The Dissertation Committee for Xi Zhang Certifies that this is the approved version of the following dissertation:

Laser Wakefield and Direct Acceleration in the Plasma Bubble Regime

Committee:

Swadesh Mahajan, Supervisor

Gennady Shvets, Co-Supervisor

Michael Downer

Philip Morrison

Milos Milosavljevic

Laser Wakefield and Direct Acceleration in the Plasma Bubble Regime

by

Xi Zhang

Dissertation

Presented to the Faculty of the Graduate School of

The University of Texas at Austin

in Partial Fulfillment

of the Requirements

for the Degree of

Doctor of Philosophy

The University of Texas at Austin

August 2017

Dedication

To my parents Youling Zhang and Lizhen Lin

To my wife Wenmin Zhang

Acknowledgements

First of all, I would like to thank Prof. Gennady Shvets. This dissertation could not be completed without his guidance, support and patience. His creativity, knowledge and hardworking influenced me a lot during all these years. The research under his guidance could be expressed as a poem from the southern song dynasty: "*After endless mountains and rivers that leave doubt whether there is a path out, suddenly one encounters the shade of a willow, bright flowers and a lovely village*."

I would like to express my grateful thanks to Prof. Swadesh Mahajan for being my supervisor and helping me through the graduation process.

I would like to thank Dr. Vladimir Khudik. His research style and enthusiasm in science impact me through the close interactions in these years. This dissertation would be finished much harder without his daily help and guidance. His suggestions as an experienced scientist are valuable to me.

I would thank Prof. Mike Downer and his experimental research group. My first and the most impressive class at UT-Austin was given by Prof. Downer. I learned a lot from the collaborations with them. I would thank Prof. Philip Morrison and Prof. Milos Milosavljevic for kindly serving on my dissertation committee. I would thank all my friends and colleges at UT-Austin. The Ph.D. life would not be happy without them.

Finally, my parents Youling Zhang and Lizhen Lin are always my solid support in all my life stages. I love them and wish them health and happiness. My wife Wenmin Zhang's patience and encouragement stimulate me to move forward. She is the most beautiful gift that life granted to me.

Laser Wakefield and Direct Acceleration in the Plasma Bubble Regime

Xi Zhang, Ph.D.

The University of Texas at Austin, 2017

Supervisor: Swadesh Mahajan

Co-Supervisor: Gennady Shvets

Laser wakefield acceleration (LWFA) and direct laser acceleration (DLA) are two different kinds of laser plasma electron acceleration mechanisms. LWFA relies on the laser-driven plasma wave to accelerate electrons. The interaction of ultra-short ultra-intensive laser pulses with underdense plasma leads the LWFA into a highly nonlinear regime ("plasma bubble regime") that attracts particular interest nowadays. DLA accelerates electrons by laser electromagnetic wave in the ion channel or the plasma bubble through the Betatron resonance. This dissertation presents a hybrid laser plasma electron acceleration mechanism. We investigate its features through particle-in-cell (PIC) simulations and the single particle model. The hybrid laser plasma electron acceleration is the merging concept between the LWFA and the DLA, so called laser wakefield and direct acceleration (LWDA). The requirements of the initial conditions of the electron to undergo the LWDA are determined. The electron must have a large initial transverse energy $\epsilon_\perp$. Two electron injection mechanisms that are suitable for the LWDA, density bump injection and ionization induced injection, are studied in detail. The features of electron beam phase space and electron dynamics are explored. Electron beam phase space appears several unique features such as spatially separated two groups, the correlation between the transverse energy $\epsilon_\perp$ and the relativistic factor γ and the

double-peak spectrum. Electrons are synergistically accelerated by the wakefield as well as by the laser electromagnetic field in the laser-driven plasma bubble. LWDA are also investigated in the moderate power regime (10 TW) in regarding the effects of laser color and polarization. It is found that the frequency upshift laser pulse has better performance on avoiding time-jitter of electron energy spectra, electron final energy and electron charge yield. Some basic characters that related to the LWDA such as the effects of the subluminal laser wave, the effects of the longitudinal accelerating field, the electron beam emittance, the electron charge yield and potentially applications as radiation source are discussed.

Table of Contents

List of Figures

Chapter 1

Introduction

1.1 Plasma-Based Electron Acceleration

Particle accelerator plays a very important role in our human history. It not only helps us to understand the origin of matters and the universe but also provides us the broad applications such as radiation source, isotope production, ion implantation, electron beam material processing, medical therapy and so on [1]. Conventional RF accelerators have typical accelerating gradient up to ~ 100 MV/m due to the limit of the dielectric medium. They require long acceleration distance to obtain high energy. A seminal paper in 1979 by Tajima and Dawson [2] attracted people's attention to use the plasma as the accelerating medium. Plasma has the nature of supporting ultra-high accelerating gradient (e.g. 10^{18} cm^{-3} plasma density has ~ 100 GV/m accelerating gradient) and is an excellent resource of electrons. These advantages make plasma-based acceleration as one of the most promising next generation acceleration mechanisms. With the rapid advancing of laser technology and decades of exciting scientific researches, huge progresses have been made [3]. Scientists experimentally demonstrated that plasma-based electron accelerators are able to produce mono-energetic electron beams [4, 5, 6]. After a few years, GeV level mono-energetic electron beams are achieved within centimeters-scales [7, 8, 9, 10]. The applications of plasma-based electron accelerators are constantly broadening from the table-top high energy electron source to the X-ray or even Gamma-ray source [11, 12].

Plasma-based electron acceleration generally can be divided into two groups: one group relies on the driven plasma wave to accelerate electrons. The driver can be ultra-intensive laser pulse [13], high energy electron beam [14, 15] and high energy

proton beam [16]. Laser wakefield acceleration utilizes laser pondermotive force to generate the plasma waves as the dynamic accelerating structures while the electron beam or proton beam driven plasma wake field acceleration relies on the electromagnetic field of the charged particle beams to create the similar accelerating structures.

The lawson-woodard-palmer theorem [17] states that an ultra-relativistic particle cannot gain a net energy or momentum from a laser in free space. Therefore, the other group of plasma-based acceleration utilizes plasma as a wiggler or undulator to make the energy transfer from laser to electrons possible. The laser pulse directly imparts its electromagnetic energy into electrons. Direct laser acceleration [18, 19] is one of the most important representatives in this group. It accelerates electrons in the ion channels [18, 19, 20] or in the plasma bubbles through the Betatron resonance mechanism.

1.1.1 Laser Wakefield Acceleration

The laser pulse propagating in the under-dense plasma which has the plasma density $n<n_c$ (n_c is the plasma critical density) excites the plasma wave so called wakefield. The driving mechanism of the wakefield is the ponderomotive force of the laser pulse. The ponderomotive force of the laser pulse is the second-order electromagnetic force. We consider the relativistic equation of motion of an electron in the collisionless plasma under the influence of electromagnetic field

$$\frac{d\vec{p}}{dt} = -e\left(\vec{E} + \frac{\vec{v}}{c}\times\vec{B}\right), \tag{1.1}$$

The electric field $\vec{E}$ and magnetic field $\vec{B}$ can be expressed by the vector potential $\vec{A}$ as $\vec{E} = -\frac{1}{c}\frac{\partial\vec{A}}{\partial t}$ and $\vec{B} = \nabla\times\vec{A}$. Therefore, the equation (1.1) can be written as follow

$$\frac{d\vec{p}}{dt} = -e\left(-\frac{1}{c}\frac{\partial\vec{A}}{\partial t} + \frac{\vec{v}}{c}\times\nabla\times\vec{A}\right), \tag{1.2}$$

The motion of an electron in the high-frequency electromagnetic field can be split into the fast oscillation component and the slow oscillation component, that is $\vec{p} = \overrightarrow{p_f} + \overrightarrow{p_s}$. To the lowest order, the fast oscillation component of the electron can be approximated as

$$\overrightarrow{p_f} = \frac{e\vec{A}}{c}, \tag{1.3}$$

After splitting the electron momentum with respect to different time scales and applying Eq. (1.3), we reach the equation of motion to the second order

$$\frac{d\overrightarrow{p_s}}{dt} = -\frac{\vec{p}}{\gamma m}\cdot\nabla\overrightarrow{p_f} - \frac{\vec{p}}{\gamma m}\times\nabla\times\overrightarrow{p_f}, \tag{1.4}$$

The above Eq. (1.4) can be further simplified. Averaging over a laser cycle, we end up with the approximated expression of the ponderomotive force

$$\overrightarrow{F_p} = \frac{d\overrightarrow{p_s}}{dt} = -\mathrm{mc}^2\nabla\bar{\gamma}, \tag{1.5}$$

where $\gamma = (1 + \frac{p_s^2}{m^2c^2} + \frac{e^2|\vec{A}|^2}{m^2c^4})^{1/2}$.

The ponderomotive force of the laser pulse generates the periodic plasma wave called laser wakefield that can be used as the dynamic accelerating structure. The structures of laser wakefield strongly depend on the laser pulse. They can range from the linear laser wakefield regime to the highly nonlinear wakefield regime so called plasma bubble regime. We will briefly derive the linear laser wakefield and this will conceptually explain the driving mechanism of laser wakefield acceleration. The starting point is the Maxwell equations coupled with the equation of motion in the collisionless cold plasma [21]

$$\frac{d\vec{p}}{dt} = -e\left(\vec{E} + \frac{\vec{v}}{c}\times\vec{B}\right), \tag{1.6}$$

$$\nabla \cdot \vec{E} = 4\pi e(n_0 - n_e), \tag{1.7}$$

$$\nabla \times \vec{E} = -\frac{1}{c}\frac{\partial \vec{B}}{\partial t}, \tag{1.8}$$

$$\nabla \cdot \vec{B} = 0, \tag{1.9}$$

$$\nabla \times \vec{B} = -\frac{4\pi}{c} e n_e \vec{v} + \frac{1}{c}\frac{\partial \vec{E}}{\partial t}, \tag{1.10}$$

We assume the laser propagating in the x-direction and change the variable $\tau = t - x/v_p$, where v_p is the plasma wave phase velocity. After some algebra, we end up with the following equations

$$n_e = \frac{\beta_p n_0}{\beta_p - u_x}, \tag{1.11}$$

$$\frac{d}{d\tau}\left[\left(u_x - \beta_p\right)\frac{dp_x}{d\tau} + u_y\frac{dp_y}{d\tau} + u_z\frac{dp_z}{d\tau}\right] = \frac{\omega_p^2 \beta_p^2 u_x}{\beta_p - u_x}, \tag{1.12}$$

where $\beta_p = v_p/c$, $\vec{u} = \vec{v}/c$, the plasma frequency $\omega_p^2 = 4\pi e^2 n_0/m_e$ and $\vec{p}$ is normalized to $m_e c$. For the small pump strength and laser is polarized in the y-direction, it is reasonable to assume that $p_x \cong u_x \ll 1, p_y \cong u_y \ll 1$, $u_z = 0$. The Eq. (1.11) and Eq. (1.12) can be further simplified to

$$n \equiv n_e - n_0 = \frac{u_x n_0}{\beta_p}, \tag{1.13}$$

$$\frac{\partial^2 n}{\partial t^2} + \omega_p^2 n = \frac{n_0}{2}\frac{\partial^2}{\partial x^2}a^2, \tag{1.14}$$

To derive the Eq. (1.14), we have use the transformation $\frac{\partial}{\partial t} = \frac{\partial}{\partial \tau}$, $\frac{\partial}{\partial x} = -\frac{1}{c\beta_p}\frac{\partial}{\partial \tau}$ and the relation $a = v_y/c$. The Eq. (1.14) describes the linear wakefield generation by the laser ponderomotive force. It is useful to point out a more common form of Eq. (1.14) under the quasi-static approximation $\frac{\partial}{\partial x} = \frac{\partial}{\partial \xi}$, $\frac{\partial}{\partial t} = \frac{\partial}{\partial \tau} - c\frac{\partial}{\partial \xi} \cong -c\frac{\partial}{\partial \xi}$ where $\xi = x - ct$. The laser pulse is assumed to be slowly varying during the electron transit time under the quasi-static approximation. The Eq. (1.14) can be written as

$$\frac{\partial^2 n}{\partial \xi^2} + k_p^2 n = \frac{n_0}{2}\frac{\partial^2}{\partial \xi^2}a^2, \tag{1.15}$$

It is clear that the laser wakefield is basically the driven plasma electron density perturbation. The plasma electron density perturbation leads to the local breakdown of the quasi-neutrality of the plasma and thus induces the electric field that can be used to accelerate electrons. The electric fields that the laser wakefield supports are on the order of $E_{\parallel} = m_e c\omega_p/e$. We have a useful estimation of the accelerating field in the laser wakefield accelerator

$$E_{\parallel}(V/m) \sim \sqrt{n_0(cm^{-3})}, \tag{1.16}$$

We discuss the linear laser wakefield so far. The development of modern laser technology (e.g. CPA [22]) has brought us the high-power (e.g. 1 PW) high-intensity (e.g. 10^{18}W/cm^2) short pulse laser (e.g. femtosecond). The high-power laser pulse interacts with the under-dense plasma push the laser wakefield to the nonlinear regime.

Before moving into the nonlinear regime of laser wakefield, it is worth mentioning the self-focusing of the laser pulse propagating in the under-dense plasma. The self-focusing is from the non-uniformity of the plasma refractive index $\eta(r)$ induced by the laser pulse. The refractive index $\eta(r) \sim 1/a(r)$ and the laser pulse intensity peaks on the axis $(r = 0)$. Therefore, this kind of shape of the refractive index focuses the laser pulse. In general, the critical power of the under-dense plasma is used to identify the self-focusing of the laser pulse [21]

$$P_c \cong 17.5\left(\frac{\omega}{\omega_p}\right)^2. \tag{1.17}$$

It is required that the power of the laser pulse $P > P_c$ to trigger the self-focusing. The self-focusing usually happens in a laser propagation distance

$$z_c = \frac{z_R}{(\frac{P}{P_c} - 1)^{1/2}}, \tag{1.18}$$

where $z_R = \frac{\pi w_0^2}{\lambda}$ is the Rayleigh Length. The self-focusing distance is on the scale of the laser pulse Rayleigh Length and decreases with the increase of the laser power. The self-focusing of intense electromagnetic wave was first demonstrated in simulations [23, 24].

A high-power short pulse laser pulse propagating in the under-dense plasma is able to create an ion cavity that is empty of electrons. The ions can be treated as immobile since they have much larger inertia than electrons. This regime of the laser wakefield acceleration is called the "bubble regime" or the fully blow-out regime [13]. The plasma bubble regime is the most interesting regime in the laser wakefield acceleration. Fig. 1.1(a) is the plasma bubble structure from the Particle-In-Cell simulation. The high-power laser pulse blows out the electrons behind it and creates a quasi-spherical ion cavity. The plasma bubble has the longitudinal fields and transverse fields. Fig. 1.1(b) is the sketch of the plasma bubble fields. The electrons are accelerated by the plasma bubble longitudinal accelerating field but also focused by the plasma bubble transverse focusing fields. These two features open the possibility to generate the high quality electron beams. All the fields in the plasma bubble are symmetric with respect to the center of the plasma bubble.

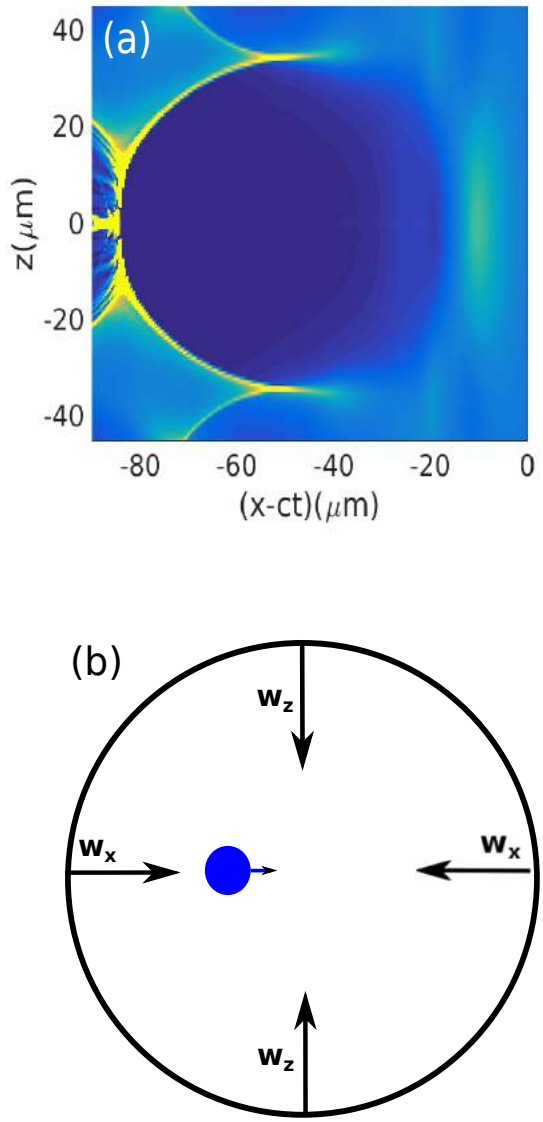

FIGURE 1.1: (a) The plasma bubble density structure driven by the Texas Peta-watt Laser in the plasma density 5×10^{17}cm^{-3}. (b) The schematic demonstration of the fields in the plasma bubble.

Electrons are decelerated after passing the center of the plasma bubble. This is an important concept called dephasing. The dephasing sets the limit of the electron energy gain from the laser wakefield. The acceleration distance cannot exceed the dephasing length L_d after which the trapped electrons are decelerated and lose energy. Besides the dephasing length L_d, the laser energy is depleted by both the diffraction and interaction with the plasma. The electron acceleration can only happen before the pump depletion happens. The laser pulse propagation distance before the pump depletion is called the pump depletion length L_{pd}. The estimation of the dephasing length L_d and the pump depletion length L_{pd} in the 3D nonlinear regime have the expression [25, 26]

$$L_d = \frac{4}{3}\frac{\omega_0^2}{\omega_p^2}\frac{\sqrt{a_0}}{k_p}, \tag{1.19}$$

$$L_{pd} = \frac{\omega_0^2}{\omega_p^2}c\tau, \tag{1.20}$$

Eqs. (1.16), (1.19) and (1.20) are commonly used to estimate the maximum electron energy gain in the plasma bubble regime of a laser wakefield accelerator.

1.1.2 Direct Laser Acceleration

It is surprising that a completely different acceleration mechanism so called direct laser acceleration exists in the same laser plasma interaction system as laser wakefield acceleration. Direct laser acceleration was first demonstrated in the ion channel via Particle-In-Cell simulations [18] and then observed in the experiment [19]. Due to the poor electron beam quality and the broad energy spectrum (Boltzmann like), direct laser acceleration did not attract much attention for a few years. Recently, people renewed interest in the direct laser acceleration because of the possible combination between the direct laser acceleration and the laser wakefield acceleration [27, 28] and the radiation generation [29, 30].

It uses the ion channel or the plasma bubble as a wiggler and the laser electromagnetic field directly accelerates electrons through the Betatron resonance mechanism [31, 32]. Betatron resonance is between two frequencies, the Betatron frequency ω_β that describes the relativistic electron wiggling motion in the plasma and the Doppler shifted laser frequency ω_d that describes the laser frequency observed by the relativistic electrons.

$$\omega_\beta = \frac{\omega_p}{\sqrt{2\gamma}}, \tag{1.21}$$

$$\omega_d = (1 - \frac{v_\parallel}{v_p})\omega_0, \tag{1.22}$$

where ω_p is the plasma frequency as mentioned above and ω_0 is the laser frequency. When the Betatron frequency matches the averaged Dopper shifted laser frequency $\omega_\beta = l < \omega_d >$, the Betatron resonance happens and the laser directly accelerates electrons by its electromagnetic field. The Betatron resonance does not need to be in the first order to have the net acceleration. It means that it is possible to have $l = 1,3,5\cdots$. When $l \neq 1$, it is called high-order direct laser acceleration [20, 33]. The electron energy gain from the laser has the expression $A_L \sim -e\int \vec{v}_\perp \cdot \vec{E}_L dt$. From the micro-point of view, the laser electric field $\vec{E}_L$ accelerates the electrons in the transverse direction and the laser magnetic field $\vec{B}_L$ re-distributes the electron energy to the longitudinal direction through the Lorentz force.

There is no analytical theory for the direct laser acceleration in the plasma bubble regime. [18, 20] developed the comprehensive analytical theory for the direct laser acceleration in the ion channel. We will only briefly introduce several important properties of the direct laser acceleration in the ion channel. The starting point is the Eq. (1.6) under the assumption that the laser fields are linear polarized plane wave $E_y^{(L)} = E_0 cos\phi$, $B_z^{(L)} = E_y^{(L)} c/v_{ph}$ and $\phi = \omega_L(x/v_{ph}$ -t). The first important

property is the transverse oscillation of the electrons. We use the transverse energy $\epsilon_\perp$ to describe the transverse oscillations of the electrons.

$$\epsilon_\perp = \frac{p_y^2}{2p_x} + \frac{\omega_p^2 m_e y^2}{4}, \tag{1.23}$$

The direct laser accelerated electrons always have big transverse oscillation since the laser field imparts the energy to electrons transversely. The transverse energy is derived from the expansion of the electron's ultra-relativistic factor [20]. There is an integral of motion from Eq. (1.16).

$$\gamma - \frac{v_{ph}}{c}\frac{p_x}{m_e c} + \frac{\omega_p^2 y^2}{4c^2} = I_0 = const, \tag{1.24}$$

This integral of motion is important since it gives us the relation among the variables of the electron motion. Eq. (1.24) can be further simplified using the transverse energy $\epsilon_\perp$ and the longitudinal momentum p_x.

$$(1 - \frac{v_{ph}}{c})\frac{p_x}{m_e c} + \frac{\epsilon_\perp}{m_e c^2} = I_0 = const, \tag{1.25}$$

Eq. (1.25) indicates that for the luminal direct laser acceleration ($v_{ph} = c$), the transverse energy $\epsilon_\perp$ is constant during the whole process. The electrons will not change their oscillation amplitude. For the super-luminal direct laser acceleration ($v_{ph} > c$) which is very common in the under-dense plasma [21], the electrons' oscillation amplitude will not be a constant. We have to point out that these discussions are under the assumption that there is no longitudinal accelerating field. The integral of motion does not exist in the plasma bubble regime that has the spatial changing longitudinal accelerating field.

Instead of going through all the formulas of the electron dynamics of the DLA in the ion channel [20], we show two representative plots to demonstrate the electron dynamics of the DLA in the ion channel.

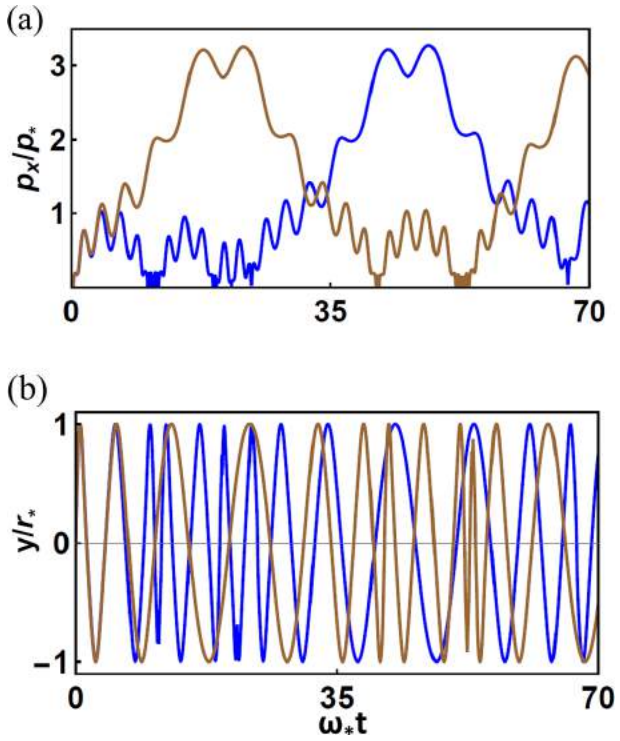

FIGURE 1.2: Two electrons are initially placed at rest on the channel axis and interact with the luminal laser wave ($v_{ph} = c$). Parameters for blue curve: $\omega_p/\omega_0 = 0.05$ and $a_0 = 4$ ($p_* = 200$ and $\omega_* = \omega_L/400$), for brown curve: : $\omega_p/\omega_0 = 0.02$ and $a_0 = 10$ ($p_* = 1250$ and $\omega_* = \omega_L/2500$). (a) The electron longitudinal momentum p_x. (b) The electron transverse oscillation y.

Fig. 1.2(a) shows that the DLA efficiently accelerates electron to high energy ($p_x > 600 m_e c$). However, the electron cannot keep the energy and it has the similar dephasing concept with the LWFA. The electron will transform from the accelerating phase to the decelerating phase after reaching the peak of the energy and this process will continue during the whole process. As the prediction of Eq. (1.25), the electron oscillation amplitude does not change as shown in Fig.1.2 (b). This dissertation will provide a method to avoid the dephasing of the DLA.

1.2 Particle-In-Cell Simulation

Experiments could be too expensive and time-consuming in some situations. Some highly nonlinear phenomenon in laser plasma interaction are too complicated to give the rigorous theoretical description. Simulation becomes an important alternative for the research of the laser plasma interaction. There are two kinds of the most commonly used simulation methods in the plasma physics: MagnetoHydroDynamic (MHD) simulation [34] and Particle-In-Cell (PIC) simulation [35]. MHD simulation treats the plasma as the fluid elements and numerically solves the sets of fluid equations coupled with Maxwell's equations. It describes the macroscopic phenomenon in general. PIC simulation captures the plasma particle motions and the evolution of the electromagnetic fields. It is the most computational demanding.

PIC simulation is the combination of the particle pusher and the field solver. The particle pusher pushes the macro-particles that represent many real particles based on newton's equation. The common method is so-called Boris pusher [36]. Boris pusher separates the effects of the electric field $\vec{E}$ and the magnetic field $\vec{B}$. The electric field $\vec{E}$ increases the magnitude of the particle momentum $\vec{p}$ and the magnetic field $\vec{B}$ changes the direction of the particle momentum $\vec{p}$. The field solver solves the Maxwell's equations on the spatial and temporal discretized grids and the common method is Finite-Difference-Time-Domain (FDTD) [36]. The electric field electric field $\vec{E}$, the magnetic field $\vec{B}$ and the current $\vec{J}$ are defined in the Yee Lattice [37]. The updates of the electric field $\vec{E}$ and the magnetic field $\vec{B}$ are staggered on the time domain. People use various schemes to push fields such Yee scheme [37] and

Numerical Dispersion Free scheme (NDF) [38]. Fig. 1.3 (a) shows the Yee Lattice and Fig. 1.3 (b) is the brief illustration of PIC algorithm.

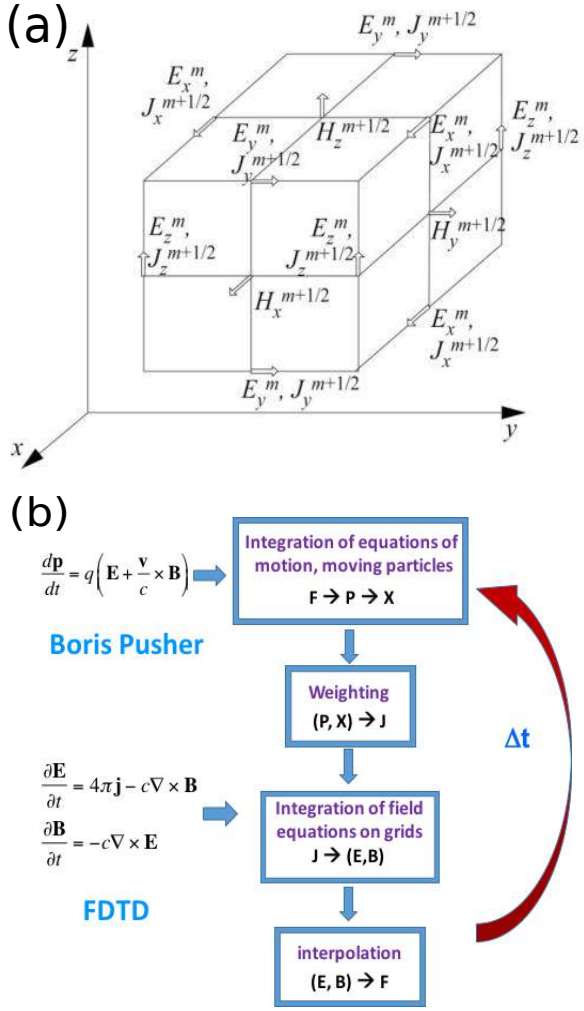

FIGURE 1.3: (a) The sketch of the Yee Lattice (courtesy to [39]). (b) The loop of the PIC algorithm.

Besides the above mentioned main PIC algorithm, the charge conservation is the other important issue in PIC simulation. There are two commonly used methods to

face this issue. The first one corrects the electric field by solving Possion's Equation after each time updates. This method is time-consuming and has difficult to parallelize [36]. The second one is the rigorous charge conservation method proposed by [40]. It automatically keeps the charge conservation when the moving charges generate the currents. The rigorous charge conservation scheme is more efficient and easy to parallelize. Nowadays, the most of PIC codes implement the rigorous charge conservation scheme.

1.3 Recent Experiments on Laser Plasma Electron Acceleration

Theoretical, computational and experimental researches in the laser plasma electron acceleration have had very close collaborations for decades. The electron acceleration during the laser plasma interaction was observed [41] a few years after the first paper about this concept [2]. Serials of papers was published in 2004 that demonstrated the mono-energetic laser plasma electron acceleration to more than 100 MeV [4, 5, 6]. The operations in these experiments were already in the plasma bubble regime. A couple of years later, 1 GeV mono-energetic electron beam was produced via the external channel guiding laser wakefield acceleration [7].

The energy level stayed on 1 GeV for a few years. During these years, peta-watt lasers became available in the world. Texas Peta-Watt (TPW) laser which has the peak power (1.1 PW [42]) is one of the most important facilities for the laser wakefield acceleration in the world. In 2013, 2 GeV quasi-mono-energetic electron beam was produced from TPW laser wakefield acceleration [8]. It was the self-guided self-injection [43, 44, 45] laser wakefield acceleration in a 7 cm pure helium gas cell. The plasma density is below $10^{18}cm^{-3}$. In the low density plasma, the dephasing length

L_d and the pump depletion length L_{pd} are expected to be long based on Eq. (1.19) and Eq. (1.20), which is good for the electron acceleration. Fig.1.4 (a) shows the experimental measured electron energy spectrum. There is a mono-energetic peak at about 2 GeV.

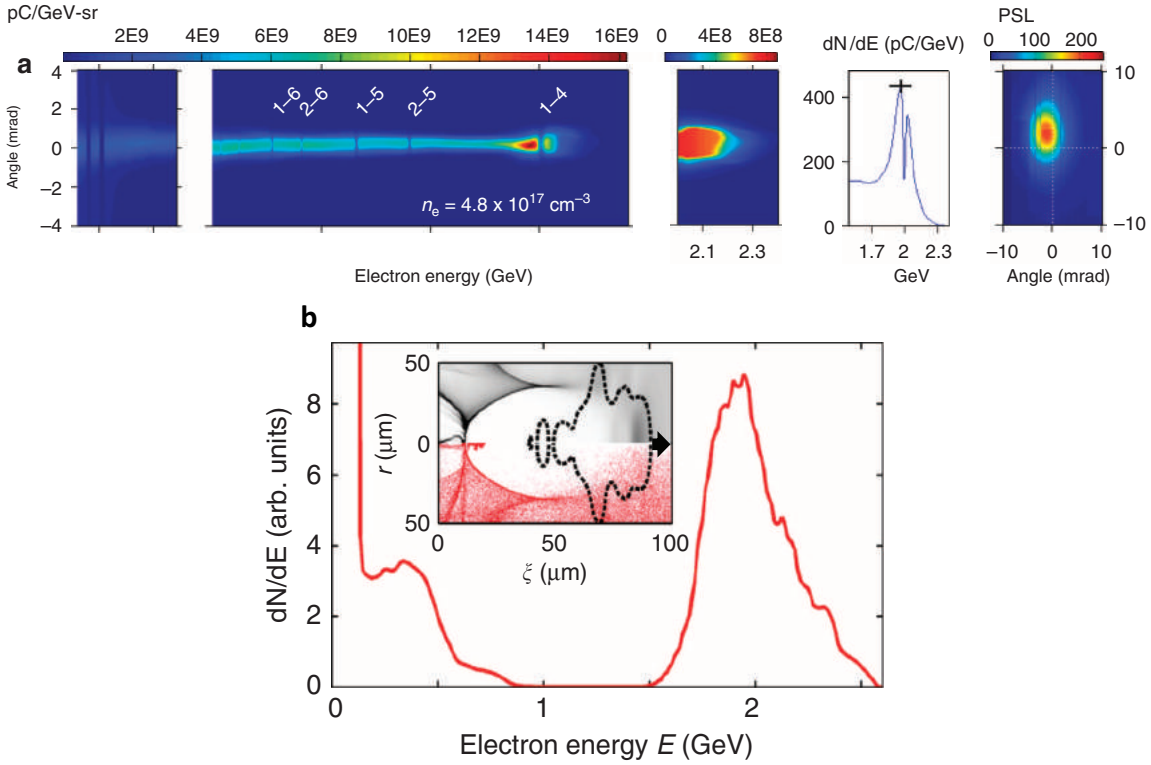

FIGURE 1.4: (a) The experimental results for the 2 GeV quasi-mono-energetic electron acceleration from TPW laser wakefield acceleration. (b) The PIC simulation (WAKE) of the experiment shown in (a), simulation parameters: plasma density n=5×10^{17}cm^{-3}, laser energy 100 J, duration $\tau = 160\, fs$, third-order super-Gaussian transverse shape with radius $w_0 = 275\, \mu m$. (courtesy to [8])

The PIC simulation well explained the 2 GeV experimental results as shown in Fig.1.4 (b). The key issue in the PIC simulation is that the TPW laser pulse had the

very wide transverse energy spread. It took very long propagation distance (~ 5 cm) for the laser pulse to self-focus and form the plasma bubble. The electron self-injection and the acceleration happened in the last 2 cm in the gas cell. Except the above single stage 2 GeV result, the other 3 GeV result by the dual-stage laser wakefield accelerator was demonstrated in 2013 [9].

The most recent world record in the laser wakefield acceleration is the 4.2 GeV mono-energetic electron beam which was produced in 2014 [10]. It was the channel guiding peta-watt laser driven laser wakefield acceleration. The experimental energy record is still pushing forward. The multi-stage laser wakefield acceleration is ongoing [46].

People never stop trying to understand the laser wakefield acceleration process. The diagnostic techniques for the laser wakefield acceleration are the other important experimental research area. The first laboratory real snapshot of the laser wakefield was done in 2006 [47]. In 2014, the same group published the first laboratory visualization of the evolution of the laser wakefield acceleration in the plasma bubble regime by the all-optical streak camera technique [48]. It was the

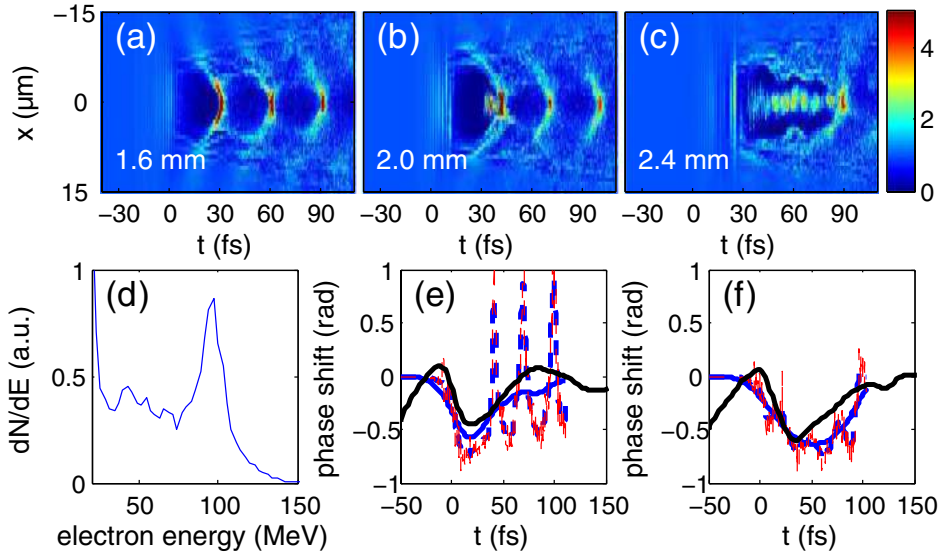

FIGURE 1.5: (a)-(c) The plasma bubble evolution from the 3D PIC simulation (VLPL). (d) The electron energy spectrum from the simulation. (e)-(f) The plasma bubble phase shift perturbation $z = 2.0\,mm$ (e) and $z = 2.6\,mm$ (f) for the ideal unlimited band-width probe (red), 100 nm probe (blue dashed) and 10 nm probe (blue solid). The black lines are measured from experiment for n=2×10^{19}cm^{-3}. Simulation parameters: plasma density n=1.5×10^{19}cm^{-3}, UT^3 laser system: 800 nm, laser pulse energy 0.8 J, duration $\tau = 30\,fs$, spot size $w_0 = 10\,\mu m$. (courtesy to [48]).

1D visualization of the plasma bubble evolution. The 2D visualization was done one year later [49]. It not only captured the plasma bubble evolution but also the self-injection process during the bubble elongation.

The electron motion in the laser wakefield acceleration has the multi-dimensional property. From the well-known synchrotron radiation formula [50], it is natural to explore the possibility of be an excellent radiation source. The experiments of the

radiation generation are always the important part of the laser plasma electron acceleration. The Betatron radiation experiments in the laser wakefield acceleration produced KeV X-rays more than a decade ago [51, 52]. The resonant betatron oscillation in the plasma bubble regime has extended the radiation to the Gamma-ray regime (more than 100 KeV) [12]. This experiment also imaged the amplified electron oscillation and might be the direct evidence of the DLA in the plasma bubble regime. Other methods were also employed to generate the high energy radiation. By adding a plasma mirror, the all-optical Gamma-ray source were created [53, 54]. The thin solid target was placed after the under-dense plasma. The laser pulse was reflected by the solid target and interacted with the laser wakefield accelerated electron beam. The high energy radiation was emitted through the Compton scattering process. This method produced very broad-band radiation spectrum that extended to the Gamma-ray regime. People also used two laser pulses instead of the thin solid target. The laser wakefield accelerated electrons collided with the scattering laser beam. The quasi-mono-energetic tunable X-ray was observed by colliding the tens of MeV electron beam with the scattering laser beam [55]. The multi-MeV Gamma-ray was reached by colliding the hundreds of MeV electron beam with the scattering laser beam [56]. More experiments are ongoing based on even larger laser system and even higher electron beam energy. It is promising to get higher energy radiation.

1.4 Summary

In summary, the plasma-based electron acceleration has huge advantages compared with the conventional accelerators and has very promising future applications. LWFA and DLA are two different major plasma-based electron

acceleration mechanisms. They have been studied for decades but are still the shining stars. Computational research plays a very important role in the area of the plasma-based electron acceleration and PIC is the main tool for the simulations. Experimental research is always the most important part. Many experiments have demonstrated the promising applications such as table-top high energy electron source and X-ray or Gamma-ray source. There are ongoing experiments to explore more exciting applications, approach the real daily applications and feed our human thirst for new physics.

This dissertation explores the hybrid LWFA and DLA (laser wakefield and direction acceleration LWDA) electron acceleration mechanism in the under-dense plasma. The chapters are organized as follow: Chapter 2 introduces the main injection mechanisms in the LWFA and the two suitable injection mechanisms we investigate for the LWDA. Chapter 3 studies the characters for the LWDA. We analyze the effects of the DLA laser pulse phase velocity and the plasma bubble accelerating field on the LWDA. The requirements of the electrons' initial conditions are determined. The dynamics of LWDA electrons are investigated in this chapter. Chapter 4 goes to the LWDA in the moderate laser power regime. Interesting effects regarding the laser polarizations and laser colors are discovered. Based on the discovery, we propose the more reliable and well-performed LWDA in the moderate laser power regime. Chapter 5 summarizes the whole dissertation and discusses the future possible research directions in this field.

Chapter 2

Electron Injection and Acceleration in Laser Wakefield and Direct Acceleration[1,2]

2.1 Electron Injection in Laser Wakefield Acceleration

One of the most important issues in the LWFA concerns the electron injection. Laser wakefield is an excellent electron accelerating structure. However, the electrons must be injected into the wakefield to get acceleration. In general, electron injection mechanism in all plasma based electron accelerators can be divided into two classes: density-based injection mechanism and laser-based injection mechanism. We focus on the electron injection in the plasma bubble regime of LWFA, in which most of the researches are done in this regime nowadays [3].

The electron motion in the plasma bubble regime of LWFA can be described by using the Moving Frame Hamiltonian (MFH) [26, 43, 44, 45]

$$H = \gamma m_e c^2 - v_b p_x - e\Psi, \tag{2.1}$$

where $\gamma = \sqrt{1 + (\vec{P} + \frac{e}{c}\vec{A})^2}$ and $\vec{P}$ is the canonical momentum, $\Psi = \frac{v_b}{c}A_x - \Phi$ is the wake potential constructed from its vector potential A_x and its scalar potential Φ. v_b is the plasma bubble group velocity and has the approximate expression $v_b = \sqrt{1 - (\frac{\omega_p}{\omega_L})^2}$. The MFH is derived from the electron averaged Hamiltonian in the slowly varying plasma bubble electromagnetic field [26]. The MFH is the integral of motion which does not explicitly depend on time. When the electrons are trapped in the plasma bubble, they must satisfy the condition $v_x \geq v_b$ that is the electrons'

[1] X. Zhang, V. N. Khudik, G. Shvets, Physical Review Letters 114 (18), 184801, 2015. Contribution: studied the DLA in the plasma bubble regime; carried out the single particle simulations, PIC simulations and analyzed the results; wrote the paper draft.

[2] X. Zhang, V. N. Khudik, A. Pukhov, G. Shvets, Plasma Physics and Controlled Fusion 58 (3), 034011, 2016. Contribution: studied the DLA in the plasma bubble regime based on ionization injection; carried out the single particle simulations, PIC simulations and analyzed the results; wrote the paper draft.

longitudinal velocity is larger than the plasma bubble group velocity. This condition is also equivalent to the condition $\Psi_i - \Psi_f \approx \frac{m_e c^2}{e}$. The initial and final (after trapping) wake potential have the difference about one unit. Initially, the electron kinetic momentum can be considered as zero. After trapping, the electrons are ultra-relativistic $\gamma m_e c^2 \approx v_b p_x$. There are many different methods for satisfying this trapping condition and we introduce the density-based electron injection and the laser-based electron injection briefly.

2.1.1 Density-Based Electron Injection

Density-based approaches involve shaping the longitudinal plasma density profile as a single or multiple density ramps. The plasma density variation leads to the variation of the wakefield group velocity v_b and the structure of the wakefield. These sudden changes of the wakefield make the electron injection possible in the density changing plasma.

Density-based electron injection was first proposed as a method to inject electron in the electron beam driven plasma wakefield acceleration [58]. A short electron pulse travel through a sharp, localized and downward density transition. The background plasma electrons can be trapped in in the plasma wake due to the rapid change of the plasma wavelength. It can also be understood as the rapid change of the wake group velocity v_b. The wake group velocity in the density changing plasma has the relation $\frac{v_b}{c} \approx 1 - (\frac{\xi}{2n})\frac{dn}{dx}$ where $\xi = x - ct$ [3]. After the driving beam $\xi < 0$ and during the density down-ramp $\frac{dn}{dx} < 0$, the wake group velocity v_b is decreasing. Therefore, the trapping condition $v_x \geq v_b$ is satisfied for some electrons. This theory was demonstrated by 2D PIC simulation [58]. The electron beam driven plasma wakefield acceleration usually uses the slowed down driving beam electrons

as the accelerated electrons [14, 15]. The density down ramp injection was demonstrated experimentally in the laser wakefield acceleration [59]. It generated low momentum spread electron bunches. The tunable hundreds of MeV electron beams were produced by the density down-ramp injection [60].

People considered the very short density bump injection [27] and even the density shock injection [61, 62]. The density bump injection drastically changes the plasma bubble structure and the injected electrons have complicated phase space [27]. The density shock injection utilizes the very rapid plasma density variation (a few micro-meters) to sudden change the wake group velocity v_b. The injection is localized and the electron energy spread is small [61, 62]. The method of density shock injection does not require complicated engineering. People usually uses the combination of a thin razor blade and the gas jet.

2.1.2 Laser-Based Electron Injection

Laser-based electron injection mechanisms do not require any plasma density engineering but are closely related to the laser propagation in the plasma. Due to the more complicated laser evolution dynamics in the plasma, there are more types of the laser-based electron injection mechanisms.

The first laser-based electron injection mechanism was the so called ponderomotive injection [63]. Two laser pulses that propagate perpendicular to one another are used. The pump pulse generates a standard plasma wakefield via LWFA mechanism and the injection pulse intersects the wakefield some distance behind the pump pulse. The ponderomotive force Eq. (1.5) of the injection pulse accelerates a fraction of the plasma electrons that they can be trapped in the wakefield. A colliding pulse injection mechanism was proposed after the ponderomotive injection [64].

Originally, it used a three short pulses scheme. Two pulses go forward, the pump pulse and the less intensive injection pulse. The forward injection pulse is polarized perpendicular to the pump pulse. The third injection pulse that has a similar intensity and polarization with the forward injection pulse goes backward. The two injection pulses collide at some distance after the pump pulse. The slow ponderomotive beat wave traps and heats the background plasma electrons, thus, some of the background plasma electrons are trapped in the plasma wakefield. The position of the forward injection pulse determines the electron injection location. Two pulses colliding pulse injection is also proposed [65].

Evolving plasma bubble injection is a one laser pulse induced electron self-injection mechanism. The electron injection is caused by the slow temporal expansion of the plasma bubble [43]. The bubble contraction and expansion are from the laser pulse self-focusing and de-focusing. During this process, the change of the electron Hamiltonian $\Delta H < -1$ if the plasma bubble is expanding fast enough. These kind of electrons are injected into the plasma bubble and have mono-energetic energy spectrum. The evolving plasma bubble injection has been demonstrated by a few experiments [8, 48, 49].

Ionization induced injection [66] is laser-based mechanism but it also related to the property of the plasma ions. In LWFA, the plasma is formed by the laser itself. The pre-pulse of the laser pulse ionizes the neutral gas and creates the plasma. The laser intensity $I \sim 10^{15} W/cm^2$ is enough to fully ionize the pure helium [67]. LWFA has laser intensity $I > 10^{18} W/cm^2$ and the main laser pulse is considered to interact with the fully ionized plasma. However, the plasma can also be formed via the ionization of some High-Z gas (e.g. Nitrogen and Oxygen). The High-Z gases

release the out-shell electrons when interact with the pre-pulse and the inner-shell electrons when interact with the main pulse. For Nitrogen, the significant ionizations for $N^{5+} \rightarrow N^{6+}$ (ionization potential $552\ eV$) and $N^{6+} \rightarrow N^{7+}$ (ionization potential $667\ eV$) happen when the normalized vector potential $a \geq 1.5$ for $0.8\mu m$ laser corresponding to laser intensity $I > 5{\times}10^{18} W/cm^2$. For Oxygen, the ionization potentials of the inner-shell electrons are even higher. Therefore, some of the electrons have the chance to be released in the wakefield and satisfy the trapping condition $\Psi_i - \Psi_f \approx \frac{m_e c^2}{e}$. There are a few models to describe the ionization process of the noble gas such as the barrier-suppression ionization theory (BSI) [67], Ammosov-Delone-Krainov Theory (ADK) [68], Keldysh Theory [69] and so on. The most common model in high-intensity LWFA is ADK model. The ionization rate has the expression

$$W(t) = \omega_a C \left(\frac{E_{ion}}{E_L(t)}\right)^d exp\left[-\frac{E_{ion}}{E_L(t)}\right], \tag{2.2}$$

where $\omega_a = \alpha^2 c/r_e$ is the atomic frequency unit, $\alpha = 1/137$ is the fine structure constant. C and d are the coefficient that related to the gas. E_{ion} is the ionization electric field that is also the property of the gas.

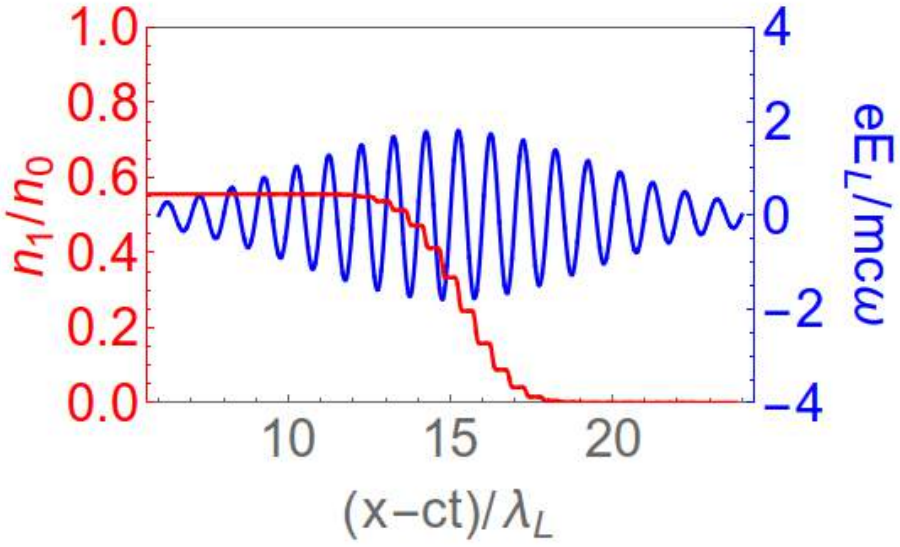

FIGURE 2.1: The fraction of ionization $N^{5+} \rightarrow N^{6+}$ in 1D configuration based on ADK tunneling ionization model. The normalized vector potential $a = 1.8$ and laser pulse duration $\tau = 25fs$.

Fig. 2.1 is the numerical demonstration of the $N^{5+} \rightarrow N^{6+}$ ionization by the high-intensity laser pulse. We solve the equation of state of Nitrogen atom by introducing the laser electric field and the ADK tunneling ionization model. The High-Z gas inner shell ionization has very fast grow when the laser intensity reaches certain level. The laser pulse propagates from left to right. It is clear that about 60% N^{5+} are ionized. Many electrons are released within the high laser intensity region where the wake potential is deep enough to get them trapped. In reality, there are also ionization events for $N^{6+} \rightarrow N^{7+}$ in this laser intensity.

Ionization induced injection has been observed in many experiments e.g. [54, 70, 71]. Ionization induced injection is stable and has small shot-to-shot variation. However, it has its own drawbacks, such as broad energy spectrum and large electron beam emittance. The reason is that ionization induced injection happens whenever the

laser intensity is high. It usually injects electrons during all the acceleration process. The laser intensity has a transverse distribution so the initial emittance could be high.

2.2 Electron Injection in Laser Wakefield and Direct Acceleration

2.2.1 Requirements of Initial Conditions

We explore the hybrid laser wakefield and direct acceleration (LWDA) in the plasma bubble regime. The first question that we need to answer is how the electrons can be injected and get efficient LWDA. The injection is associated with the electron initial conditions in LWDA. It is extremely difficult to rigorously understand the initial condition requirements of LWDA through the self-consistent PIC simulations. Thus, we introduce the single particle model. This model describes the electron dynamics under the influence of the combination of the plasma bubble fields and the laser electromagnetic fields. Due to the complexity of the real plasma bubble fields and the laser electromagnetic fields, we simplify the plasma bubble fields to the ideal case and the laser electromagnetic fields are under the assumption of the plane wave. The electron motion is assumed to be in a 2D plane and this is enough to capture most of the features of LWDA. The equations of motion are then given by

$$\frac{dp_x}{dt} = -e\left(W_x - \frac{v_z}{c}B_y^{(L)}\right), \tag{2.3}$$

$$\frac{dp_z}{dt} = -e\left(W_z + E_z^{(L)} + \frac{v_x}{c}B_y^{(L)}\right), \tag{2.4}$$

where $W_x = m\omega_p^2(x - r_b - v_b t)/2e$ is the plasma bubble accelerating field and $W_z = m\omega_p^2 z/2e$ is the plasma bubble focusing field respectively. The wakefields are the combinations of the electric and magnetic forces [26]. ω_p is the plasma frequency that is defined in the chapter 1. For simplicity, the linear polarized laser field were assumed to be planar and given by $E_z^{(L)} = -E_0 sin\omega_L(t - \frac{x}{v_{ph}})$ and $B_y^{(L)} = B_0 sin\omega_L(t - \frac{x}{v_{ph}})$ where $B_0 = cE_0/v_{ph}$. The parameters are scaled to the

laser wavelength λ_L. We need the laser and the plasma bubble parameters to start the single particle simulation. There is always synergy between the theory and the experiment in the field of the plasma-based electron acceleration. The similar parameters in experiment [12] are used in our single particle simulations and they were chosen as follows: $\frac{\omega_p}{\omega_L} = 0.032$ (corresponding to plasma density $n = 1.8\times10^{18} cm^{-3}$), $r_b = 22\lambda_L$, $\gamma_b = 18$ and $E_0 \approx 2.5\frac{m_e c\omega_L}{e}$. For these parameters the peak accelerating gradient E_{max}^W at the back of the bubble ($x = v_b t$) is $E_{max}^W \approx E_0/40 \approx 2GV/cm$. These parameters were also chosen to approximately mimic the parameters of PIC simulations presented in the next section. It is normal that the laser wave has a super-luminal phase velocity $v_{ph} > c$ propagating in the under-dense plasma ($v_{ph} = c\sqrt{1 + (\frac{\omega_p}{\omega_L})^2}$) but it is difficult to rigorously derive the laser phase velocity in the plasma bubble regime. We reasonably assume that the laser phase velocity in our single particle simulation is $v_{ph} = 1.00036c$.

The electron initial phase space color-coded by the electron energy gain from the laser wave and the representative test electrons are shown in Fig. 2.2.

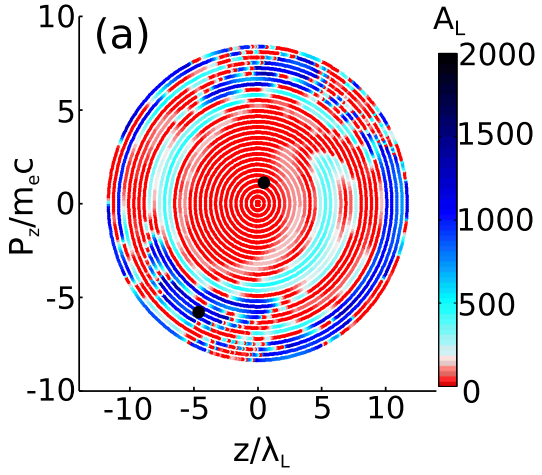

FIGURE 2.2

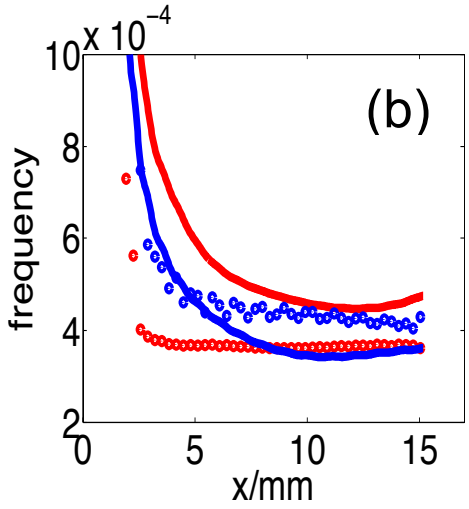

FIGURE 2.2: (a) Color-coded laser energy gain A_L as a function of the initial conditions in the (z_0, p_{z0}) phase space. Elliptical curves represent the transverse energy $\varepsilon_\perp = \frac{p_z^2}{2\gamma m_e} + \frac{\gamma m_e \omega_\beta^2 z^2}{2} = const$ curves. (b) Betatron frequency ω_β and averaged Dopper-shifted laser frequency $< \omega_d >$ ($< \omega_d >$: dotted lines, ω_β: solid lines) for two test electrons with initial conditions marked in (a) by circles. Blue lines: DLA, red lines: non-DLA test electrons.

It is apparent from Fig. 2.2(a) that, while A_L depends on the initial phase of the electron's Betatron oscillation (i.e. on the specific values of p_{z0} and z_0), a large initial value of the transverse energy is a pre-condition for DLA. The Betatron frequency ω_β and the averaged Dopper-shifted laser frequency $< \omega_d >$ of two representative DLA (blue) and non-DLA (red) electrons with initial transverse energies $\varepsilon_{\perp 0} = 0.8 m_e c^2$ and $\varepsilon_{\perp 0} = 0.1 m_e c^2$, respectively, are compared in Fig. 2.2(b). The ultra-relativistic limits of the Eqs. (1.21, 1.22) can be written as follows

$$\omega_\beta = \frac{\omega_p}{\sqrt{2\gamma}}, \tag{2.5}$$

$$\omega_d = \left(\frac{1}{2\gamma_{ph}^2} + \frac{1 + \langle p_z^2 \rangle / m_e c^2}{2\gamma^2}\right)\omega_L, \tag{2.6}$$

where $\gamma_{ph} = 1/\sqrt{v_{ph}^2 - 1}$. The two frequencies of DLA electron (blue) crosses each other. This is evidence for the Betatron resonance. It means that the LWDA

happens for the electrons with large initial transverse energy $\varepsilon_{\perp 0}$. On the contrary, the two frequencies of non-DLA electron (red) never approaches to each other and no resonance happens. In the LWDA system, the electron γ increases drastically by the wakefield acceleration. Based on Eqs. (2.5, 2.6), a large initial transverse energy $\varepsilon_{\perp 0}$ is able to compensate this initial acceleration and makes the Betatron resonance possible.

The electrons undergo significant DLA must have large initial transverse energy. Meanwhile, the laser wave always exists in the single particle model. Based on the results of the above single-particle modeling, we can now formulate the requirements of electron initial conditions for achieving synergistic LWDA in a realistic laser-plasma accelerator. First, considerable overlap between laser field and injected electrons is required for effective DLA. Second, electrons must be injected into the bubble with large transverse energy to maintain the Betatron resonance. The requirements for operating the LWDA is clear and we start the self-consistent PIC simulation to demonstrate it.

2.2.2 Density bump electron injection

We use a 2D PIC code VLPL [38] to model the self-consistent interaction of a multi-terawatt laser pulse with tenuous ($n = 1.8\times10^{18} cm^{-3}$) plasma to demonstrate that two conditions can be met. The first requirement needed is that the intensive laser wave in the accelerating part of the plasma bubble. It is a little unusual since the plasma bubble regime requires the ultra-short high power laser pulse [3, 13]. Therefore, we introduce the second time-delayed less intensive laser pulse co-propagates with the pump pulse. The second time-delayed laser pulse fills the

accelerating part of the plasma bubble but has no observable effect on the plasma bubble accelerating structure.

The second condition is met by engineering the self-injection of the background plasma electrons into the bubble. As discussed above, there are two possible ways to inject electrons in general. We explore the density-based injection in this section. The density down-ramp injection usually inject electron from the bottom of the plasma bubble with small transverse energy $\varepsilon_\perp$. A short injection density bump shown in Fig. 2.3(a) is utilized to rapidly deform the plasma bubble, thereby causing self-injection [43, 44, 45, 58, 70, 72] of plasma electrons. Note that, although the bubble is fully formed for $x < L_1 + L_2$, no self-injection occurs prior or after the laser encountering the density bump. Experimental approaches to generating such density bumps have been described elsewhere [73, 74]. Due to the drastic change of the plasma density, the plasma bubble structure is strongly deformed and the electrons that are in the sheath of the plasma bubble are shaked into the plasma bubble. The bump-facilitated injection can be thought of as a less "gentle" version of transverse injection [72] that imparts self-injected electrons with large transverse energy $\varepsilon_\perp$ needed for efficient DLA as illustrated in Fig. 2.2(a). After passing by the plasma density bump, the plasma bubble is re-formed and stably propagates more than 1 cm.

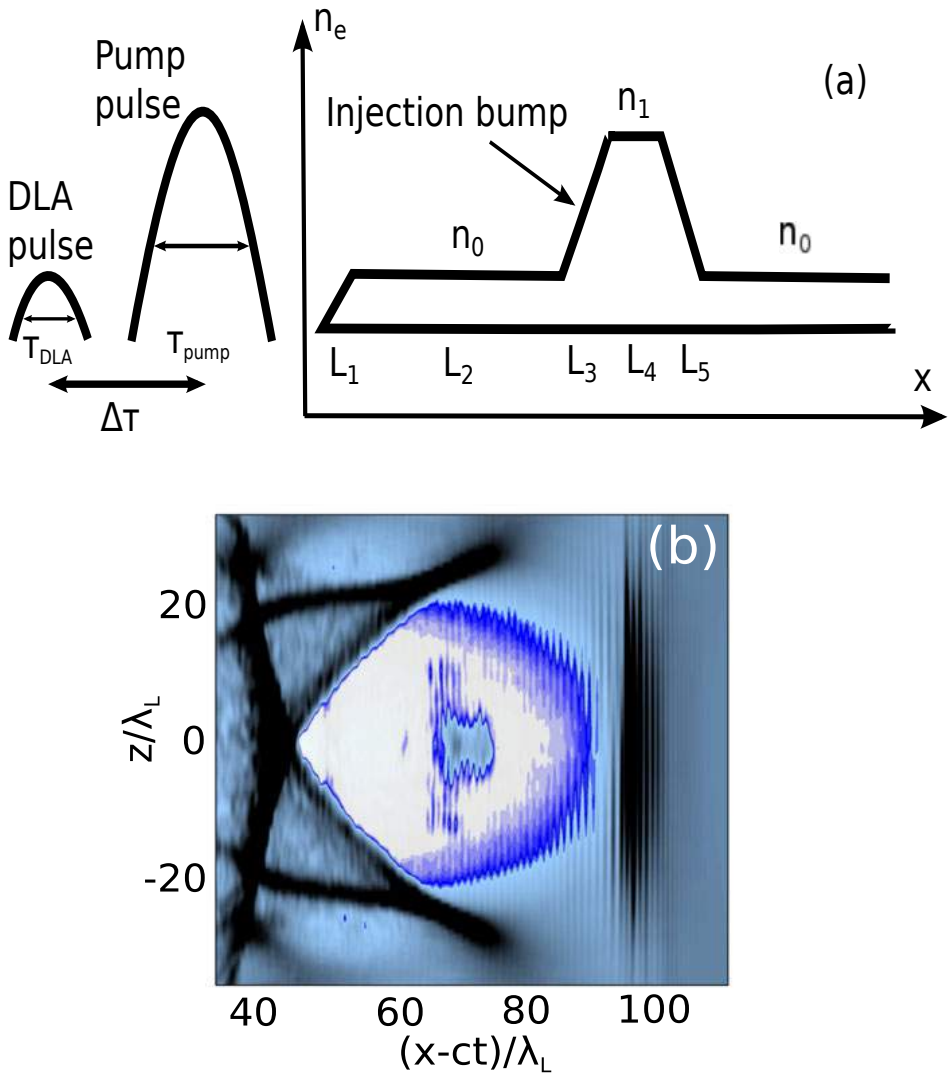

FIGURE 2.3: (a) Schematic representation of the laser pulse format and plasma density profile. (b) Plasma electron density in the bubble regime at $x = 1\,cm$; self-injected electron bunch inside the plasma bubble has advanced approximately to the middle of the bubble. Plasma parameters: $L_1 = L_2 = L_3 = L_4 = L_5 = 0.1\,mm$, $L_2 = 1.6\,mm$; $n_0 = 1.8{\times}10^{18} cm^{-3}$, $n_1 = 3n_0$. Laser parameters: $I_{pump} = 2{\times}10^{19} W/cm^2$, $I_{DLA} = I_{pump}/5$, pulse durations $\tau_{pump} = 50fs$ and $\tau_{DLA} = 30fs$, inter-pulse time delay $\Delta\tau = 67fs$.

The plasma bubble density structure is shown in Fig. 2.3(b). The plasma bubble has a well-defined sheath and the electrons are almost completely blown out. The

density bump injected electrons are trapped in the plasma bubble and accelerated for more than 1 cm. In Fig. 2.3(b), the electron beam has passed the center of the plasma bubble and reached the dephasing regime. This one-time injected electron beam has some unique LWDA features such as the different spatial distributions of the groups within the electron beam and wide transverse diverge. We will come back to the LWDA electron beam later. In conclusion, the density-bump injection is efficient to inject electrons that meet the LWDA requirements.

2.2.3 Ionization Induced electron injection

Laser-based electron injection mechanisms can also be used in LWDA. The injection must provide the electrons with certain initial transverse energy $\varepsilon_{\perp 0}$. It is also important that the injection mechanism is stable and relatively easy to realize.

We investigate the ionization induced injection. Ionization injection is considered particularly straightforward because of its relative controllable and stable features. It produces electron beams with high emittance. Recently, it has been theoretically shown to be promising for producing low-emittance beams [75, 76]. We want that the ionization produce electrons have certain initial transverse energy $\varepsilon_{\perp 0}$ to fulfill the initial requirement of LWDA. This is on the opposite way of the above mentioned research for LWFA but it may turn one of the drawbacks of the ionization induced injection to an advantage. The first requirement of LWDA is still fulfilled by the time-delayed DLA pulse.

We use in 2D PIC code VLPL with the ADK DC ionization model [77] to study the ionization injection in LWDA. The schematic representation is shown in Fig. 2.4.

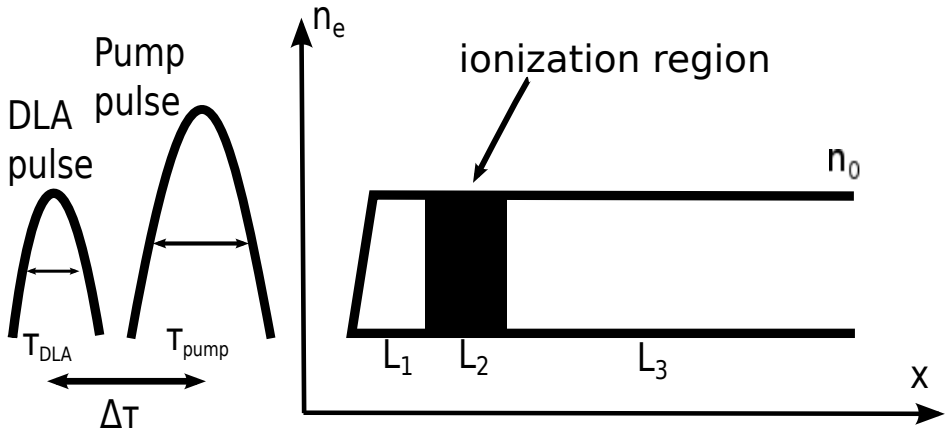

FIGURE 2.4: Schematic representation of the laser pulse format and plasma density profile. Plasma parameters: $L_1 = 80\,\mu m$, mixed gas length $L_2 = 100\,\mu m$, $L_3 = 3\,mm$; $n_0 = 4.0{\times}10^{18} cm^{-3}$, $n_{O^{7+}} = 0.1 n_0$, ionization potential for $O^{7+} \rightarrow O^{8+}$ $U_{ion} \approx 871.4\,eV$ $\lambda_p = \frac{2\pi c}{\omega_p} = 17\mu m$. Laser parameters: wavelength $\lambda_L = 0.8\mu m$, $I_{pump} = 2.3{\times}10^{19} W/cm^2$, $I_{DLA} = I_{pump}/2$, pulse durations $\tau_{pump} = 20fs$ and $\tau_{DLA} = 15fs$, spot size $W_{pump} = 17\mu m$ and $W_{DLA} = 13\mu m$, inter-pulse time delay $\Delta\tau = 61fs$.

Multi-terawatt ($P_{pump} = 96TW$ and $P_{DLA} = 28TW$) pump and the time-delayed DLA pulses are assumed in the simulation. Instead of engineering a density bump [27] for injecting electrons with large transverse energy, the injection due to the ionization of high-Z oxygen ions ($O^{7+} \rightarrow O^{8+}$) is modeled in the simulation. The $100\,\mu m$ gas mixture region consisting of 90% He and 10% O_2 is shown as a dark area in Fig. 2.4. The leading edge of the pump pulse fully ionizes helium and the low-charge states of oxygen ions, thereby creating a background plasma with the density $n_0 = 4.0{\times}10^{18} cm^{-3}$ which is pushed aside by the pump pulse to create a plasma bubble. The K-shell oxygen's electrons are produced via ionization close to the peak of the pump pulse intensity. Therefore, these electrons are injected and get trapped inside the plasma bubble [70, 78, 79, 80]. The pump pulse thus serves a dual role of

producing the plasma bubble and injecting the electrons into it. From the experimental point of view, ionization injection is easier to implement than a short density bump. The basic setup is similar as the density bump injection discussed above but we have the uniform plasma density now. The plasma bubble is not destroyed during all the propagation distance. The dark region is the mixed gas of the helium and the oxygen. As discussed above, the inner shell electrons of the oxygen atom have high ionization potential. They are used as the dopping gas for the ionization injection. There are experiments that used oxygen as the dopping gas to do the ionization injection [78].

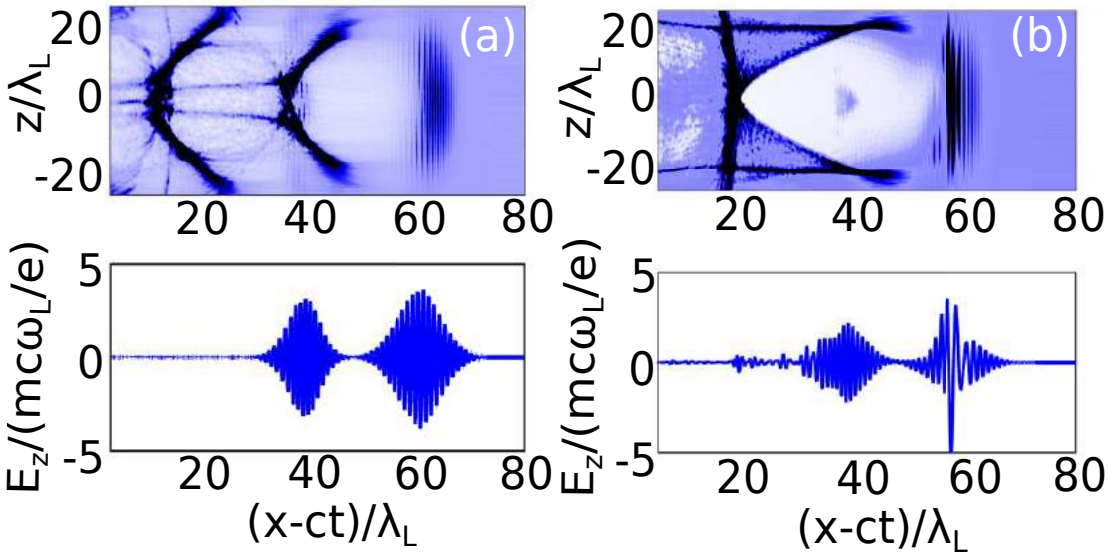

FIGURE 2.5: (a) Plasma electron density (top) and the on-axis laser field E_z at $x = 320\mu m$. (b) Same as (a), but at $x = 2.6mm$.

The results of the PIC simulations are presented in Figs. 2.5 (a,b) for $x = 320\mu m$ (right after the lasers passing though the ionization region) and $x = 2.6mm$ (peak energy gain), respectively. The ADK tunneling ionization model [68, 77, 81] is

used to describe the release of the K-shell electrons from the oxygen ion. Fig. 2.5(a) represents the propagation distance that the laser pulse just exits the mixed gas region. The ionization induce injection has already happened. It is apparent from the top panel of Fig. 2.5(a) that the majority of trapped electrons are concentrated at the bottom of plasma bubble where the DLA pulse is located. As the laser pulses and the plasma bubble propagates through the plasma, the injected electrons advanced forward through the bubble due to dephasing. Even after the electrons reach the middle of the bubble as shown in Fig. 2.5(b), their overlap with the DLA pulse is well maintained. The reason is that the DLA pulse, which propagates inside the plasma bubble, has a highly relativistic group velocity ($\gamma_{DLA} \approx 40$) that is larger than that of the bubble group velocity ($\gamma_{bubble} \approx 15$) and very close to the longitudinal velocity of the DLA electrons. The expansion of the plasma bubble [43, 44, 45] observed by comparing the top panels of Figs. 2.5(a) and (b) also plays a role in maintaining excellent overlap between the DLA pulse and the injected electrons near the middle of the plasma bubble.

The results presented in Fig. 2.5 explain the requirement of the overlap between the DLA pulse and the injected electrons. It is not surprising that the ionization injection happens. To understand how laser-ionized electrons can acquire large transverse energy necessary for DLA, we need to recall the specifics of ionizing an atom in a laser field that greatly exceeds the atomic electric field $E_a = e/r_e^2 \approx 5.1 GV/cm$, where $r_e = e^2/m_e c^2$ is the classical electron radius. According to the ADK tunneling ionization model [68, 77, 81], the ionization rate is given Eq. (2.2). For the $O^{7+} \rightarrow O^{8+}$ oxygen ionization we estimate that $C \approx 8.4\times10^4$, $d \approx 1$ and $E_{rm} \approx 1.7\times10^3 GV/cm$. ADK tunneling ionization model implemented in VLPL [77,

81] assumes that the ionization rate is given by Eq. (2.2). From Eq. (2.2) we conclude that for the peak on-axis electric field of the laser $E_0 = 3.5 m_e c \omega_L / e$ and the pulse duration of $\tau_{pump} = 20 fs$, the product $W(E_0)\tau_{pump} \gg 1$. This means that an O^{7+} laser axis is ionized to its O^{8+} state with nearly 100% probability. This also implies that an atom experiencing a weaker instantaneous field $E_L < E_0$ can also lose an electron with significant probability. In the near-static tunneling limit of $\omega_L < \omega_a$ electron tunneling may occur according to the following scenarios: (a) at $z \neq 0$ (off-axis tunneling), or (b) at $z = 0$, but at the electric field's phase φ that does not correspond to its maximum (off-peak phase ionization). Of course, all intermediate scenarios are also possible, so the (a) and (b) are the two limiting cases that supply ionization-produced electrons with finite transverse energy $\varepsilon_\perp$necessary for DLA acceleration. The scenarios (a) and (b) are illustrated by Fig. 2.6(a) and Fig. 2.6(b) respectively.

The motion of an ionized electron born at rest inside the pump pulse can be broken up into three stages: (i) ionization and direct interaction with the pump laser pulse, (ii) initial trapping in the bubble, and (iii) final acceleration by the combination of LWFA and DLA mechanisms. The first two stages are very short and results in the electron's energy gain of the order of $\gamma_b m_e c^2$. The third stage is the longest one; it results in the final energy gain exceeding $\gamma_b^2 m_e c^2$. Because the third stage of the electron acceleration in an LWDA will be studied after the discussion of the injection, below we concentrate mostly on the first and second acceleration stages, as well as on the earliest times of the third stage.

During the first stage of the duration $\Delta\tau_1 \approx \tau_{pump}$ the electron born at t_i at $(x = x_i, z = z_i)$ interacts primarily with the pump pulse. This interaction is best

described using the (approximate) conservation of the transverse canonical momentum as mentioned in the chapter 1: $\frac{p_z(t)}{m_e c} - a_z(z(t), t) = \frac{p_z(t_i)}{m_e c} - a_z(z_i - t_i)$ where $a_z = eA_z/m_e c^2$ is the normalized canonical momentum of the laser. This approximation is valid as long as the laser spot size satisfies $W_{pump} \gg z_{wiggle}$ where z_{wiggle} is the wiggling amplitude of the newly-ionized electron in the laser field. Combining the $a_z(t) = 0$ for $t > t_i + \tau_{pump}$ condition with $p_z(t_i) = 0$, we obtain $\frac{p_{z0}}{m_e c} = -a_z(z_i, t_i)$ at the end of the first stage.

Assuming that $A_z = cg(z)E_0 \cos\left(\omega_L\left(t - \frac{x}{v_{ph}}\right)\right)/\omega_L$, where $g(z)$ is the transverse laser profile normalized as $g(z = 0) = 1$, we obtain [75, 76]

$$p_{z0} = -g_{z_i}\frac{eE_0}{m_e c\omega_L} cos\varphi_i, \tag{2.7}$$

where $\varphi_i = \omega_L(t_i - x_i/v_{ph})$ is the laser phase at the moment of electron's tunneling from an oxygen ion in the electric field of the magnitude $|E_i| = E_0 g(z_i)|sin\varphi_i|$. By definition, the peak-phase ionization corresponds to $\varphi_i = \pi/2$ and vanishes for transverse momentum p_{z0}, while the off-peak ionization corresponds to $\varphi_i \neq \pi/2$ and $p_{z0} \neq 0$. Therefore, those electrons born far off-axis are likely to be produced by peak-phase ionization and to have small p_{z0}. On the other hand, the on-axis electrons can be ionized during the off-peak phase of the laser and have a relativistic $p_{z0} \approx eE_0/m_e c\omega_L$. However, both off-axis and off-peak electrons can have a substantial initial transverse energy $\varepsilon_{0\perp} = \frac{p_{z0}^2}{2\gamma_0 m_e} + m_e\omega_p^2 z_0^2/4$ (where $z_0 = z_i$) that is necessary for effective DLA.

The second stage involves electron motion toward the back of the bubble and its subsequent trapping. Because of the brevity of the first stage, we assume that the electron's initial conditions established for the second stage are $(z_0, p_{z0}, x_i, p_{x0} = 0)$. Assuming that the bubble does not have sufficient time to evolve during the second

stage, we can take advantage of the conservation of the Moving Frame Hamiltonian (MFH) [26, 43, 44, 45, 70] given by Eq. (2.1). Using the results of the PIC simulations, we can approximately calculate $\Psi(\xi, z)$ at any instance of time according to $\Psi = \int_{\xi_{min}}^{\xi_{max}} E_x d\xi$, where E_x is the longitudinal electric field, and the integration is carried out over the entire moving computational window that encompasses the plasma bubble. The contours of constant $e\Psi(\xi, z)/m_e c^2$ calculated at $x = 120\mu m$ inside the ionization region shown in Fig. 2.4 are presented in Fig. 2.6(a) and Fig. 2.6(b). For this particular case we have found that the maximum value of Ψ reached at the center of the bubble is $\Psi_{max} \approx 3.1 m_e c^2$ while its minimum value at the bottom of the bubble is $\Psi_{min} \approx 0.1 m_e c^2$.

It is instructive to simplify the expression for the MFH in the two important limits: at the end of the first acceleration stage, when $p_x/m_e c \ll \gamma_0 \approx 1$, and at the end of the second stage, when $\gamma_b \leq \gamma_0 \ll \gamma_b^2$. In the former case we can assume that $H_0 \approx \gamma_0 m_e c^2 - e\Psi(\xi_i, z_i)$ while in the latter case $H_f \approx -e\Psi(\xi_t, z_t)$, where $(\xi_{t,i}, z_{t,i})$, are the coordinates of electrons birth/trapping inside the plasma bubble. From $H_0 = H_f$ we derive the following trapping condition for the electrons:

$$\Psi_i - \Psi_f \approx \frac{m_e c^2}{e} \gamma_0 \sim 1, \tag{2.8}$$

where $\Psi_i = \Psi(\xi_i, z_i)$ and $\Psi_f = \Psi(\xi_f, z_f)$.

The constant-Ψ contours can be used for a simple graphical interpretation of the trapping condition given by Eq. (2.8). If an electron is born on the Ψ_i contour, then it will slip out of the bubble if $\Psi_i < \Psi_{min} + \gamma_0 m_e c^2/e$. This condition is exemplified by a representative magenta-colored electron shown in Fig. 2.6(b) born at the leading edge of the pump. This electron, which starts insufficiently deep inside the bubble with $\Psi_i \approx 0.5 m_e c^2$, does not get trapped inside the bubble. On the other

hand, all other representative electrons shown in Figs. 2.6 that are born deep inside the bubble ($\Psi_i > 1.2m_ec^2$) end up trapped inside the bubble because the trapping condition $\Psi_i > \Psi_{min} + \gamma_0 m_e c^2/e$ is satisfied for them.

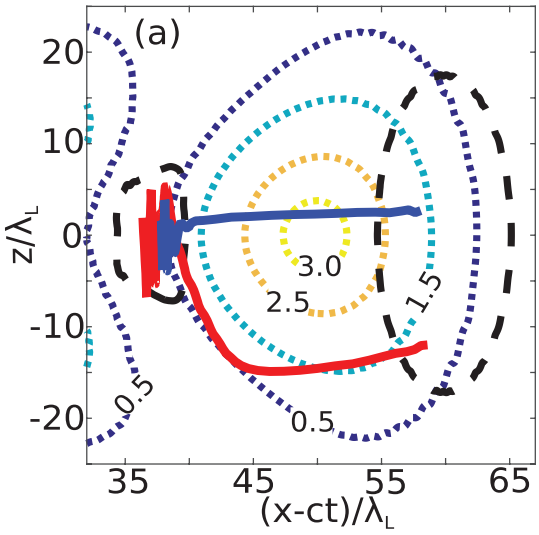

FIGURE 2.6

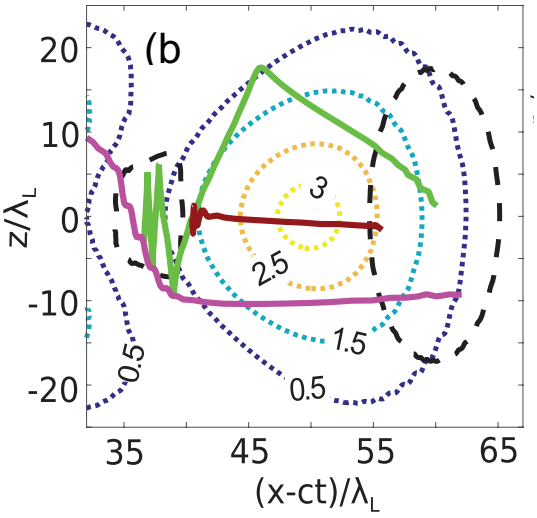

FIGURE 2.6: The ionization injection process in the plasma bubble. Colored dotted curves: the labelled $\frac{e\Psi(\xi,z)}{m_e c^2} = const$ contours of the wake's potential. Black dashed curves: $\frac{E_z}{E_z^{max}} = 0.45$ contour inside which 99% of ionization events takes place. (a) Trajectories of the off-axis DLA (red solid curve) and non-DLA (blue solid curve) electrons. (b) Same as in (a), but for a different set of ionization-injected electrons: the untrapped (magenta line), the deeply trapped non-DLA (brown line), and the ricochet DLA (green line) electrons.

2.3 Electron Dynamics in Laser Wakefield and Direct Acceleration

2.3.1 Electron Distribution and Phase Space

We demonstrated the density bump injection and the ionization induced injection are able to produce the electron beams that satisfy the initial condition requirements. The time-delayed DLA pulse is capable of providing sufficient DLA without disturbing the plasma bubble too much. In this section, we focus on the acceleration of LWDA for both the density bump injection and the ionization induced injection.

We first look into the density bump injection LWDA in detail. The density structure of the plasma bubble and the injected electron beam after propagating for $x = 1cm$ through the plasma are shown in Fig. 2.3(b). As the injected electrons, they advance towards the center of the bubble and experience dephasing, a clear separation

into DLA and non-DLA groups occurs. Electrons color-coded according to their final energy are shown in Fig. 2.7(a), which is a zoom-in of Fig. 2.3(b) in the vicinity of the bubble's center indicated by a vertical black line. Clearly, the highest energy electrons comprising the DLA group have a much larger betatron oscillation amplitude, and are spatially located behind the lower-energy non-DLA group of electrons. The laser-delayed dephasing is apparent. The dephasing rate $\frac{d\xi}{dt} = v_x - v_b$ is suppressed by the resonant excitation of the Betatron oscillation according to Eq. (2.6). DLA electrons advance slower through the bubble because they have much higher transverse momentum (up to $p_z = 100 m_e c$) imparted directly by the DLA pulse.

$$\frac{d\xi}{d(ct)} = \frac{1}{2\gamma_b^2} - \frac{1 + \langle p_z^2/m_e^2 c^2 \rangle}{2\gamma^2}, \tag{2.9}$$

In Eq. (2.9), the first term in the right hand side is determined by the plasma bubble and the second term in the right hand side is changing due to the electron acceleration. Large transverse momentum p_z increases this term and decreases the dephasing rate. The DLA electrons have larger transverse momentum p_z and smaller dephasing rate than non-DLA electrons.

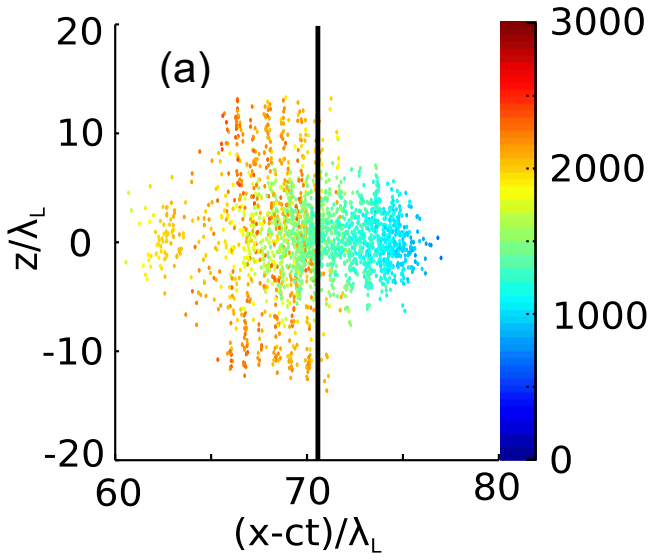
(a)
20
10
0
-10
-20
z/λL
60
70
80
(x-ct)/λL
3000
2000
1000
0

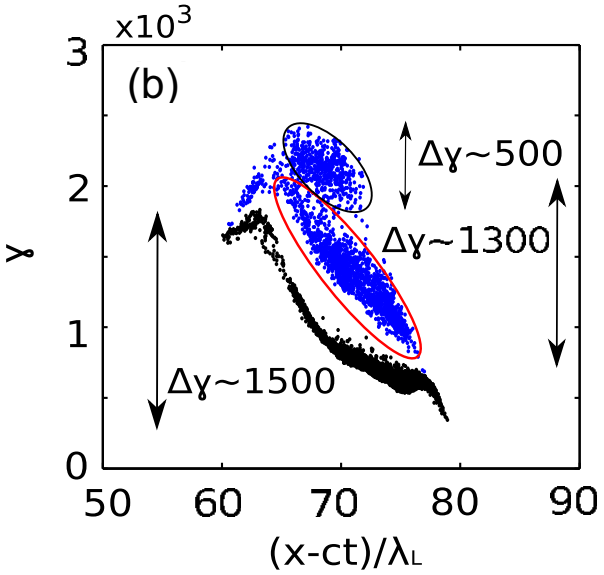
x10^3
(b)
3
2
1
0
γ
Δγ~500
Δγ~1300
Δγ~1500
50
60
70
80
90
(x-ct)/λL

FIGURE 2.7

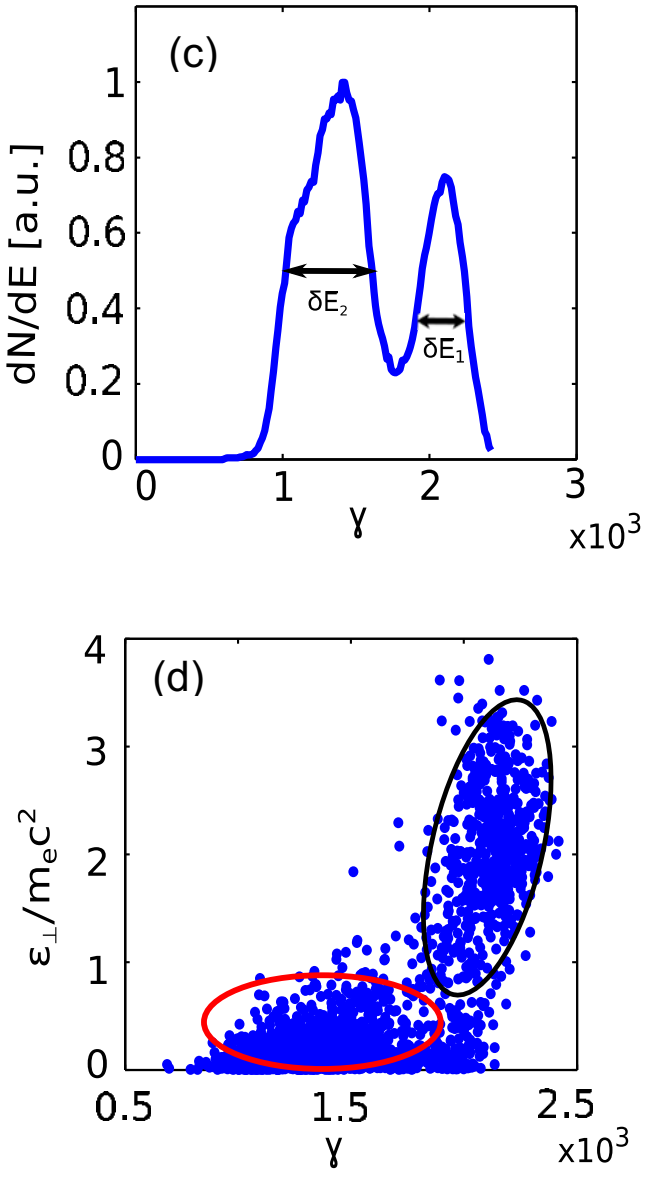

FIGURE 2.7: (a) Zoom-in of the self-injected electrons color-coded according to their relativistic factor γ; black vertical line: bubble's center. (b) Phase space of self-injected electrons for double-pulse (blue dots) and single-pulse (black dots) laser formats. (c) Energy spectrum for double-pulse (pump + DLA) formats. Energy spreads: $\delta E_1 \approx 350 m_e c^2$, $\delta E_2 \approx 600 m_e c^2$. (d) Bifurcated phase space $(\gamma, \epsilon_\perp)$ shows correlation between total and transverse energies for DLA electrons.

The bifurcated $(x - ct,\ \gamma)$ phase space and the total energy spectrum of the accelerated electrons are plotted in Figs. 2.7(b, c), respectively (blue-colored). The DLA (black-circled) and non-DLA (red-circled) electrons are clearly separated in energy and space, with their energy spectra peaking at $\varepsilon_{tot}^{DLA} = 1.1\ GeV$ and $\varepsilon_{tot}^{DLA} = 0.65\ GeV$, respectively. To illustrate the role of the time-delayed DLA laser pulse on phase space bifurcation, we carried out PIC simulations for the single-pulse LWFA case, i.e. with the same bubble-producing pump pulse ($I_{pump} = 2{\times}10^{19} W/cm^2$ corresponding to $a_{pump} = 3$) but no DLA pulse. The resulting electron phase space shown in Fig. 2.7(b) (black dots) do not show any phase space fragmentation, thus indicating that no DLA electrons are produced. We note in passing that the energy gain in the single-pulse case is somewhat smaller than for non-DLA particles in the two-pulse case because of the slightly weaker accelerating wake in the former case, apparently due to stronger on-axis beam loading. The injected electrons have wider transverse spread in the two-pulse scenario than the injected electron in pump-pulse scenario. Another intriguing difference between the two groups of electrons is observed by plotting the $(\gamma, \epsilon_\perp)$ phase space in Fig. 2.7(d). While there is no correlation between γ and $\epsilon_\perp$ for the non-DLA group, a strong positive correlation exists for the DLA group. A relativistic beam with finite emittance and energy spread possessing such correlation between total energy and transverse action of its electrons is referred to as conditioned [82]. It has been suggested that beam conditioning [82, 83, 84, 85, 86] can considerably improve gain and efficiency of FELs if the correlation between γ and $\epsilon_\perp$ is such that any deviation of individual electron's energy $\Delta\gamma_i = \gamma_i - \gamma_d$ from the design energy γ_d is compensated by the

corresponding increase in its transverse energy $\epsilon_{\perp i}$ so that there is no spread in the longitudinal velocity Δv_{xi} is minimized.

We have investigated all the electron distribution and the phase space of LWDA in the density bump injection. The next step is to study the LWDA electrons in the ionization induced injection. The same techniques and phase space are used for the reason of the easy comparisons. We show the electron spatial distribution, energy spectrum and the $(\gamma, \epsilon_{\perp})$ phase space in the following Figs. 2.8.

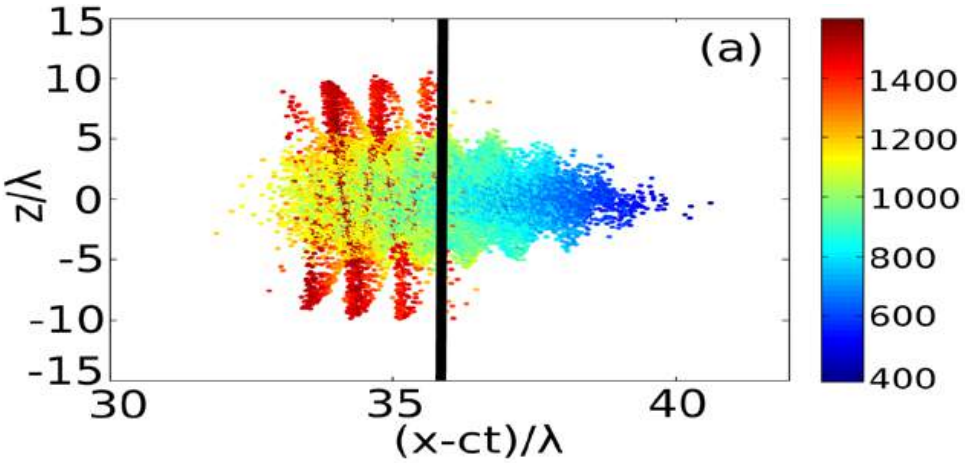

FIGURE 2.8

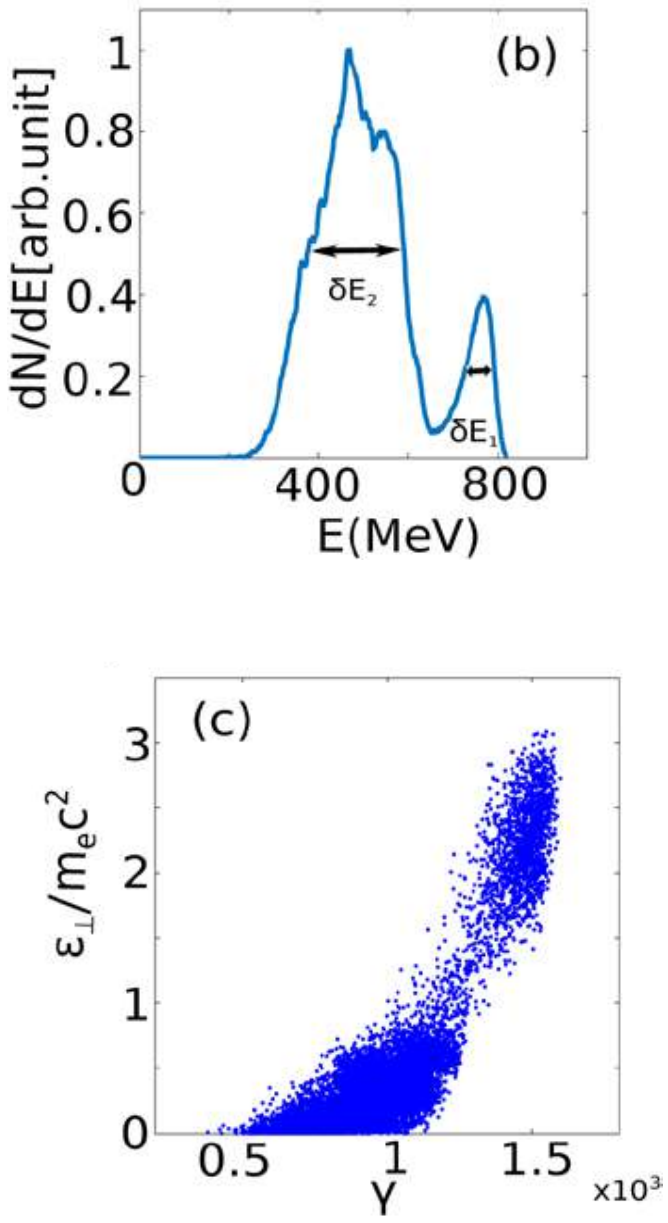

FIGURE 2.8: Spatial distribution of the ionization injected electrons color-coded according to their relativistic factor γ at $x = 2.6\,mm$; black vertical line: bubble's center. (b) Energy spectrum for injected elelctrons. Energy spreads: $\delta E_1 \approx 60\,MeV$, $\delta E_2 \approx 230\,MeV$. (c) Bifurcated phase space $(\gamma, \epsilon_\perp)$ shows positive correlation between total and transverse energies for DLA electrons.

Close observation of Fig. 2.5(b) and its zoomed-in version in Fig. 2.8(a) shows that DLA and non-DLA particles are spatially separated in x. This is the consequence of Eq. (2.6) which predicts that DLA electrons with large betatron amplitudes advance less through the bubble than the non-DLA electrons. The resulting phase space bifurcation in the LWDA is apparent from Fig. 2.8(a), where the injected electrons are color-coded according their total energy γmc^2, and the vertical black line indicates the center of plasma bubble ($E_x \approx 0$). The high-energy DLA group of electrons is located behind the lower-energy non-DLA group, which is already in the decelerating region of the bubble.

The total energy spectrum of the accelerated electrons is plotted in Fig. 2.8(b). The spectrum has two peaks which represent the DLA ($\gamma^{DLA}mc^2 \approx 770\ MeV$) and non-DLA electrons ($\gamma^{n-DLA}mc^2 \approx 450\ MeV$), respectively. The DLA effect does not compromise the beam's energy spread; in fact, the energy distribution of the DLA electrons is considerably lower than that of the non-DLA electrons.

Below we present a quantitative statistics of the ionized electrons. The number of trapped electrons is about 90% of all electrons released by oxygen ionization. There are about 13% of electrons undergoing significant DLA within the group of trapped electrons or about 11% within the group of all electrons released by ionization. DLA electrons form a sub-population of high transverse energy electrons, that were born either off-axis or off-peak phase. The ADK ionization rate is relatively small when it is off-axis or off-peak phase. So the number of DLA electrons is smaller than the number of non-DLA electrons.

Due to the 2D geometry, we can only roughly estimate the charge yield. The beam density is $n \approx 8{\times}10^{17} cm^{-3}$ at the propagation distance $x = 2.6mm$ as

shown in Fig. 2.8. The length of the beam is about $L_b \approx 6\mu m$ and the radius is about $r_b \approx 4\mu m$. We estimate that there is about 40pC charge in the beam.

Another intriguing difference between DLA and non-DLA electrons is revealed in Fig. 2.8(c) which shows the bifurcated $(\gamma, \epsilon_\perp)$ phase space of the accelerated electrons. The DLA group exhibits a clear positive correlation between γ and $\epsilon_\perp$ while there is no such correlation for the non-DLA group. Both the double-peaked energy spectrum and the bifurcated phase space are reminiscent of the earlier results obtained using the density bump injection [27]. Therefore, the synergistic LWFA and DLA mechanisms can be realized in an accelerator with ionization injection.

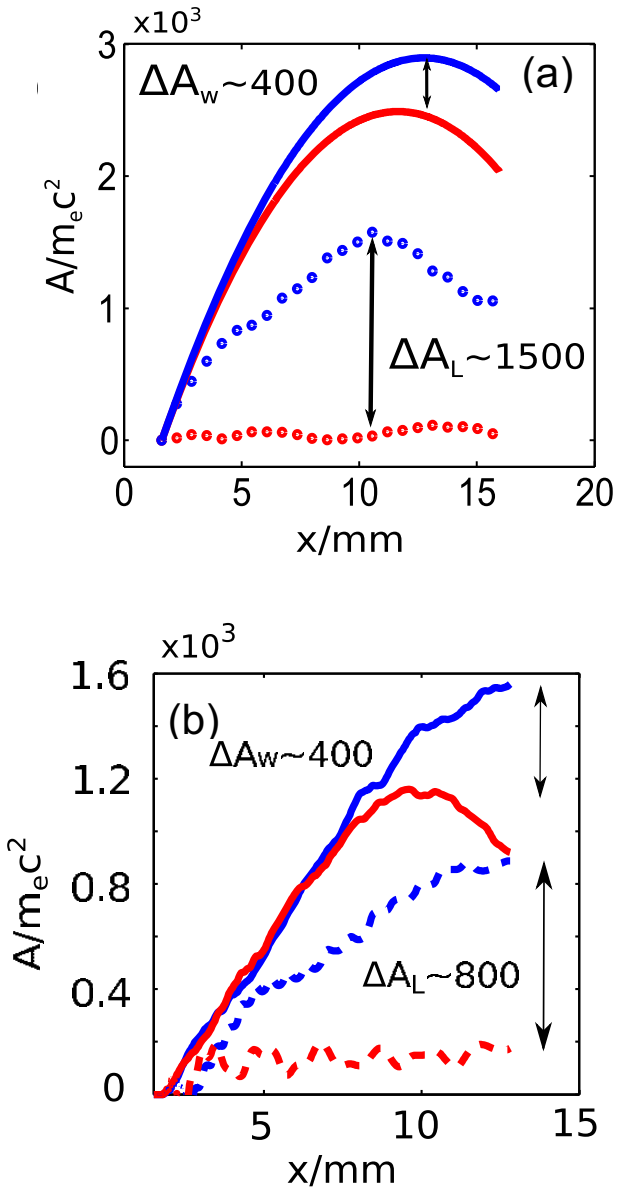

FIGURE 2.9: (a) Single particle model: Energy gain from the laser/wake (A_L: dashed lines, A_w: solid lines) for two test electrons with initial conditions marked in Fig. 2.2(a) by circles. Blue lines: DLA, red lines: non-DLA test electrons. (b) PIC simulation: Energy gain from the wake (A_w: solid lines) and laser (A_L: dashed line) fields for DLA (blue) and non-DLA (red) representative electrons.

2.3.2 Synergestic Nature of Electron Acceleration

The density bump injection and the ionization induced injection perform well in the LWDA. The LWDA can significant boost the electron energy by combining the LWFA and the DLA in the plasma bubble regime. We have studied the electron distribution and phase space. In this section, we look into the detail of the electron dynamics during the acceleration stage of both the density bump injection and the ionization injection.

Before moving into the self-consistent PIC simulations, we first investigate the laser and wake energy gains of two representative DLA (blue) and non-DLA (red) electrons marked by the black circles in Fig. 2.2(a) with initial transverse energies $\epsilon_{\perp 0} = 0.8 m_e c^2$ and $\epsilon_{\perp 0} = 0.1 m_e c^2$, respectively, are compared in Fig. 2.9(a). One important phenomenon is clear from the comparison. The synergistic nature of the hybrid DLA/LWFA: the DLA electron gains more energy from the wake than a non-DLA electron, with the difference of ($\Delta A_w \approx 0.2\ GeVs$) being due to delayed dephasing. At the same time, the DLA electron gains ($\Delta A_L \approx 0.7\ GeV$) energy from the laser, thereby almost doubling its total final energy $\varepsilon_{tot} = \gamma m_e c^2$ compared with its non-DLA counterpart. From our single particle model, we find that the LWDA is not simply the energy add-up. The DLA electrons have much larger wiggling motion than the non-DLA electrons. They stay in the plasma bubble accelerating field longer than the non-DLA electrons. Therefore, the DLA electrons gain more energy than the non-DLA electrons.

We move into the self-consistent PIC simulation to confirm the synergistic nature of the LWDA. The synergistic nature of the DLA and LWFA mechanisms can be demonstrated by comparing the LWFA gains A_w plotted in Fig. 2.9(b) for two

representative DLA and non-DLA electrons. Because it is impossible to rigorously separate laser and wake fields in PIC simulations, the energy gains A_L and A_w from the laser and wake were estimated [19] as $A_L = -\int eE_z v_z dt$ and $A_w = -\int eE_x v_x dt$, respectively, where $E_{x;z}$ is the electric field extracted from the PIC simulations. Even though the finite E_x component of the laser pulse makes a non-vanishing contribution to A_w for the off-axis electrons, we estimate that this contribution is much smaller than the contribution of the plasma wake. From Fig. 2.9(b) we observe that the non-DLA electron gains less energy than the DLA electron, and promptly moves into the decelerating phase of the bubble's field (red solid line). The DLA electron does not experience. dephasing (blue solid line), resulting in a much larger wake energy gain A_w. Additionally, the DLA electron gains considerable energy ($A_L \approx 900 m_e c^2$) directly from the laser. The combination of larger gains from the wake ($\Delta A_w \approx 400 m_e c^2$) and from the laser ($\Delta A_L \approx 800 m_e c^2$) explains why DLA electrons acquire much higher total energy $\gamma m_e c^2$ than non-DLA electrons [see Fig. 2.9(b) for definitions of ΔA_w and ΔA_L]. The synergistic acceleration in LWDA with the density bump injection is clear by looking into the time evolution of the electron energy gain. We study more details of the electron dynamics in the ionization injection.

Now we consider the acceleration stage involving the long-term interaction of the trapped electrons with the DLA pulse and with the bubble's wakefield. The long-term trajectories of two typical trapped electrons that are shown in Fig. 2.6(a) are plotted over a distance of $x < 0.8mm$ after their ionization in Figs. 2.10. The electrons are chosen to belong to the DLA (red) and non-DLA (blue) groups. The pump laser's intensity contour shown with a dashed line was chosen in such a way that 99% of all

ionization events take place inside the contour based on ADK the tunneling ionization model [68, 77]. We observe that the non-DLA electron is born near the axis and during the peak ionization phase $\phi_i \approx \pi/2$. Therefore, this electron does not acquire any significant initial transverse energy $\epsilon_{\perp 0}$ during the first acceleration stage.

Even though the non-DLA electron spatially overlaps with the DLA laser pulse as illustrated in Fig. 2.6(a), its interaction with the laser is weak because its initial transverse energy is small. On the other hand, the DLA electron is produced via off-axis peak-phase ionization at $z_i = 11\lambda$ with considerable $\epsilon_{\perp 0}$.

The long time acceleration of these two representative electrons shown confirms their classification as DLA and non-DLA. The energy gains $A_L = -\int eE_z v_z dt$ and $A_w = -\int eE_x v_x dt$ from the wake are plotted in Figs. 2.10(c, d), respectively. The DLA electron gains much more energy ($\Delta A_L \approx 700 m_e c^2$) directly from the laser than non-DLA electron. Meanwhile, the DLA electron also gains more energy ($\Delta A_w \approx 100 m_e c^2$) from the wake than a non-DLA electron because of the delayed dephasing predicted by Eq. (2.6) due to its large transverse momentum p_z as shown in Fig. 2.10(a). The delayed dephasing of the DLA electron with respect to the non-DLA one is observed by comparing the peaks of the two $A_w(x)$ curves in Fig. 2.10(c). The non-DLA electrons lose about 50-100 MeV due to the dephasing. The combination of these two factors provide the DLA electron with much larger higher peak energy $\gamma m_e c^2$ as shown in Fig. 2.10(b).

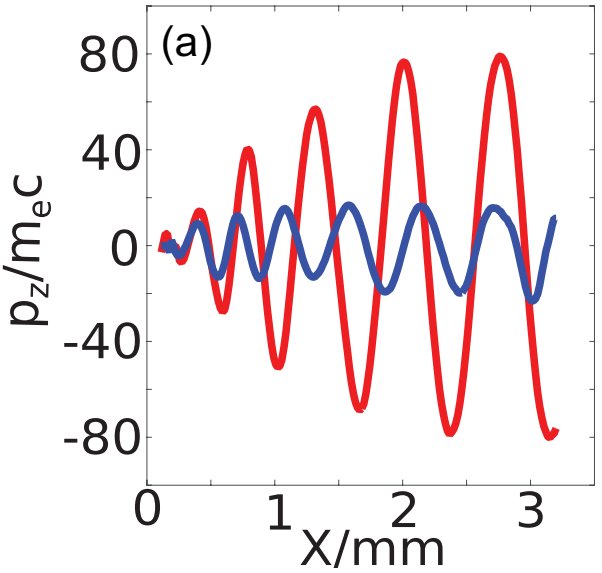

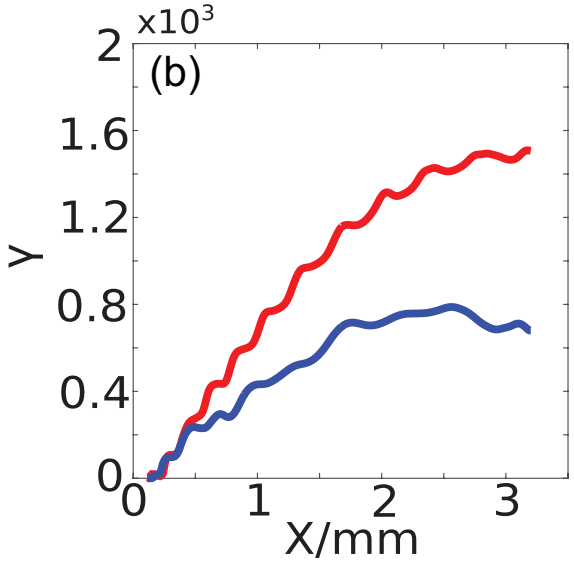

FIGURE 2.10

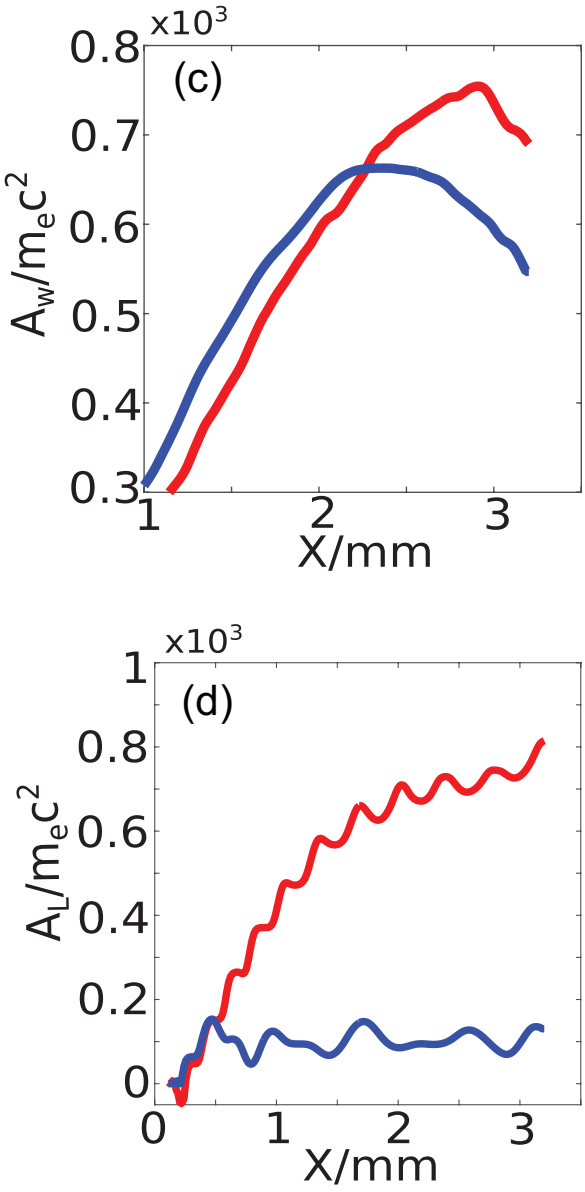

FIGURE 2.10: (a)-(d) The long-term evolution of the transverse momentum p_z, relativistic factor γ, the work A_w done by the wake, and work A_L done by the laser for the same representative electrons as in Fig. 2.6(a).

Two more electron injection and acceleration scenarios are illustrated in Fig. 2.6(b), where the trajectories of a non-DLA (brown-colored) and DLA (green-colored) trapped electrons are shown in Figs. 2.11. The non-DLA electron is born near the trailing edge of the pump pulse deep inside the bubble at $\Psi_i \approx 2.5 m_e c^2/e$. The conservation of the MFH expressed by Eq. (2.1) implies that the electron does not reach the back of the bubble and, therefore, does not overlap with the DLA pulse. The direct laser energy gain A_L is, therefore, negligible, i.e. even smaller than for the non-DLA electron analyzed in Fig. 2.10.

The DLA electron shown in Fig. 2.11 exemplify the electrons injected via the off-peak phase tunneling [87]. Even though the electron is produced by laser ionization on-axis, its trajectory shown in Fig. 2.6(b) clearly indicates that it has a large transverse momentum after the first acceleration stage. The initial transverse momentum of the electron is estimated to be $P_{0z} \approx 2.2\, m_e c$. Because of its unusual trajectory that involves several bounces off the edge of the plasma bubble before overlapping with the DLA pulse and undergoing further acceleration, we refer to such particles as "ricochet" electrons. By following the long-term acceleration of the ricochet DLA electron shown in Figs. 2.11(a)-(d), we conclude that the efficiency of DLA is comparable for the electrons produced via off-axis and off-peak tunneling. Therefore, we conclude that the DLA electrons injected into the bubble via ionization injection roughly belong to two categories: the off-axis ionized and the off-peak phase ionized (ricochet) electrons.

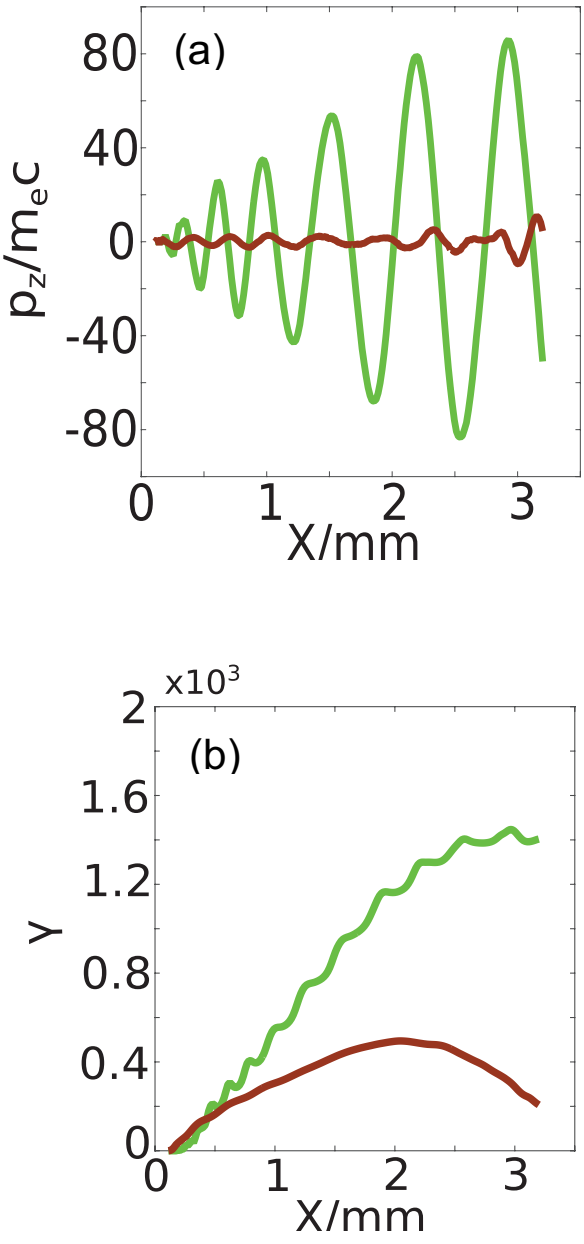

FIGURE 2.11

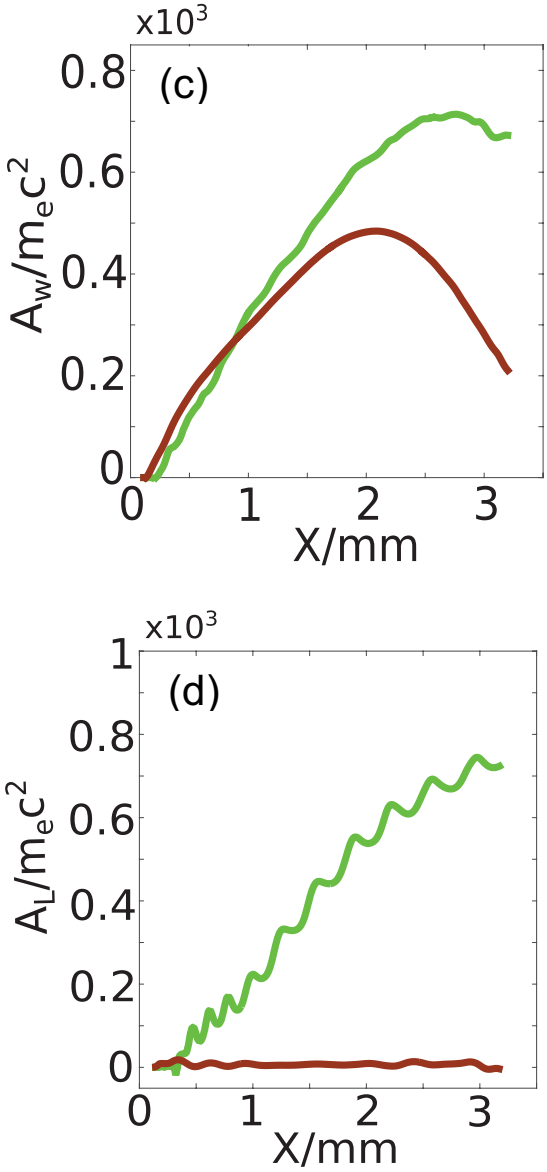

FIGURE 2.11: (a)-(d) The long-term evolution of the transverse momentum p_z, relativistic factor γ, the work A_w done by the wake, and work A_L done by the laser for the green and brown representative electrons as in Fig. 2.6(b).

2.4 Summary

In conclusion, we have proposed and theoretically demonstrated a new type of a plasma-based accelerator: a hybrid laser wakefield/direct laser accelerator. The synergistic nature of the LWFA/DLA mechanism manifests itself in compounding the distinct energy gains from the plasma wake and directly from the laser pulse while increasing the former because of the delayed dephasing caused by the latter. Phase space bifurcation of the self-injected electrons into two distinct groups of high-energy DLA and lower-energy non-DLA particles is demonstrated. We also demonstrate that ionization injection is suitable for a laser wakefield and direct accelerator (LWDA). We find that the electrons' phase space is similar to the density bump injection and the energy spectrum is split into two peaks corresponding to two sub-populations. By tracking several electrons with different initial condition, we demonstrate that DLA electrons born inside the plasma bubble must have significant transverse energy. Two ways of gaining such energy are discovered using PIC simulations: electrons must be generated either via off-axis of via off-peak phase tunneling. With the introduction of ionization injection, the hybrid laser wakefield and direct laser plasma accelerator may potentially become more stable and controllable. Future work will explore the possibility of developing incoherent and coherent (e.g., FELs) radiation sources based on DLA electrons.

Chapter 3

The Effects of Laser Colors and Polarizations on Laser Wakefield and Direct Acceleration

The LWDA needs two requirements: (i) the initial energy $\epsilon_{\perp}(t = 0)$ of Betatron motion of an injected plasma electron must be sufficiently high to overcome its rapid reduction due to electron acceleration by the longitudinal field of the plasma bubble, (ii) considerable overlap between the laser field and the injected electrons [27, 28]. The second requirement is met by time-delaying the second (DLA) laser pulse from the bubble-forming (pump) laser pulse [27, 28]. Even more significantly, once we allow the possibility of complex laser pulse formats, new opportunities for high-gradient LWDA open up. For example, one can envision the scenarios where the leading and the trailing laser pulses have different polarizations and/or different frequencies. Such laser pulse engineering can be designed to circumvent some of the limitations of the two-pulse LWDA as it was originally conceived [27], i.e. both pulses having the same frequency and polarization. These limitations are exacerbated for moderate-power laser pulses (i.e. in the 10 TW range) which is also widely used [46, 48, 54, 88, 89] because the relatively small size of the plasma bubble can result in undesirable interference between the two equal-frequency laser pulses. Such interference has two consequences. First, the shape of the plasma bubble can be considerably modified by the beat wave between the two pulses. As will be shown below, such modification can have a major effect on the total electron charge trapped inside the plasma bubble and subsequently accelerated by the combination of the LWFA and DLA mechanisms. Second, the peak laser field experienced by the injected electrons is also strongly modified by interference. This

would naturally influence the electrons' energy gain from the DLA mechanism, as well as the fraction of the injected electrons that experiences the DLA. The latter point will also be elaborated on below.

The orthogonal polarization LWDA is promising to benefit both pitfalls and the two-color LWDA is able to work even better. The effectiveness of the combination of the low and high frequency pulse has been demonstrated in ionization injection [75, 76, 90]. The low frequency laser pulse with high ponderomotive force F_p but low electric field E_L blows out the plasma bubble and the high frequency laser pulse with the opposite feature provides the ionization injection without disturbing the plasma bubble because $a^2 \approx I\lambda_L^2$. In the part of this paper, we are exploring the similar combination in the LWDA for the different purposes. The $\lambda_{pump} = 0.8\mu m$ low frequency laser pulse blows out the plasma bubble and produces the ionization of the high Z gas and the $\lambda_{DLA} = 0.4\mu m$ second time-delayed high frequency laser pulse serves as the DLA pulse. The $\lambda_{DLA} = 0.4\mu m$ DLA pulse can potentially increase the energy gain without disturbing the plasma bubble. In other words, the DLA electron beam energy and the charge yield can be enhanced. We also demonstrate the improved stability of the LWDA by using $\lambda_{DLA} = 0.4\mu m$ DLA pulse.

The results of self-consistent 2D PIC simulations carried out using the VLPL code are presented in the remainder of the chapter. Three scenarios are presented: single color parallel polarization LWDA, single color orthogonal polarization LWDA and two color parallel polarization LWDA. The schematic of a proposed LWDA is shown in Fig. 3.1 (see caption for simulations parameters). We consider the scheme that is composed of the short length injection stage and acceleration stage. This two-stage scheme has been experimentally verified [71, 91] and the sub-hundred micrometer gas nozzle has also

been achieved [92, 93]. Ten-terawatt pump pulse ($P_{pump} = 12TW$) and the time-delayed DLA pulse ($P_{DLA} = 10TW$) are assumed in the simulations. The laser parameters are consistent with the UT^3 laser system [48, 54]. We keep the power and a_0 the same when the $\lambda_{DLA} = \lambda_L/2$ DLA pulse is used. It means that the $\lambda_{DLA} = \lambda_L/2$ DLA pulse is tightly focused. The $100\mu m$-long injection stage is formed by gas mixture of 80% He and 20% N_2 shown as a dark area in the middle of Fig. 3.1(a). The injection is due to the ionization of high-Z nitrogen ions (N^{5+} and N^{6+}) in the simulations. We have demonstrated that the ionization injection is able to produce electrons with large enough $\epsilon_\perp(t = 0)$ for the operation of the LWDA [28]. The background plasma is formed by the leading edge ionization of the neutral gas. The inner shell nitrogen's electrons (N^{5+} -> N^{6+} and N^{6+} -> N^{7+}) are produced via ionization close to the peak of the pump pulse intensity and are injected and get trapped inside the plasma bubble [70, 78, 80]. The ionizations also happen for the DLA pulses but due to the relative position of the DLA pulses, the wake potential difference can not satisfied the trapping condition $\frac{e\Delta\Psi}{m_e c^2} \approx -1$ [28, 70, 75, 76]. Therefore, the pump pulse plays the roles of producing the plasma bubble and injecting the electrons into it. The ADK tunneling ionization model [68, 77, 81] is used to describe the release of the inner shell electrons from the nitrogen ions. Figs. 3.1(b-e) are the initial on axis $E_\perp^2$ in the three schemes we consider. Figs. 3.1(b-d) are the single color cases. The single color parallel polarization LWDA has larger initial on axis $E_\perp^2$ in the DLA pulse part than single color orthogonal polarization LWDA due to the constructive interference. The two color parallel polarization LWDA has the same a_0 as single color LWDAs so the initial on axis $E_\perp^2$ is much higher that is clear by looking at Fig. 3.1(e). The optimal time delay of the second DLA pulses are $\Delta\tau = 24fs$ for the single color parallel polarization LWDA and the two color parallel LWDA and $\Delta\tau =$

$21fs$ for the single color orthogonal polarization LWDA regarding the peak DLA electron energy.

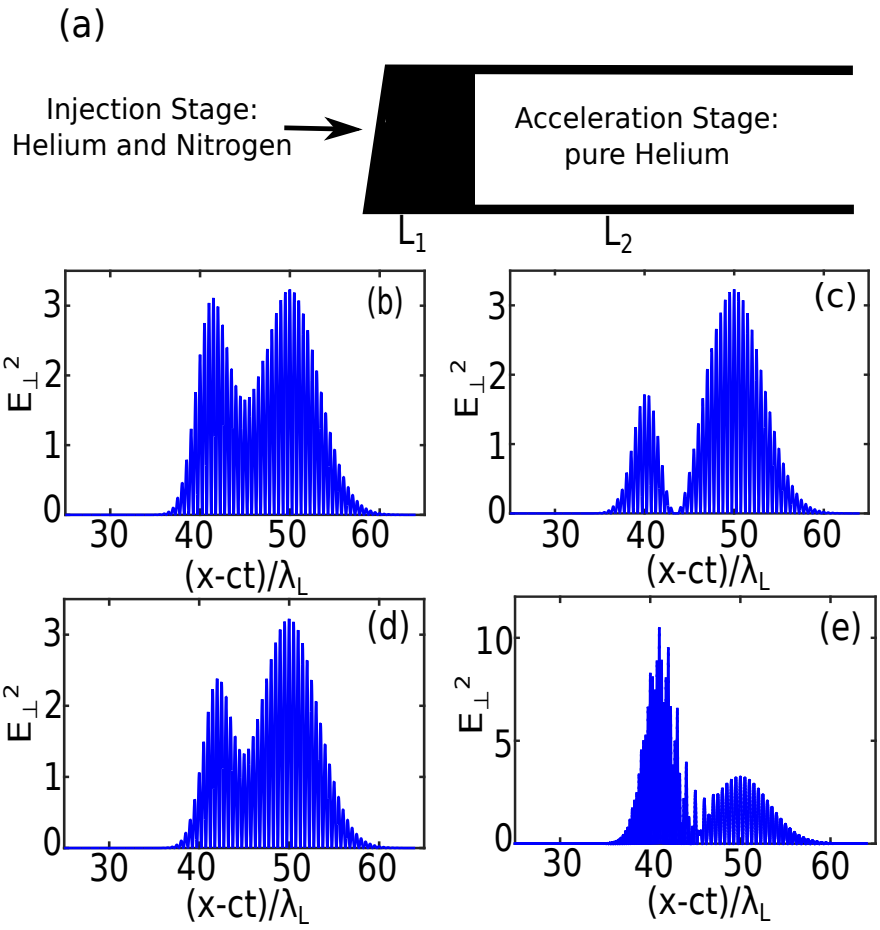

FIGURE 3.1

FIGURE 3.1: (a) plasma density profile. It is divided into the injection stage and acceleration stage. (b) Initial on axis $E_{\perp}^2$ for the single color parallel polarization case $\lambda_{pump} = \lambda_{DLA} = \lambda_L$ and time delay $\Delta\tau = 24fs$. (c) Initial on axis $E_{\perp}^2$ for the single color parallel polarization case $\lambda_{pump} = \lambda_{DLA} = \lambda_L$ and time delay $\Delta\tau = 25.3fs$, the destructive interference appears. (d) Initial on axis $E_{\perp}^2$ for the single color orthogonal polarization case $\lambda_{pump} = \lambda_{DLA} = \lambda_L$ and time delay $\Delta\tau = 21fs$. (e) Initial on axis $E_{\perp}^2$ for the two color parallel polarization case $\lambda_{pump} = 2\lambda_{DLA} = \lambda_L$ time delay $\Delta\tau = 24fs$. $E_{\perp}$ is normalized to $m_e c\omega_L/e$. Plasma parameters: mixed gas length $L_1 = 100\mu m$, $L_2 = 1mm$; $n_0 = 1.5\times10^{19}cm^{-3}$, $n_{N^{5+}} = 0.2n_0$, ionization potential for $N^{5+} \rightarrow N^{6+}$ $U_{ion} \approx 552.1ev$and $N^{6+} \rightarrow N^{7+}$ $U_{ion} \approx 667.0ev$, $\lambda_p = \frac{2\pi c}{\omega_p} = 9\mu m$. Laser parameters: wavelength $\lambda_{pump} = \lambda_L$, $I_{pump} = 7.0\times10^{18}W/cm^2$, $I_{DLA} = 4.8\times10^{18}W/cm^2$ for $\lambda_{DLA} = \lambda_L$ and $I_{DLA} = 1.9\times10^{19}W/cm^2$ for $\lambda_{DLA} = 0.5\lambda_L$, pulse durations $\tau_{pump} = 20fs$ and $\tau_{DLA} = 10fs$, $w_{pump} = 10\mu m$, $w_{DLA} = 10.6\mu m$ for $\lambda_{pump} = \lambda_L$ DLA pulse and $w_{DLA} = 5.3\mu m$ for $\lambda_{DLA} = 0.5\lambda_L$, inter-pulse time delay is changing $\Delta\tau = 21.3 - 26.7fs$. Simulation parameters: numerical grid cell size $\Delta x\times\Delta z = \lambda_L/50\times\lambda_p/50$ for $\lambda_{DLA} = \lambda_L$ DLA pulse and $\Delta x\times\Delta z = \lambda_L/100\times\lambda_p/50$ for $\lambda_{DLA} = 0.5\lambda_L$ DLA pulse. $\lambda_L = 0.8\mu m$

3.1 Laser Polarization Effects on the Laser Wakefield and Direct Acceleration

3.1.1 Single Color Parallel Polarization Laser Pulse (SP-LWDA)

We first look into the details of the SP-LWDA. As shown in Fig. 3.2(a), the plasma bubble has not formed during the injection stage. The trapping of electrons happens in the nonlinear wake stage. With the self-focusing of the pump pulse, the plasma bubble is formed at about $x = 200\mu m$. Fig. 3.2(b) shows the bubble structure at the end of the propagation. There are electrons that are accelerated inside of the plasma bubble but they are not dense. The zoom-in color-coded electron spatial distribution is shown in Fig. 3.2(d). The DLA electrons advance slower than the non-DLA electrons. Detail discussions are in [27, 28]. The spectrum is in Fig. 3.2(c). Two peaks are formed. The DLA electrons peaks at about $\gamma_{DLA} m_e c^2 \approx 170\ MeV$ and gain about 60 MeV more energy than non-DLA electrons. The vertical axis in Fig. 3.2(c) is the number of macro-electrons. It is for the later comparison with the other two cases. We observe all the features of LWDA as mentioned in [27, 28] but in this moderate power regime.

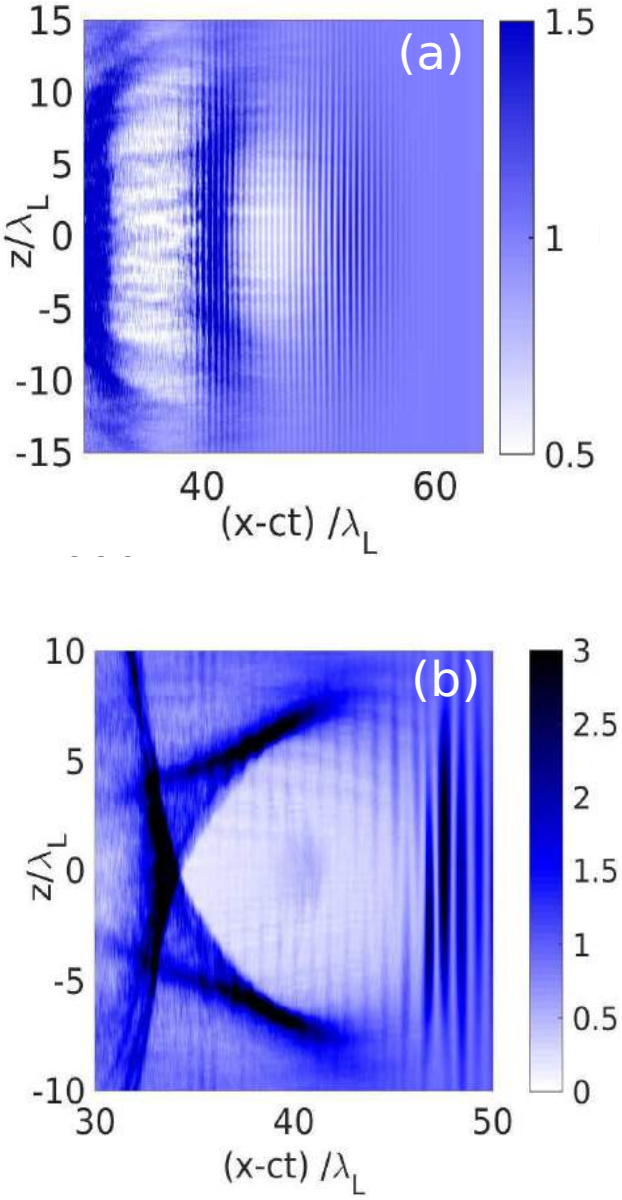
(a)
15
10
5
0
-5
-10
-15
z/λL
40
60
(x-ct) /λL
1.5
1
0.5
(b)
10
5
0
-5
-10
z/λL
30
40
50
(x-ct) /λL
3
2.5
2
1.5
1
0.5
0

FIGURE 3.2

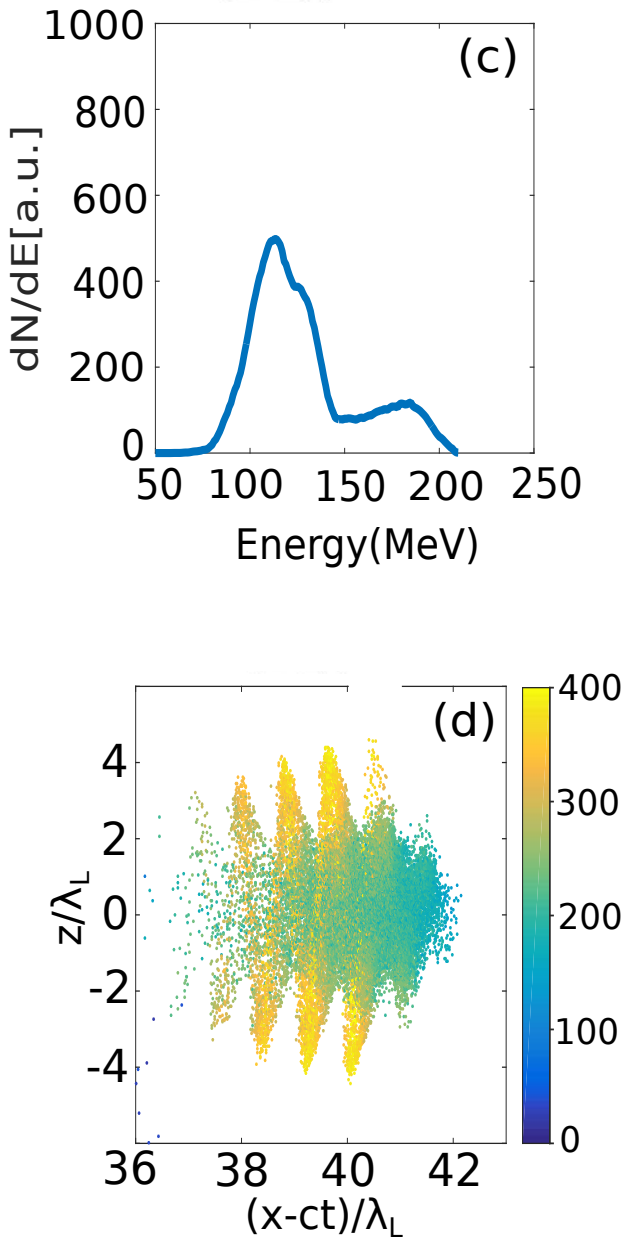

FIGURE 3.2: (a) Nonlinear wake structure at the propagation distance $x = 128\mu m$ for the SP-LWDA. (b) The bubble structure at $x = 640\mu m$ for the SP-LWDA. The density is normalized to the initial density in both (a) and (b). (c) the energy spectrum for electrons in (d). (d) Spatial distribution of the trapped electrons and color-coded by their γ at $x = 640\mu m$ for the SP-LWDA

The time-delay of the second DLA pulse is one of the crucial parameters. This parameter is from the synchronization of the pump pulse and the DLA pulse. In the moderate laser power regime (e.g. UT[3] laser system), the plasma bubble is smaller $R \approx \sqrt{a_0}/k_p$ [94] than the cases in [27, 28] and the interference between the pump pulse and the DLA pulse has to be taken into account. The SP-LWDA is the most common setup but it relies on the extremely accurate timing of the time-delay $\Delta\tau$. To understand how the time-delayed of the DLA pulse affect the LWDA, we need to consider different cases that the time delay of the DLA pulse is slightly shifted from the position in Figs. 3.2. Figs. 3.3 shows several cases with both forward shifted $\delta\tau = 0.25\lambda_L, 0.5\lambda_L$ and the backward shifted $\delta\tau = -0.25\lambda_L, -0.5\lambda_L$ in the SP-LWDA.

We have already seen the on axis $E_\perp^2$ for the case $\delta\tau = -0.5\lambda_L, 0\lambda_L$ in Fig. 3.1(b, c). Fig. 3.1(b) is the constructive interference and the destructive interference appears by only shifting the DLA pulse $0.5\lambda_L$backward as shown in Fig. 3.1(c). The $E_\perp^2$ at the bottom of the bubble are changed significantly. These cases are only slight shifts but the SP-LWDAs produce the drastically different results. Since the number of the DLA electrons may become very small, we roughly separate the energy spectrum to the DLA spectrum and the non-DLA spectrum by the empirical criteria that the electrons gain $A_L \geq 75\, MeV$ directly from the laser field E_L belong to the DLA group. The DLA and non-DLA spectra for all five cases are shown in Fig. 3.1(a) and Fig. 3.1(b) respectively. The magenta curves in Fig. 3.3(a, b) are the DLA spectrum and the non-DLA spectrum for $\delta\tau = 0\lambda_L$, corresponding to $\Delta\tau = 24fs$. From the point of view of the DLA energy gain, it is clear that $\Delta\tau = 24fs$ is the optimal case. The peak energy of the DLA spectra changes from about $\gamma^{DLA} m_e c^2 \approx 120\, MeV$ to $\gamma^{DLA} m_e c^2 \approx 170\, MeV$. The number of the accelerated macro-electrons has about 6 times different

from the best case (the magenta curve) to the worst case (the blue curve). Only slightly shifts of the $\lambda_{DLA} = \lambda_L$ DLA pulse deteriorate the final results. We observe that the number of DLA electrons increase in the constructive interference although the total number of the trapped electrons drop. The ratio of DLA electrons increases with the DLA pulse peak electric field and the constructive interference broadens the high laser electric field region.

Note that the non-DLA spectra in Fig. 3.3(b) also exhibit the differences in the peak energy and the number of the accelerated macro-electrons. The differences in the number of the accelerated macro-electrons are due to the perturbation of the laser wake induced by the $\lambda_{DLA} = \lambda_L$ DLA pulses in the injection stage. The differences in the peak energy are from the beam loading effect [27, 95, 96] which influences the plasma bubble accelerating field. We have to mention that the differences in the DLA spectra are influenced by both the energy gain from laser and the energy gain from wake. It is convincing that the time delay of the $\lambda_{DLA} = \lambda_L$ DLA pulse has to be carefully selected and the SP-LWDA is not very stable in the moderate laser power regime. Therefore, we have to turn to the other directions to avoid the time jittering of LWDA.

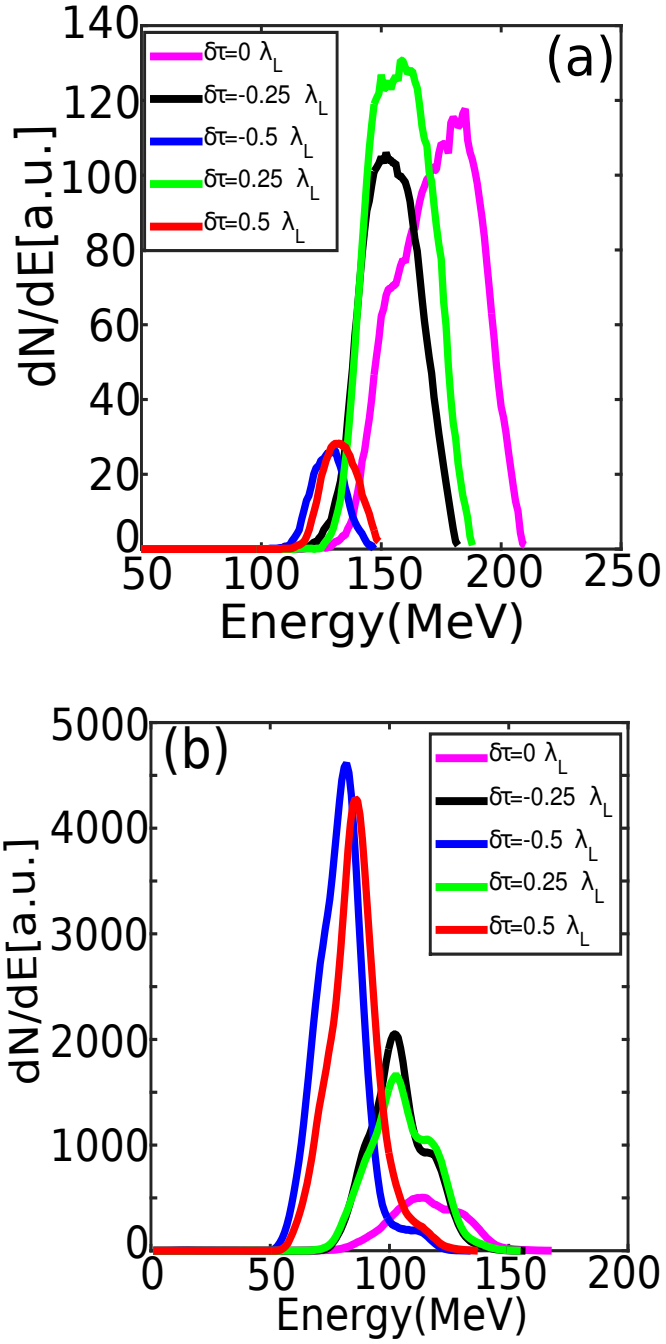

FIGURE 3.3: (a) The spectra for the DLA electrons $A_L \geq 75\ MeV$ in different cases. (b) The spectra for the non-DLA electrons $A_L < 75\ MeV$ in different cases

3.1.2 Single Color Orthogonal Polarization Laser Pulse (SO-LWDA)

The interference between the pump pulse and the DLA pulse is the main resource of the time jittering of SP-LWDA. The natural way to avoid this time jittering is to rotate the pump pulse so that the DLA pulse and the pump pulse are orthogonal to each other. We investigate this situation by making the pump pulse polarize in the Y direction. Other laser and plasma parameters are exactly the same as shown in the SP-LWDA.

As shown in Fig. 3.4(a), the plasma bubble structure does not have observable difference compared with Fig. 3.2(b). But the numbers of trapped electrons are different between SP-LWDA and SO-LWDA. This leads to the different accelerating field due to the beam loading effect. We have to mention that the optimal time-delays of the DLA pulse have a small difference (see caption of Fig. 3.1) between the SP-LWDA and SO-LWDA because of the evolution of the DLA pulse. The spectra in the optimal cases of the SP-LWDA and the SO-LWDA are in general similar. Non-DLA electrons peaks at about $\gamma^{non-DLA} m_e c^2 \approx 110\, MeV$ and DLA electrons peaks at about $\gamma^{DLA} m_e c^2 \approx 170\, MeV$. The number of the macro-electrons are different. The difference in the trapped electrons is from the perturbation to the nonlinear wake in the injection stage. We will discuss it in detail later. There is also difference in the number of the DLA electrons. The high energy peak in the spectrum of Fig. 3.2(c) is higher than in Fig. 3.4(b) although the total number of the trapped electrons is smaller. The reasons are two-fold: one is that the constructive interference increases the DLA pulse electric field so the electrons experience stronger laser field in the optimal case of the SP-LWDA; the other is that there are more ricochet electrons in parallel polarization LWDA [28].

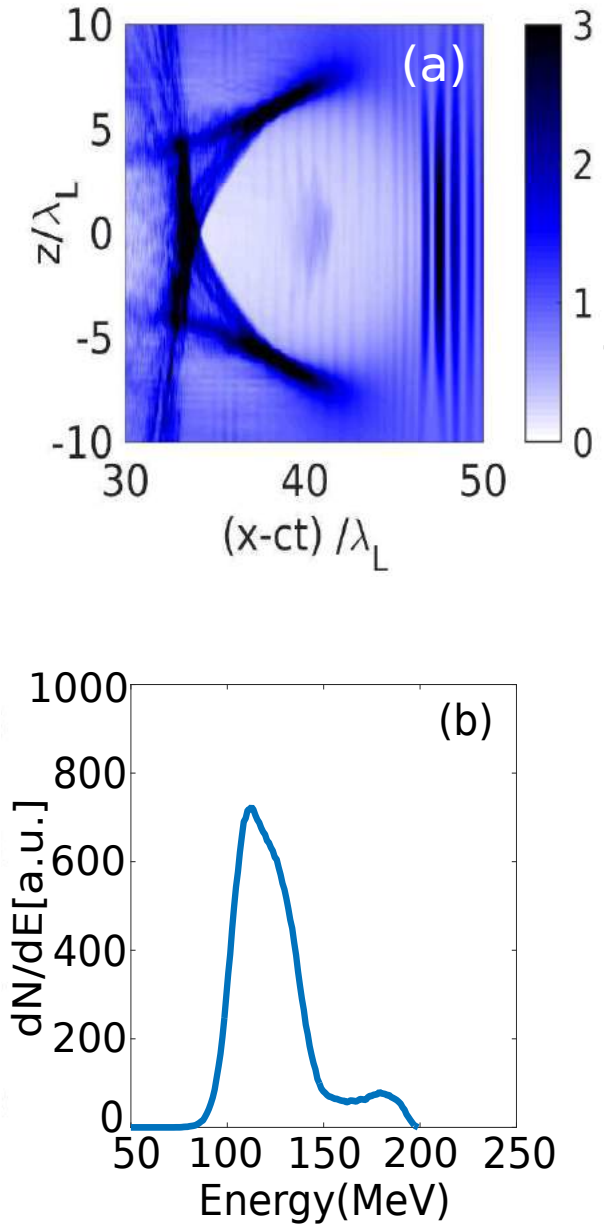

FIGURE 3.4: (a) The bubble structure at $x = 640\mu m$ for the SO-LWDA. The density is normalized to the initial density. (b) the energy spectrum for electrons trapped in the bubble.

The time jittering is improved in the SO-LWDA. The variations in the DLA and the non-DLA spectra are smaller in Figs. 3.5 than in Figs. 3.3. Fig. 3.5(a) are the DLA spectra for the both backward shift case and the forward shift case. The variations in the peak energy and the number of electrons are better but there are still some fluctuations. Since there is no interference between the pump pulse and the DLA pulse, the overlap between the DLA pulse and the trapped electrons plays the major role in the spectra fluctuations. For non-DLA spectra as shown in Fig. 3.5(b), the fluctuations in the spectra are from the perturbations to the nonlinear wake in the injection stage as mentioned above. We have seen that the time-jittering of the final spectra are getting better by rotating the pump pulse to orthogonal direction with respect to the DLA pulse.

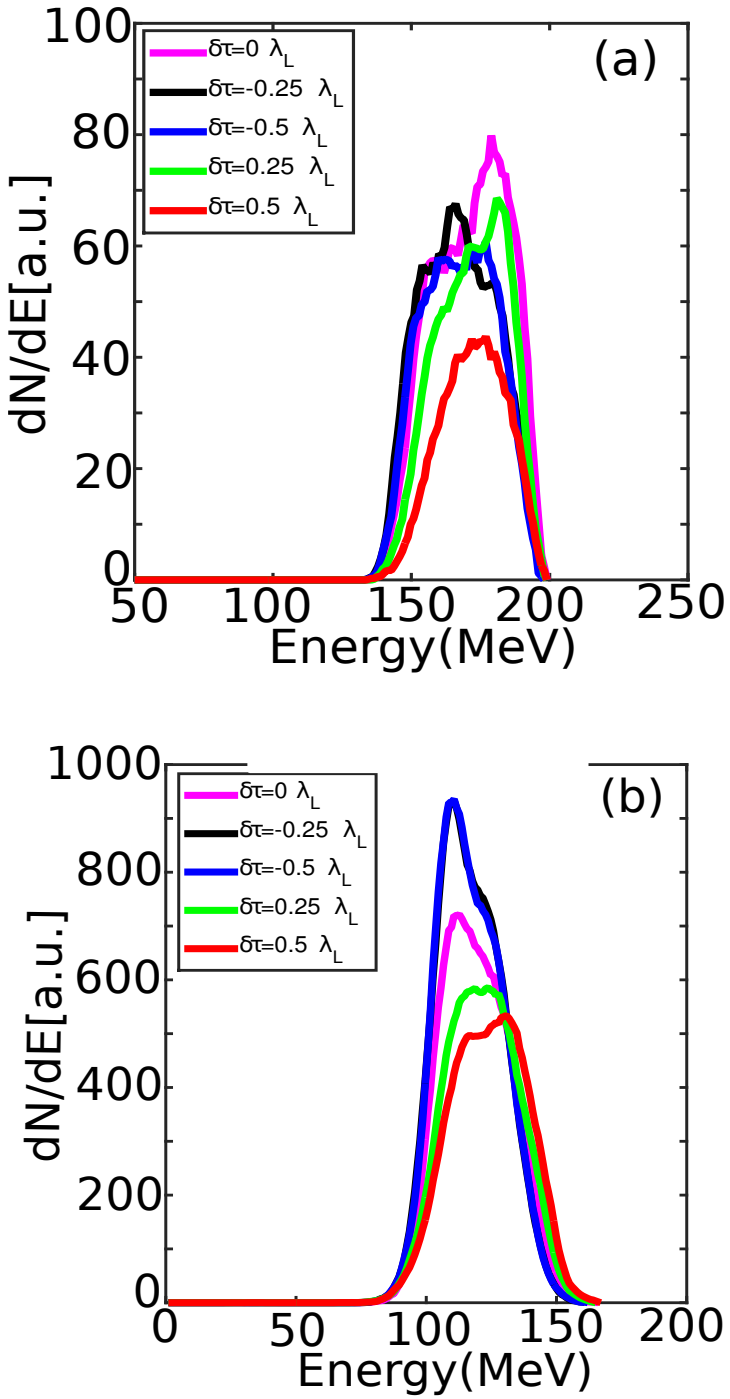

FIGURE 3.5: (a) The spectra for the DLA electrons $A_L \geq 75\ MeV$ in different cases. (b) The spectra for the non-DLA electrons $A_L < 75\ MeV$ in different cases

3.2 Laser Color Effects on the Laser Wakefield and Direct Acceleration

3.2.1 Two Color Parallel Polarization (TP-LWDA)

By rotating the polarization direction of the pump pulse, we improve the performance of the LWDA. It is possible that the performance can be further improved by introducing the $\lambda_{DLA} = 0.5\lambda_L$ DLA pulse. The wake structure is mainly determined by the a_0. We keep the initial a_0 of the DLA pulse the same as in SP-LWDA and SO-LWDA. Since $a_0 \sim \sqrt{I}\lambda_L$, the laser electric field can be higher without changing the wake structure. The energy gain from the laser is $A_L \sim -e\int E_L v_\perp dt$. So the electrons are able to gain higher energy from the laser in TP-LWDA. The other interesting point of the TP-LWDA is that the interference between the pump pulse and the DLA pulse does not have strong influence because of the different frequencies.

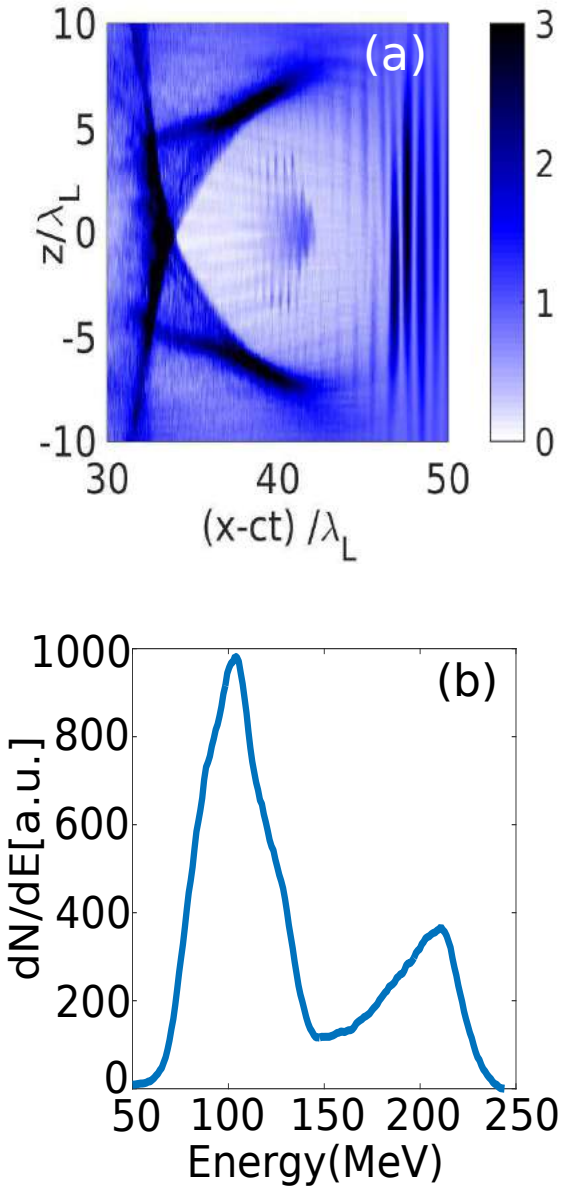

FIGURE 3.6: (a) The bubble structure at $x = 640\mu m$ for the TP-LWDA. The density is normalized to the initial density. (b) the energy spectrum for electrons trapped in the bubble.

The bubble structure is shown in Fig. 3.6(a). It looks similar with Fig. 3.2(b) and in Fig. 3.4(a). The DLA pulses do not influence the plasma bubble but they do have

effects on the evolution of the nonlinear wake in the injection stage. The trapped electrons are denser in Fig. 3.6(a). Without the perturbation to the non-linear wake from the constructive interference, there are more electrons that are trapped. Note that the trapped electrons are smaller in in SO-LWDA than TP-LWDA although both of them do not have constructive interference. The reason is that the optimal position of the DLA pulse is shifted in SO-LWDA and it has the effects on the nonlinear wake evolution. To get a clear picture of the trapping dynamics in the injection stage, we look into the on axis wake potential Ψ as shown in Figs. 3.7. Due to the pump pulse and the DLA pulse, more than 95% of the ionization happens in the gray colored region as shown in Figs. 3.7. The trapping condition is $e\Delta\Psi m_e c^2 \approx -1$ [28, 70, 97]. In Fig. 3.7(a), the TP-LWDA (red curve) is the highest and close to $e\Psi m_e c^2 \approx 0.2$ at the bottom part of the nonlinear wake. The trapping condition is satisfied for TP-LWDA (red curve) in a widest region. In the contrary, the trapping condition cannot be satisfied for SP-LWDA (blue curve) at propagation distance $x = 64\mu m$. As the nonlinear wake evolved, all three scenarios can satisfy the trapping condition as shown in Fig. 3.7(b). The region for TP-LWDA is still the widest. Therefore, we understand that the charge yield for TP-LWDA is the highest.

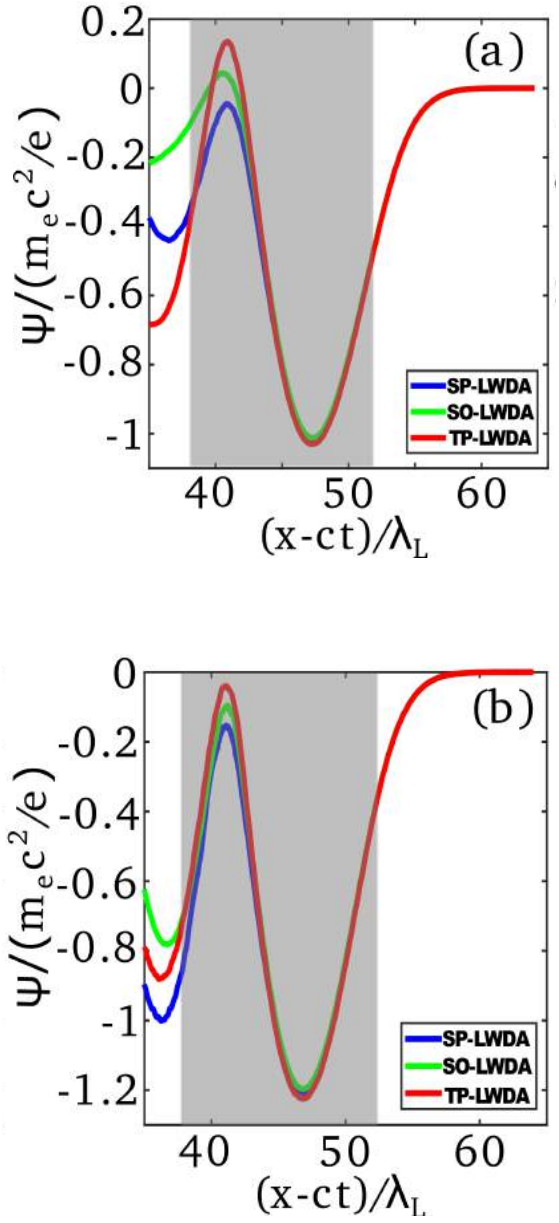

FIGURE 3.7: (a) On axis wake potential Ψ at propagation distance $x = 64\mu m$ for SP-LWDA(blue), SO-LWDA(green) and TP-LWDA(red). (b) On axis wake potential Ψ at propagation distance $x = 128\mu m$ for SP-LWDA(blue), SO-LWDA(green) and TP-LWDA(red). More than 95% of ionization happen in the gray region

Not only the number of the trapped electrons, the energy of the DLA electrons are also higher in TP-LWDA. As shown in Fig. 3.6(b), the DLA peak is at about $\gamma^{DLA} m_e c^2 \approx 210\ MeV$. It almost doubles the energy peak of the non-DLA electrons and is close to 50 MeV higher than SP-LWDA and SO-LWDA without broadening the beam's energy spread. The other interesting effect is the number of the DLA electrons. The number of DLA electrons in optimal TP-LWDA counts for about 35% of the number of the non-DLA electrons while this ratio is about 20% for optimal SP-LWDA and about 12% for optimal SO-LWDA. The increase of the total number of trapped electrons is one reason. The other reason is that the laser intensity is higher in TP-LWDA, which has the connection to the number of the DLA electrons.

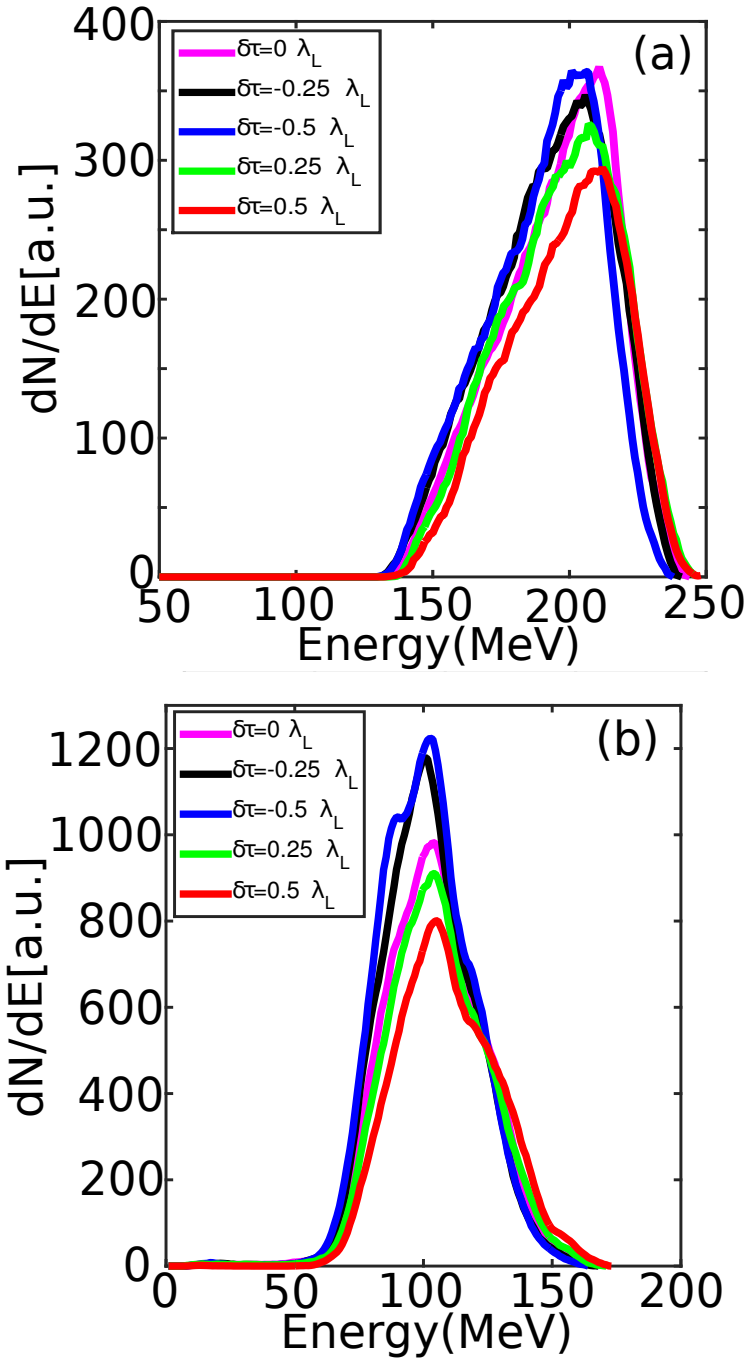

FIGURE 3.8: Electron energy spectra in TP-LWDA. (a) The energy spectra for the DLA electrons $A_L \geq 75MeV$ in both backward shift and forward shift cases. (b) The energy spectra for the non-DLA electrons $A_L \leq 75MeV$ in both backward shift and forward shift cases.

Higher energy gain and higher charge yield are first two-folds advantages. The stability is also important. A few cases with the slightly different time delay of the $\lambda_{DLA} = 0.5\lambda_L$ DLA pulse are considered. It is boring to see the more or less the same plots as in Fig. 3.1(e) for both the backward shift case and the forward shift case. So we directly show the final spectra for the DLA electrons and the non-DLA electrons. The rough separation criteria is still the electrons gain $A_L \geq 75MeV$ directly from the laser field. On the side of the final electron energy, no matter how to shift the $\lambda_{DLA} = 0.5\lambda_L$ DLA pulse, the DLA spectra consistently peak at about $\gamma^{DLA} m_e c^2 = 200MeV \sim 210\, MeV$ as shown in Fig. 3.8(a). On the other side of the number of the accelerated macro-electrons, there are fluctuations but not as drastic as in the single color cases. The worst case is $\delta\tau = 0.5\lambda_L$ forward from the initial time delay $\Delta\tau = 24fs$ as indicated by the red line in Fig. 3.8(a). The number of the DLA electrons is still about two times higher than the optimal case in the SP-LWDA in Fig. 3.3(a) and three times higher than the optimal case in SO-LWDA as shown by the magenta curve in Fig. 3.5(a). The ratio between the number of the DLA electrons to the non-DLA electrons are between 20% to 35% for all the cases. This is significantly better than the most of cases in the SP-LWDA and in the SO-LWDA in which the ratios drastically change from 20% to about 1%. We find that the non-DLA spectra in the forward shift cases and the backward shift cases are also slightly different in the number of the trapped electrons and the peak energy. The explanation for this phenomenon is similar with the SO-LWDA. It is due to the perturbation of the laser wake induced by the position variation of the $\lambda_{DLA} = 0.5\lambda_L$ DLA pulse. From the investigation of the TP-LWDA, the high frequency DLA pulse is optimistic to the stable operation of the LWDA.

3.2.2 Radiation Generation of Electrons

The DLA electrons are able to produce more copious X-rays than the non-DLA electrons. We select two representative electrons from the simulation of TP-LWDA. The DLA electron has larger p_z and γ than non-DLA electron as shown in Fig. 3.9(b) and Fig. 3.9(c). The X-ray spectra are calculated by integrating over the electrons' trajectories based on the synchrotron radiation formula in [35]. As shown in Fig. 3.9(a), the DLA electron has much higher and wider X-ray spectrum than the non-DLA electron. The DLA electron has $\gamma_{max} \approx 450 m_e c^2$ and $p_z \approx 35 m_e c$ and the non-DLA electron has $\gamma_{max} \approx 250 m_e c^2$ and $p_z \approx 8 m_e c$. We can estimate the maximum X-ray critical frequency $\omega_c = 1.5\gamma^3 c/\rho$ [35] for the DLA electron is $\omega_c^{DLA} \approx 45 KeV$ and for the non-DLA electron is $\omega_c^{nDLA} \approx 5 KeV$. The DLA and non-DLA X-ray spectra roughly peak at about $\omega_{peak}^{DLA} \approx 7 KeV$ and $\omega_{peak}^{nDLA} \approx 0.6 KeV$ respectively. Therefore, the DLA electrons could be the excellent radiation source.

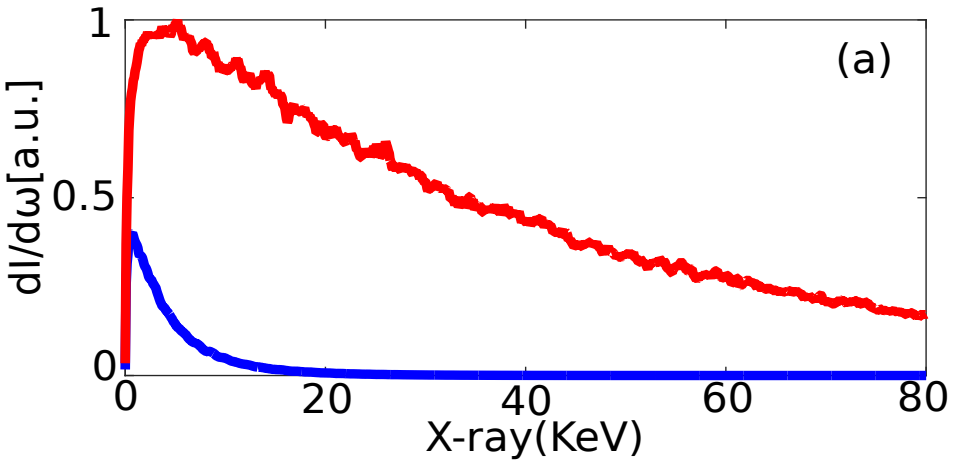

FIGURE 3.9

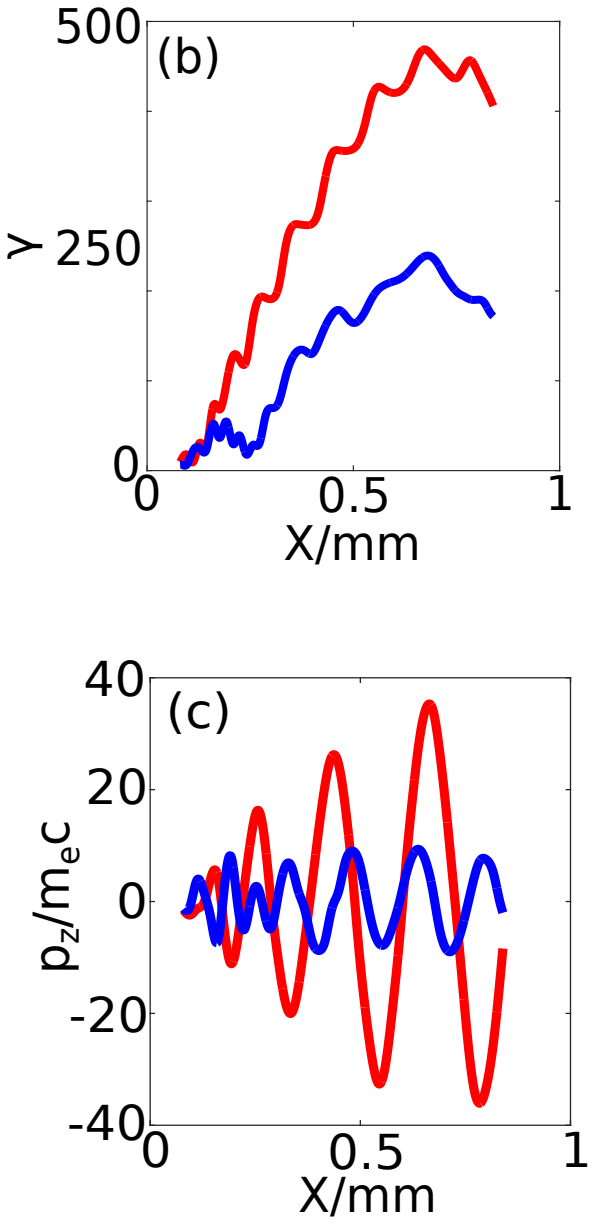

FIGURE 3.9: (a) X-ray spectra for the representative DLA electron (red) and non-DLA electron (blue) in TP-LWDA. (b) the evolution of γ for the representative DLA electron (red) and non-DLA electron (blue). (c) the transverse momentum p_z for the representative DLA electron (red) and non-DLA electron (blue).

3.3 Summary

In conclusion, we have investigated the three possible scenarios of laser wakefield and direct acceleration (LWDA) in a moderate power regime: SP-LWDA, SO-LWDA and TP-LWDA. SP-LWDA has huge time-jittering in the final electron spectrum because of the interference between the pump pulse and the DLA pulse. SO-LWDA has relatively better performance than the SP-LWDA since it eliminates the interference and improves the time jittering. But the DLA charge yield is not improved. TP-LWDA combines the benefits of the $\lambda_{pump} = \lambda_L$ pump pulse and the $\lambda_{DLA} = 0.5\lambda_L$ DLA pulse. It is demonstrated that TP-LWDA achieves higher energy and higher charge DLA electrons compared with the SP-LWDA and SO-LWDA. Furthermore, the TP-LWDA increases the stability by lowering the requirement of synchronization between the pump pulse and the DLA pulse. With the introduction of the frequency upshift DLA pulse, the hybrid laser wakefield and direct laser plasma accelerator may become even more valuable for future experiment realization.

Chapter 4

Basic Characters of Laser Wakefield and Direct Acceleration

4.1 Effects of the Laser Phase Velocity[1]

For an electromagnetic wave, two kinds of velocity are very important: group velocity and phase velocity. The group velocity $v_g = \partial\omega/\partial k$ is related to the envelope of the wave and represents the propagation of the wave energy. The phase velocity $v_p = \omega/k$ is related to the phase of the wave and represents the changing rate of the wave phase. In the LWDA system, the electron interacts with the electromagnetic wave in the fast time-scale compared with the pulse duration. The phase velocity v_p plays an very important role. The phase velocity v_p can be derived from the dispersion relation of the wave matter interaction. For the electromagnetic wave propagating in the under-dense plasma, the phase velocity v_p under the linear approximation has the expression

$$v_p = c\sqrt{1+\frac{\omega_p^2}{\omega_L^2}}, \tag{4.1}$$

Eq. (4.1) states that the phase velocity of the electromagnetic wave in the under-dense plasma is larger than the speed of light c. It is also the more realistic situation. This is the reason that we take the phase velocity of the laser wave v_p larger than the speed of light c in our single particle model in chapter 2.

However, the direct energy transfer from the electromagnetic wave to the electron should not be restricted in system with the wave phase velocity $v_p \geq c$. Some other systems such as cluster plasmas [98], residual non-neutral gas [99], or corrugated

[1] X. Zhang, V. N. Khudik, G. Shvets, Physical Review Letters 114 (18), 184801, 2015. Contribution: studied the DLA in the plasma bubble regime; carried out the single particle simulations, PIC simulations and analyzed the results; wrote the paper draft.

plasma waveguides [100] are able to reach the condition $v_p < c$. The subluminal laser wave leads to the significantly different case in the Betatron resonance. The resonance condition may become $\omega_\beta = -< \omega_d >$ where $\omega_d = (1 - \frac{v_x}{v_p})$. The Doppler shifted laser frequency ω_d can be smaller than zero $\omega_d < 0$ for ultra-relativistic electrons.

We explore the subluminal laser wave interaction with the electron under the same single particle model as Eqs. (2.3, 2.4). We first consider the case of a subluminal laser pulse with $v_p = 0.9985c$ [101] and briefly analyze the subluminal case below because it provides a stark illustration of the delayed dephasing via direct laser-electron interaction. Test electrons are injected at $t = 0$ near the back of the bubble at $x = 2.65\lambda_L$ with a constant value of $\gamma = 25$. The initial transverse positions z and momenta p_z were chosen to span a wide range $0 < \frac{\epsilon_\perp}{m_e c^2} < 1$ of transverse energies [26, 102] $\epsilon_\perp = \frac{p_z^2}{2\gamma m_e} + \frac{\gamma m_e \omega_\beta^2 z^2}{2}$.

The bifurcated $(\gamma, \epsilon_\perp/m_e c^2)$ phase space of the injected test electrons after the propagation distance of $x = ct = 1.3cm$ is shown in Fig. 4.1(a): one group of electrons (blue) gains considerable transverse energy $\epsilon_\perp$ from the laser while the other group (red) experiences considerable reduction in $\epsilon_\perp$. By following two representative electrons (one from each group, see inset), the following properties of the two groups are observed.

First, Direct Laser Deceleration (DLD): the work $A_L = -\int e\, E_z^L v_z dt$ done by the laser field on the first group of electrons (blue lines in Figs. 4.1) is negative as shown by the dashed line in Fig. 4.1(c). The non-DLD electrons do not exchange energy with the laser pulse. The physics of the DLD is related to the anomalous Doppler effect (i.e. $-\omega_d = \omega_\beta$) that has been investigated in dielectric-loaded or

periodically loaded waveguides [103, 104]. Qualitatively, if an ultra-relativistic ($\gamma \approx p_x/m_e c \gg 1$) electron interacts with the laser alone, a simple relationship between the changes in $\epsilon_\perp$ and γ can be derived: $\Delta\gamma\left(1-\frac{c}{v_{ph}}\right) = \Delta\epsilon_\perp/m_e c^2$, thus implying that DLD ($\Delta\gamma < 0$) is necessary for the resonant excitation of betatron oscillations ($\Delta\epsilon_\perp > 0$) whenever $v_{ph} < c$. The above relation holds under the near-relativistic assumption for the laser pulse: $\left|1 - v_{ph}/c\right| \ll 1$.

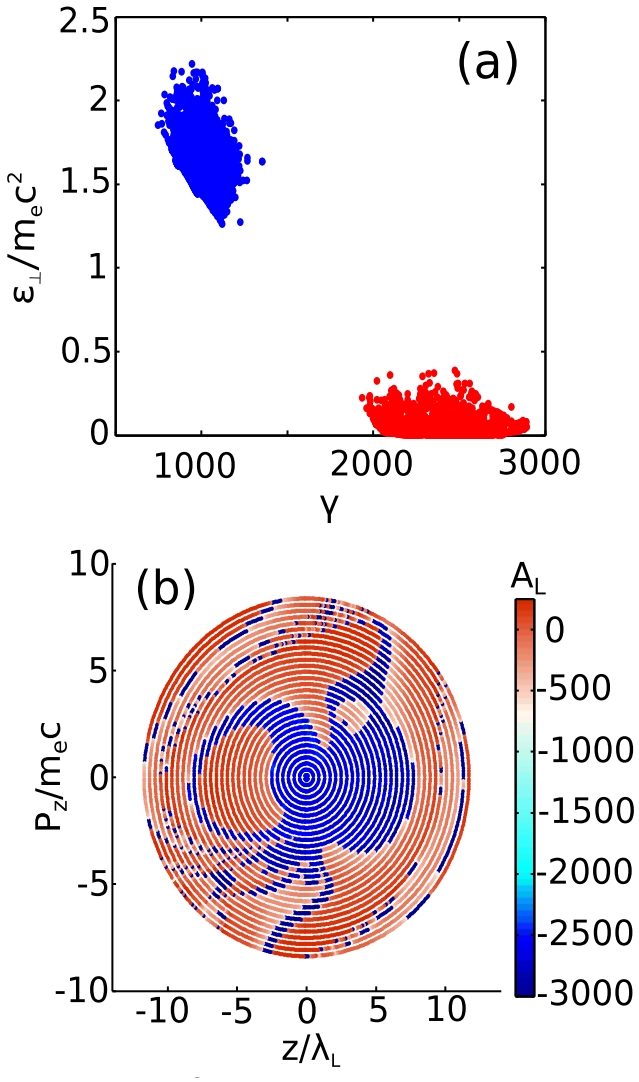

FIGURE 4.1

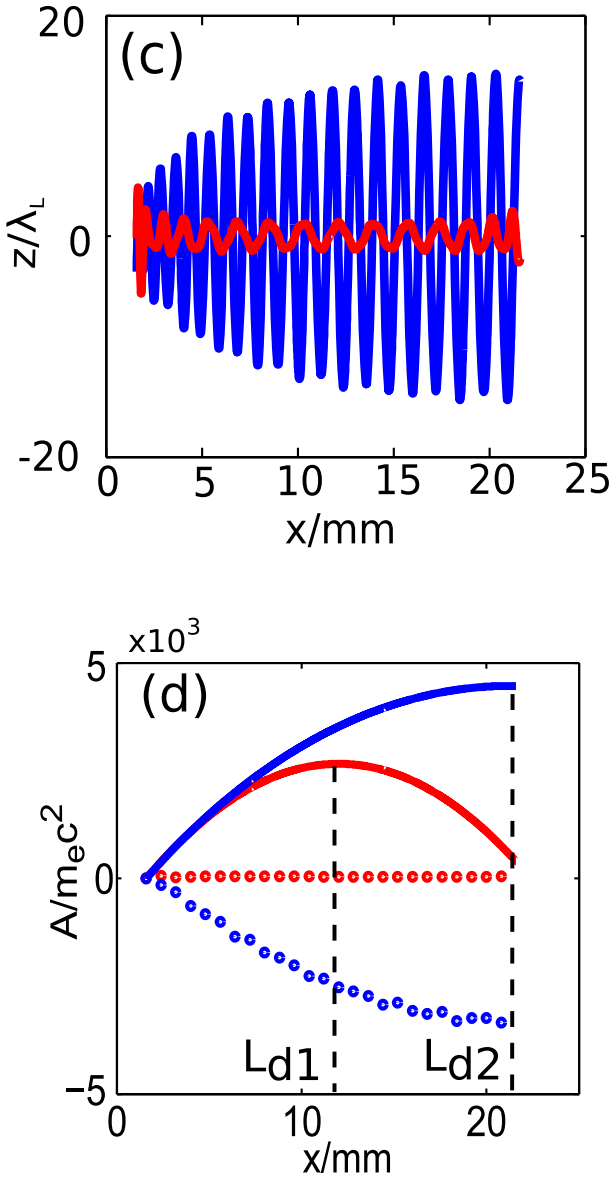

FIGURE 4.1: Single-particle dynamics in combined wake/laser fields with $v_{ph} < c$. (a) Fragmentation of the $(\lambda, \epsilon_\perp)$ phase into DLD (blue) and non-DLD (red) electron populations at x=1.3 cm. (b) Color-coded laser energy gain A_L as a function of the initial conditions in the (z_0, p_{z0}) phase space. Elliptical curves: $\epsilon_\perp = const$. (c) Betatron trajectories of two representative electrons from the DLD (blue line) and

non-DLD (red line) groups. (d) Energy gain by the same representative electrons from the wake (A_w, solid lines) and from the laser (A_L, dashed lines)

Second, Laser-delayed dephasing is apparent from Fig. 4.1(d), where the trajectory of the DLD electron is shown to cross the bubble's center much later than that of the non-DLD electron: $L_{d2} \approx 2L_{d1}$. The dephasing rate $\frac{d\xi}{dt} = v_x - v_b$ is suppressed by the resonant excitation of the Betatron oscillation according to Eq. (2.6). An important manifestation of the delayed dephasing for DLD electrons is that they experience much greater energy gain $A_w = -\int e\, W_x v_x dt$ from the wakefield (solid lines in Fig. 4.1(d)) compared with non-DLD electrons. Note, however, that the total energy gain $A = A_w + A_L$ is smaller for DLD electrons because they amplify the laser pulse at the expense of the energy gained from the wake.

4.2 Effects of the Accelerating Field

The main difference between the LWDA and the conventional DLA in the ion channel is the existence of the longitudinal accelerating field in the LWDA. We discuss the effects of the accelerating field in this section.

The first obvious effect of the accelerating field is that it accelerates electrons to higher energy together with the laser electromagnetic field. As states in the above chapters, the wake accelerating field and the laser electromagnetic field synergistically accelerate electrons. The electrons' final energy can be almost doubled. This is the big advantage of the accelerating field.

The second effect of the accelerating field is that it restricts the electrons initial condition of entering into LWDA. The electrons must have large enough transverse energy $\varepsilon_{0\perp} = \frac{p_{z0}^2}{2\gamma_0 m_e} + m_e \omega_p^2 z_0^2/4$ to undergo the Betatron resonance as mentioned by Eqs. (2.5, 2.6). This effect of the accelerating field also limits the electron

injection methods. However, there are more electrons that can be satisfied the Betatron resonance condition. The reason is that the rapid acceleration by the accelerating field is able to lower the Dopper shifted laser frequency ω_d so that the electrons with much large initial transverse energy $\epsilon_{\perp 0}$ are able to satisfy the Betatron resonance condition. To illustrate this effect of the accelerating field, we consider the constant accelerating field and the long interaction time. The simplified model is the same as Eqs. (2.3, 2.4) except $W_x = const$ or $W_x = 0$ in this discussion. Without losing generality, we consider the similar parameters in the moderate power regime as in chapter 3. The parameters are in caption of Fig. 4.2.

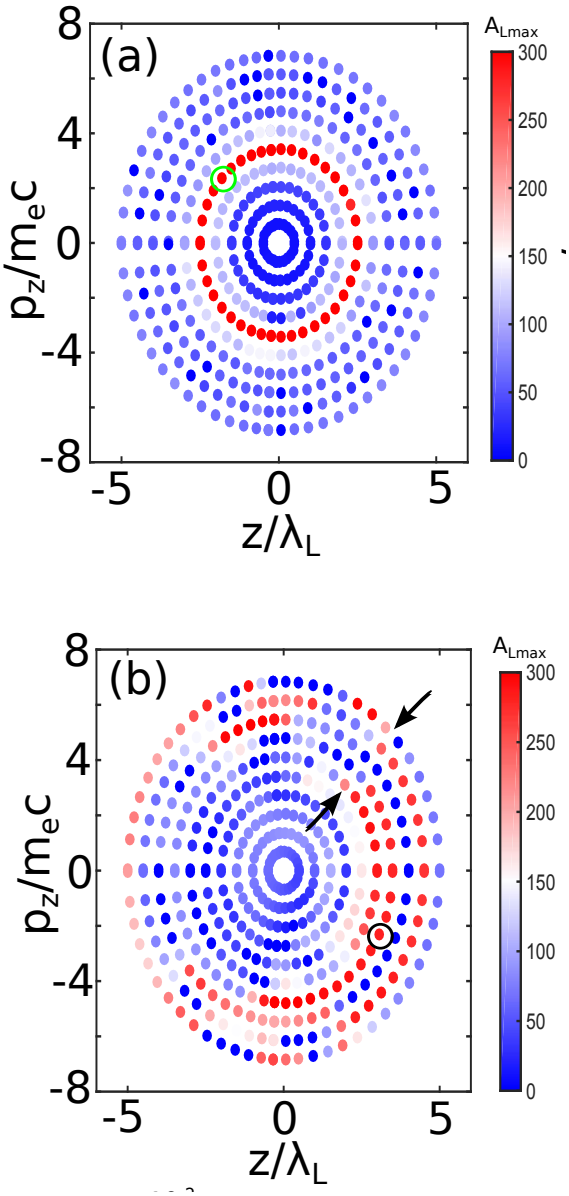

FIGURE 4.2: Single-particle dynamics governed by Eqs. (2.3, 2.4). (a) Color-coded energy gain A_L from the $0.8\mu m$ laser plotted as a function of the initial conditions without longitudinal accelerating field. Rings: $\epsilon_\perp = const$. (b) Color-coded energy gain A_L from the $0.8\mu m$ laser plotted as a function of the initial conditions with longitudinal accelerating field. Rings: $\epsilon_\perp = const$. Simulation parameters: $E_0 \approx 1.5 m_e c\omega_L/e$, $\gamma_{ph} = 14.4$ and $\omega_p/\omega_L = 0.093$, $W_x = -0.08 m_e c\omega_L/e$.

From the comparison of Fig. 4.2(a) and Fig. 4.2(b), we find that the DLA without longitudinal accelerating field happens in a narrower region of $\epsilon_\perp(t=0)$ than the DLA with longitudinal accelerating field. It means that the presence of the longitudinal accelerating field relaxes the requirement of the $\epsilon_\perp(t=0)$. In Fig. 4.2(a), the DLA electrons ($A_L > 200m_ec^2$) are confined in a narrow ring with $\epsilon_\perp(t=0) \approx 0.5m_ec^2$. However, the DLA electrons ($A_L > 200m_ec^2$) occupy a wider band with $0.8m_ec^2 < \epsilon_\perp(t=0) < 2.1m_ec^2$ in Fig. 4.2(b). This is good for generating more DLA electrons. To understand this effect, we take a look at The ultra-relativistic limits of $\langle\omega_d\rangle$ and ω_β (Eqs. (2.5, 2.6)). Due to the absence of the longitudinal accelerating field, the electron γ factor in the case without longitudinal accelerating field can only be changed by the interaction with the laser field. The transverse momentum p_z is strongly correlated with the γ for purely DLA. So the requirement of the initial transverse energy $\epsilon_\perp(t=0)$ is more stringent. On the contrary, the longitudinal accelerating field introduces one more degree of freedom that can increase γ but without raisding p_z. Therefore, the requirement of $\epsilon_\perp(t=0)$ is relaxed and more electrons have the chance to undergo DLA in the case with longitudinal accelerating field.

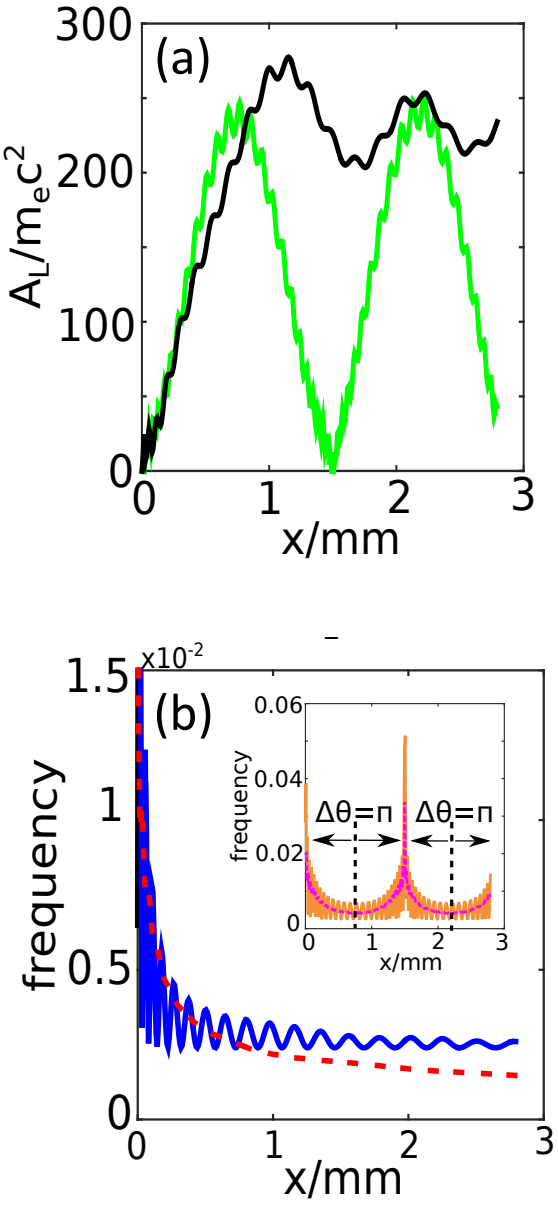

FIGURE 4.3: (a) A_L for two representative electrons with initial conditions marked in Fig. 4.2(a) (green) and Fig. 4.2(b) (black) by circles. (b) Doppler shifted laser frequency ω_d for case I (green) and case II (black); betatron frequency ω_β for case I (magenta) and case II (yellow).

The third effect of the accelerating field is not so intuitive. By looking at the DLA in the ion channel, the electron energy has the wave-like fluctuation as in Fig. 1.2(a). After reaching the peak of the energy, the laser wave start decelerating electrons. For some specific time, the DLA electrons loss all their energy. However, the accelerating field changes this situation. The accelerating field is capable to maintain the energy gain from the laser field A_L. We pick two representative DLA electrons marked by the green circle in Fig. 4.2(a) and the black circle in Fig. 4.2(b). As shown by the green curve in Fig. 4.3(a), the DLA electron in the ion channel case ($W_x = 0$) has the oscillations in A_L. The DLA electron can lose all its energy that was gained from the laser. The phase difference between the gaining stage and the losing stage is $\Delta\theta = \pi$, where $\Delta\theta = \psi + \varphi$, $\frac{d\psi}{dt} = \omega_\beta$ and $\frac{d\varphi}{dt} = \omega_d$. For detail discussion about the DLA in the ion channel, please see [20]. The DLA electron in case with accelerating field ($W_x = const$) keeps the most of the energy gain from the laser field (black line). Whenever the electron is pushed out from the Betatron resonance, it never goes back to the resonance again. This is clear by looking at the frequency matching curves shown in Fig. 4.3(b).

4.3 On the Number of DLA Electrons

One of the basic and important questions is the number of DLA electrons in LWDA. This is related to the DLA electron charge yield of LWDA. We have already raise this issue in the chapter 3. The Two-Color LWDA can significant boost the number of the DLA electrons as shown in Fig. 3.6(b) and Fig. 3.8(a). One important signature of Two-Color LWDA is that it provides larger E_L when other laser plasma

parameters are fixed. In this section, we utilize our simplified model to clarify this problem more systematically.

To make the close connection with the PIC simulations in chapter 3, we turn back to the plasma bubble accelerating field in our simplified model. The ratio between the maximum bubble field and the laser field E_L/W_{xm} is changing. We use our single particle simulations to investigate the relation of the ratio between the number of DLA electrons and the total number of trapped electrons with the E_L/W_{xm}. Electrons are placed near the tail of the bubble and assigned a constant longitudinal momentum $p_x \approx \gamma_b m_e c$. The amplitude of DLA pulse E_0 is changing. As shown in Fig. 4.4, N_{DLA}/N_{total} is increasing with respect to E_L/W_{xm}. Therefore, the large laser field is good to generate more DLA electrons. The issue raised in the chapter 3 is well solved. The high frequency DLA pulse with the same a_0 that has larger E_L is able to increase the number of the DLA electrons and the charge yield.

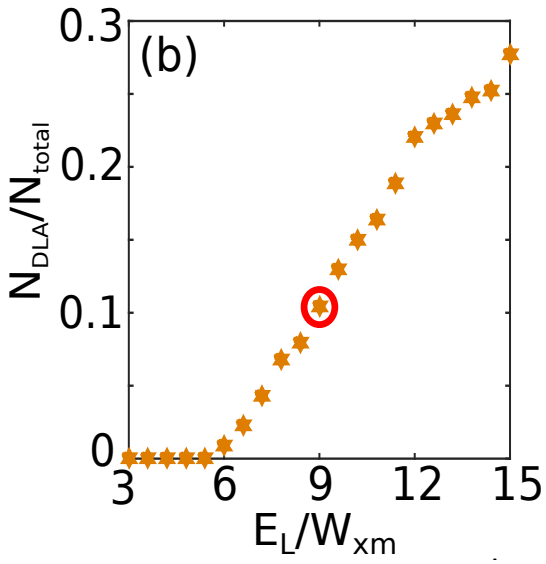

FIGURE 4.4: The ratio between the number of DLA electrons and the number of trapped electrons. Empirical criteria for DLA electrons is $\frac{A_L}{m_e c^2} > 0.3\gamma$. The red circle corresponds to the conditions: $E_0 \approx 1.5 m_e c \omega_L / e$, $\gamma_{ph} = \sqrt{v_{ph}^2 - 1} = 14.4$ and $\omega_p/\omega_L = 0.093$, E_0 is changing in the figure. $W_x = m\omega_p^2(x - r_b - v_b t)/2e$, $\gamma_b = 10$ and $r_b = 6\lambda_L$.

4.4 Emittance of the Electron Beam

Beam emittance is always an important topic in the particle accelerator [1]. In the field of the laser wakefield accelerator, people has paid a lot of attention and put much effort to reduce the emittance of the electron beam [3]. We have to face the issue of the emittance of the electron beam in our LWDA.

Beam emittance is the measure of the area covered by the beam in the position-momentum phase space. When the charged particle beam propagates in the wiggler or the undulator which do not have longitudinal acceleration, the beam emittance is conserved. However, the transverse beam size shrinks when the beam is accelerated. In the laser wakefield accelerator, we have the relation $z \sim \gamma^{-1/4}$ and $p_z \sim \gamma^{1/2}$[11].

The beam emittance ϵ is not conserved with the longitudinal acceleration but the normalized emittance $\epsilon_n = p_x\epsilon$ is a constant. The statistical definition of the normalized emittance has expression

$$\epsilon_n = \langle\frac{p_x}{m_e c}\rangle \sqrt{\langle z^2\rangle \langle\left(\frac{p_z}{p_x}\right)^2\rangle - \langle\left(z\frac{p_z}{p_x}\right)^2\rangle}, \tag{4.2}$$

where $\langle\cdot\rangle$ is the ensemble average. We use Eq. (4.2) and the simplified model to study the emittance of the electron beam.

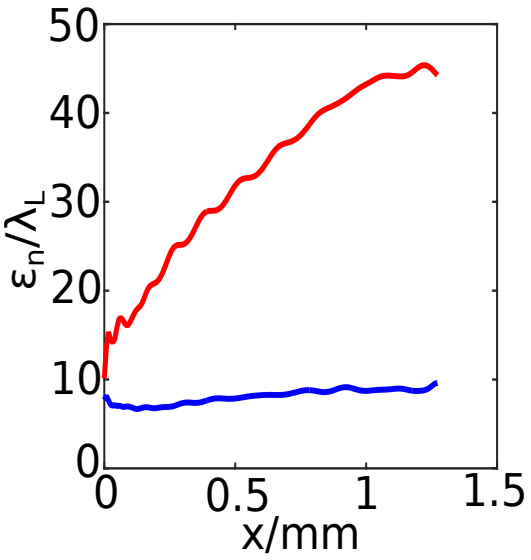

FIGURE 4.5: Evolution of the normalized emittance ϵ_n for both DLA electrons (red line) and non-DLA electrons (blue line) for the case marked by the red circle in Fig. 4.4.

In our single particle simulations, the initial emittance is about $\epsilon_n \approx 6mm \cdot mrad$. The emittance for non-DLA electrons does not change a lot during the whole acceleration process but the DLA electrons have about 6 times larger normalized emittance ϵ_n than the initial emittance and continuously grows during the acceleration process as shown in Fig. 4.5. Therefore, LWDA produce the large emittance electron beam. It is a downside for purely accelerator but may be an

advantage for other applications. Usual ionization injection produces electrons with large initial emittance [75]. It is not good for LWFA but LWDA can utilize it.

4.5 Summary

This chapter summarizes some basic and important characters of LWDA. The laser phase velocity v_{ph} has an effect on the LWDA. The DLA of the subluminal laser wave is apparently different from the superluminal laser wave. The longitudinal accelerating field distinguishes the LWDA from the DLA in the ion channel. It increases the electron energy, broadens the electron initial condition and maintains the electron energy gain from the laser field. The number of the DLA electrons in LWDA has strong relation with the ratio between the laser field E_L and the maximum wakefield W_{xm}. It increases with the E_L/W_{xm}. The LWDA generated electron beams have large normalized emittance ϵ_n and the normalized emittance ϵ_n continuously grows during the acceleration process.

Chapter 5

Conclusion and Outlook

5.1 Conclusion

This chapter summarizes the dissertation and makes the outlook of the laser wakefield and direct acceleration of the electrons. This dissertation focuses on the computational laser plasma electron acceleration. It provides the comprehensive computational researches on the hybrid laser wakefield and direct acceleration of electrons in the plasma bubble regime.

Laser plasma electron acceleration is a fruitful and complex area. Computational research and experimental research becomes more and more important nowadays and are pushing each other forward. The computational research plays a very important role on the laser plasma electron acceleration. Among all the simulation techniques, Particle-In-Cell (PIC) simulation is the most commonly used. The major parts of this dissertation are done through the PIC simulations.

The first question is always about the electron injection in all kinds of laser plasma electron acceleration including the LWDA. The prerequisite of choosing the electron injection method is to identify the requirements of the electron initial conditions. We establish the single particle model based on the assumption of the non-evolving plasma bubble and the uniform plane electromagnetic wave. Through the single particle simulations, it is found that electrons must have large enough transverse energy $\epsilon_{\perp}(t=0)$ in order to undergo LWDA. In general, both of the density-based electron injection mechanism and the laser-based electron injection

mechanism can be utilized in LWDA. For the density-based electron injection mechanism, the sub-hundred micro-meter density-bump injection is able to produce electrons with a large initial transverse energy. For the laser-based electron injection mechanism, the ionization induced injection can generate electrons with large initial transverse energy. The in-depth studies of the electron dynamics during the ionization injection unveil several types of the ionization released electrons in the plasma bubble regime. The off-axis ionization released electron and the "ricochet" electron are responsible for the DLA electrons in LWDA. Especially, the "ricochet" electron gains large initial transverse energy $\epsilon_\perp(t=0)$ due to the off peak phase ionization.

Both of the density-bump injection and the ionization injection generate the similar LWDA electron beams. There is another crucial requirement of the LWDA. The injected electrons must overlap with the intensive laser pulse during all the acceleration process. This requirement is fulfilled by introducing a second less intensive time-delayed co-propagating laser pulse. With these setups, we are able to operate the LWDA. The LWDA electron beam has several unique features. First, the LWDA electron beam is spatially separated. The high energy DLA electrons have the large transverse oscillation amplitude z and the large transverse momentum p_z so that they have smaller dephaing rate compared with the non-DLA electrons. The DLA electrons fall behind with the non-DLA electrons in the plasma bubble. Second, the transverse energy $\epsilon_\perp$ of the DLA electrons is strongly correlated with the DLA electrons' relativistic factor γ. The high energy DLA electrons have the large transverse energy $\epsilon_\perp$ and vice versa. Third, the LWDA electron beam exhibits the double-peak energy spectrum that is particular useful for the experimental measurements. The DLA electron gains significantly higher energy than the non-

DLA electron. The DLA peak is almost doubled compared with the non-DLA peak. The electron dynamics in the LWDA is investigated. The DLA electron experiences the synergistic acceleration by the laser field and the plasma bubble accelerating field. The DLA electron gains energy from the laser field through the Betatron resonance. The reduced dephasing rate of the DLA electron leads to the more energy gain from the plasma bubble accelerating field than the non-DLA electron. The synergistic acceleration is the signature of the electron dynamics in the LWDA.

The polarization direction and the color of the DLA laser pulse are studied in the moderate power (10 TW) regime. Due to the restriction of the laser power, the plasma bubble size is smaller than the 100 TW regime. The interference between the pump pulse and the DLA pulse has strong effects on the LWDA. It is found that the final spectra of both the DLA electron and the non-DLA electrons have the huge time-jittering of the energy and the charge yield in the single color parallel polarization LWDA because of the intensity fluctuation in the bottom of the plasma bubble. By rotating the pump to the orthogonal direction with respect to the DLA pulse, the time-jittering is reduced by avoiding the interference between the pump pulse and the DLA pulse. The high frequency DLA pulse upgrades the performance of LWDA further. With the same a_0, it has the higher electric field E_L than the low frequency DLA pulse. The fluctuation of the final spectra, the energy gain and the charge yield are significantly improved in the two color parallel polarization LWDA. Since the DLA electrons in the LWDA have the high energy and the large oscillation amplitude, they have the potential application as an excellent radiation source.

The dissertation discusses some basic characters of the LWDA. The subluminal laser phase velocity has a big effect on the DLA process through the anomalous

Doppler effect. It is called direct laser deceleration. The longitudinal accelerating field in the LWDA benefits the acceleration from three aspects. First, it works together with the DLA and increases the DLA electron energy. Second, it broadens the range of the initial transverse energy $\epsilon_\perp(t=0)$ in which the electrons can undergo DLA. Third, it is able to maintain the electron energy gain from the laser field since the electron would lose all the energy in the ion channel DLA. The number of the DLA electrons in the LWDA is strongly correlated with the ratio between the laser field and the maximum wakefield E_L/W_{xm}. The DLA electrons in the LWDA has a big normalized emittance ϵ_n that is increasing during all the acceleration process.

5.2 Outlook

The concept of the LWDA has been recently experimentally demonstrated [105]. This phenomenon does exist in the nature. The DLA electron beam has a large normalized emittance which possibly prevents it from the application as an advanced accelerator. However, it can serve as an excellent radiation source. The current researches of the LWDA concentrate on the plasma bubble accelerating regime. But the laser field can also accelerate electrons in the plasma bubble decelerating regime [33]. This kind of acceleration has more unique features and is worth investigating more. The electron beam driven plasma wakefield accelerator [106] is limited by the transformer ratio E_+/E_-. With the help from the DLA in the plasma bubble decelerating regime, the plasma wakefield accelerator may achieve high energy and high quality electron beams. Besides the above theoretical and computational

prospective researches, it is promising to boost the performance of the LWDA by introducing high frequency DLA pulse in the future experiments.

Bibliography

[1] E. Wilson, An introduction to particle accelerators (Oxford University Press, 2001).

[2] T. Tajima and J. M. Dawson, Laser electron accelerator, *Phys. Rev. Lett.*, **43**, 267, (1979).

[3] E. Esarey, C. B. Schroder, W. P. Leemans, Physics of laser-driven plasma-based electron accelerators, *Rev. Mod. Phys.*, **81**, 1229, (2009).

[4] J. Faure *et al.,* A laser–plasma accelerator producing monoenergetic electron beams, *Nature (London),* **431**, 541, (2004).

[5] S. Mangles *et al.*, Monoenergetic beams of relativistic electrons from intense laser–plasma interactions, *Nature (London),* **431**, 535, (2004).

[6] C. Geddes *et al.*, High-quality electron beams from a laser wakefield accelerator using plasma-channel guiding, *Nature (London),* **431**, 538, (2004).

[7] W. Leemans *et al.*, GeV electron beams from a centimeter-scale accelerator, *Nature Phys.*, **2**, 696 (2006).

[8] X. Wang *et al.*, Quasi-monoenergetic laser-plasma acceleration of electrons to 2 GeV, *Nature Comms.*, **4**, 1988 (2013).

[9] H. T. Kim *et al.*, Enhancement of electron energy to the multi-GeV regime by a dual-stage laser-wakefield accelerator pumped by petawatt laser pulses, *Phys. Rev. Lett.,* **111**, 165002 (2013).

[10] W. Leemans *et al.*, Multi-GeV electron beams from capillary-discharge-guided subpetawatt laser pulses in the self-trapping regime, *Phys. Rev. Lett.*, **113**, 245002 (2014).

[11] S. Corde, K. Ta Phuoc, G. Lambert, R. Fitour, V. Malka and A. Rousse., Femtosecond x rays from laser-plasma accelerators, *Rev. Mod. Phys.*, **85**, 1, 2013.

[12] S. Cipiccia *et al.,* Gamma-rays from harmonically resonant betatron oscillations in a plasma wake, *Nature Phys.*, **7**, 867 (2011).

[13] A. Pukhov, J. Meyer-Ter-Vehn, Laser wake field acceleration: the highly non-linear broken-wave regime, *Appl. Phys. B*, **74**, 355 (2002).

[14] I. Blumenfeld *et al.*, Energy doubling of 42 GeV electrons in a metre-scale plasma wakefield accelerator, *Nature (London)*, **445**, 741, (2007).

[15] M. Litos *et al.,* High-efficiency acceleration of an electron beam in a plasma wakefield accelerator, *Nature (London)*, **515**, 92, (2014).

[16] A. Caldwell, K. Lotov, A. Pukhov, F. Simon., Proton-driven plasma-wakefield acceleration, *Nature Phys.*, **5**, 363, (2009).

[17] E. Esarey, P. Sprangle, J. Krall., Laser acceleration of electrons in vacuum, *Phys. Rev. E*, **52**, 5443, (1995).

[18] A. Pukhov, Z.-M. Sheng, J. Meyer-ter-Vehn, Particle acceleration in relativistic laser channels, *Phys. Plasmas*, **6**, 2847, (1999).

[19] C. Gahn *et al*., Multi-MeV electron beam generation by direct laser acceleration in high-density plasma channels, *Phys. Rev. Lett.* **83**, 23, (1999).

[20] V. N. Khudik, A. V. Arefiev, X. Zhang, G. Shvets., Universal scalings for laser acceleration of electrons in ion channels, *Phys. Plasmas*, **23**, 103108, (2016).

[21] P. Gibbon, Short Pulse Laser Interactions with Matter: An Introduction (Imperial College Press, 2005).

[22] D. Strickland, G. Mourou., Compression of amplified chirped optical pulses, *Opt. Commun*., **56**, 212, (1985).

[23] W. B. Mori, C. Joshi, J. M. Dawson, D. W. Forslund, J. M. Kindel., Evolution of self-focusing of intense electromagnetic waves in plasma., *Phys. Rev. Lett.*, **60**, 1298 (1988).

[24] A. Pukhov, J. Meyer-Ter-Vehn., Relativistic magnetic self-channeling of light in near-critical plasma: Three-dimensional particle-in-cell simulation., *Phys. Rev. Lett.*, **76**, 3975 (1996).

[25] W. Lu, M. Tzoufras, C. Joshi, F. S. Tsung, W. B. Mori, J. Vieira, R. A. Fonseca, L. O. Silva., Generating multi-GeV electron bunches using single stage laser wakefield acceleration in a 3D nonlinear regime, *Phys. Rev. ST Accel. Beams*, **10**, 061301, (2007).

[26] I. Kostyukov, A. Pukhov, S. Kiselev, Phenomenological theory of laser-plasma interaction in "bubble" regime., *Phys. Plasmas*, **11**, 11 (2004).

[27] X. Zhang, V. N. Khudik, G. Shvets, Synergistic laser-wakefield and direct-laser acceleration in the plasma-bubble regime, *Phys. Rev. Lett.*, **114**, 184801 (2015).

[28] X. Zhang, V. N. Khudik, A. Pukhov, G. Shvets, Laser wakefield and direct acceleration with ionization injection, *Plasma Phys. Control. Fusion*, **58**, 034011 (2016).

[29] D. J. Stark, T. Toncian, A. V. Arefiev, Enhanced multi-MeV photon emission by a laser-driven electron beam in a self-generated magnetic field, *Phys. Rev. Lett.*, **116**, 185003 (2016).

[30] A. V. Arefiev, V. N. Khudik, A. P. L. Robinson, G. Shvets, L. Willingale, M. Schollmeier, Beyond the ponderomotive limit: Direct laser acceleration of relativistic electrons in sub-critical plasmas, *Phys. Plasmas*, **23**, 056704 (2016).

[31] N. M. Kroll, P. L. Morton, M. N. RosenBluth, Free-electron lasers with variable parameter wigglers, *IEEE J. Quantum Elec.* **QE-17**, 1436 (1981).

[32] D. H. Whittum, A. M. Sessler, J. M. Dawson, Ion-channel laser, *Phys. Rev. Lett.*, **64**, 2511 (1990)

[33] V. N. Khudik, X. Zhang, G. Shvets, Far-field constant-gradient laser accelerator of electrons in an ion channel, arXiv preprint arXiv:1610.09545 (2016).

[34] J. Birn *et al.,* Geospace Environmental Modeling (GEM) magnetic reconnection challenge, *J. Geophys. Res.* **106**, 3715 (2001).

[35] J. M. Dawson, Particle simulation of plasmas, *Rev. Mod. Phys.*, **55**, 403, (1983).

[36] C. K. Birdsall, A. B. Langdon, Plasma Physics via Computer Simulation (Taylor & Francis Group, 2004)

[37] K. S. Yee, Numerical solution of initial boundary value problems involving Maxwell's equations in isotropic media, *IEEE Trans. on Antennas and Propagation* **AP-14**, 302 (1966).

[38] A. Pukhov, Three-dimensional electromagnetic relativistic particle-in-cell code VLPL (Virtual Laser Plasma Lab), *J. Plasma Phys.* **61**, 425 (1999).

[39] L. Liu, Z. Shi, S. He, Analysis of the polarization-dependent diffraction from a metallic grating by use of a three-dimensional combined vectorial method, *J. Opt. Soc. Am. A* **21**, 1545 (2004).

[40] J. Villasenor, O. Buneman, Rigorous charge conservation for local electromagnetic field solvers, *Comput. Phys. Comm.* **69**, 306 (1992).

[41] C. Joshi, T. Tajima, J. M. Dawson, H. A. Baldis, N. A. Ebrahim, Forward Raman instability and electron acceleration, *Phys. Rev. Lett.* **47**, 1285 (1981).

[42] E. W. Gaul *et al.,* Demonstration of a 1.1 petawatt laser based on a hybrid optical parametric chirped pulse amplification/mixed Nd: glass amplifier, *Appl. Opt.* **49**, 1676 (2010).

[43] S. Kalmykov, S. A. Yi, V. Khudik, G. Shvets, Electron self-injection and trapping into an evolving plasma bubble, *Phys. Rev. Lett.* **103**, 135004 (2009).

[44] S. A. Yi, V. Khudik, S. Y. Kalmykov, G. Shvets, Hamiltonian analysis of electron self-injection and acceleration into an evolving plasma bubble, *Plasma Phys. Control. Fusion* **53**, 014012 (2011).

[45] S. A. Yi, V. Khudik, C. Siemon, G. Shvets, Analytic model of electromagnetic fields around a plasma bubble in the blow-out regime, *Phys. Plasmas* **20**, 013108 (2013).

[46] S. Steinke *et al.,* Multistage coupling of independent laser-plasma accelerators, *Nature (London)* **431**, 538 (2016).

[47] N. H. Matlis *et al*., Snapshots of laser wakefields, *Nature Phys*., **2**, 749 (2006).

[48] Z. Li *et al*., Single-shot visualization of evolving laser wakefields using an all-optical streak camera, *Phys*. *Rev*. *Lett*. **113**, 085001 (2014).

[49] A. Sävert *et al*., Direct observation of the injection dynamics of a laser wakefield accelerator using few-femtosecond shadowgraphy, *Phys*. *Rev*. *Lett*. **115**, 055002 (2015).

[50] J. D. Jackson, Classical Electrodynamics, (John Wiley&Sons, Inc, 2004).

[51] A. Rousse *et al*., Production of a keV X-ray beam from synchrotron radiation in relativistic laser-plasma interaction, *Phys*. *Rev*. *Lett*. **93**, 135005 (2004).

[52] S. Wang *et al*., X-ray emission from betatron motion in a plasma wiggler, *Phys*. *Rev*. *Lett*. **88**, 135004 (2002).

[53] K. Ta Phuoc *et al*., All-optical Compton gamma-ray source, *Nature Photon*., 6, 308 (2012).

[54] H. Tsai *et al*., Compact tunable Compton x-ray source from laser-plasma accelerator and plasma mirror, *Phys*. *Plasmas*, **22**, 023106, (2015).

[55] N. D. Powers *et al*., Quasi-monoenergetic and tunable X-rays from a laser-driven Compton light source, *Nature Photon*., **8**, 28 (2014).

[56] S. Chen *et al*., MeV-energy X rays from inverse Compton scattering with laser-wakefield accelerated electrons, *Phys*. *Rev*. *Lett*. **110**, 155003 (2013).

[57] H. Suk, N. Barov, J. B. Rosenzweig, Plasma electron trapping and acceleration in a plasma wake field using a density transition, *Phys*. *Rev*. *Lett*. **86**, 1011 (2001).

[58] C. G. R. Geddes *et al*., Plasma-density-gradient injection of low absolute-momentum-spread electron bunches, *Phys*. *Rev*. *Lett*. **100**, 215004 (2008).

[59] A. J. Gonsalves *et al*., Tunable laser plasma accelerator based on longitudinal density tailoring, *Nature Phys*., **7**, 862 (2011).

[60] K. Schmid *et al*., Density-transition based electron injector for laser driven wakefield accelerators, *Phys*. *Rev*. *ST Accel*. *Beams*, **13**, 091301 (2010).

[61] A. Buck *et al*., Shock-front injector for high-quality laser-plasma acceleration, *Phys*. *Rev*. *Lett*. **110**, 185006 (2013).

[62] D. Umstadter, J. K. Kim, E. Dodd, Laser injection of ultrashort electron pulses into wakefield plasma waves, *Phys*. *Rev*. *Lett*. **76**, 2073 (1996).

[63] E. Esarey, R. F. Hubbard, W. P. Leemans, A. Ting, P. Sprangle, Electron injection into plasma wakefields by colliding laser pulses, *Phys*. *Rev*. *Lett*. **79**, 2682 (1997).

[64] G. Fubiani, E. Esarey, C. B. Schroder, W. P. Leemans, Beat wave injection of electrons into plasma waves using two interfering laser pulses, *Phys. Rev. E.* **70**, 016402 (2004).

[65] M. Chen, Z-M. Sheng, Y. Y. Ma, J. Zhang, Electron injection and trapping in a laser wakefield by field ionization to high-charge states of gases, *J. Appl. Phys.* **99**, 056109 (2006).

[66] S. Augst, D. D. Meyerhofer, D. Strickland, S. L. Chin, Laser ionization of noble gases by Coulomb-barrier suppression, *JOSA B* **8**, 858 (1991).

[67] M. V. Ammosov, N. B. Delone, V. P. Krainov, Tunnelling ionization of complex atoms and of atomic ions in an alternating electromagnetic field, *Sov. Phys. JETP* **64**, 1191 (1986).

[68] L. V. Keldysh, Ionization in the field of a strong electromagnetic wave, *Sov. Phys. JETP* **20**, 1307 (1965).

[69] A. Pak, K. A. Marsh, S. F. Martins, W. Lu, W. B. Mori, C. Joshi, Injection and trapping of tunnel-ionized electrons into laser-produced wakes, *Phys. Rev. Lett.* **104**, 025003 (2010).

[70] B. B. Pollock *et al.*, Demonstration of a narrow energy spread ~ 0.5 GeV electron beam from a two-stage laser wakefield accelerator, *Phys. Rev. Lett.* **107**, 045001 (2011).

[71] R. Lehe, A. F. Lifschitz, X. Davoine, C. Thaury, V. Malka, Optical transverse injection in laser-plasma acceleration, *Phys. Rev. Lett.* **111**, 085005 (2013).

[72] C.-H. Pai, S.-Y. Huang, C.-C. Kuo, M.-W. Lin, J. Wang, S.-Y. Chen, C.-H. Lee, J.-Y. Lin, Fabrication of spatial transient-density structures as high-field plasma photonic devices, *Phys. Plasmas* **12**, 070707 (2005).

[73] M.-W. Lin, Y.-M. Chen, C.-H. Pai, C.-C. Kuo, K.-H. Lee, J. Wang, S.-Y. Chen, J.-Y. Lin, Programmable fabrication of spatial structures in a gas jet by laser machining with a spatial light modulator, *Phys. Plasmas* **13**, 110701 (2006).

[74] X. L. Xu *et al.*, Low emittance electron beam generation from a laser wakefield accelerator using two laser pulses with different wavelengths, *Phys. Rev. ST Accel. Beams* **17**, 061301 (2014).

[75] C. B. Schroeder *et al.*, Thermal emittance from ionization-induced trapping in plasma accelerators, *Phys. Rev. ST Accel. Beams* **17**, 101301 (2014).

[76] M. Chen *et al.*, Numerical modeling of laser tunneling ionization in explicit particle-in-cell codes, *J. Comput. Phys.* **236**, 220 (2012).

[77] J. S. Liu *et al.*, All-optical cascaded laser wakefield accelerator using ionization-induced injection, *Phys. Rev. Lett.* **107**, 035001 (2011).

[78] E. Oz *et al*., Ionization-induced electron trapping in ultrarelativistic plasma wakes, *Phys. Rev. Lett.* **98**, 084801 (2007).

[79] C. McGuffey *et al*., Ionization induced trapping in a laser wakefield accelerator, *Phys. Rev. Lett.* **104**, 025004 (2010).

[80] A. Karmakar, A. Pukhov, Collimated attosecond GeV electron bunches from ionization of high-Z material by radially polarized ultra-relativistic laser pulses, Laser Part. Beams **25**, 371 (2007).

[81] A. M. Sessler, D. H. Whittum, L-H. Yu, Radio-frequency beam conditioner for fast-wave free-electron generators of coherent radiation, *Phys. Rev. Lett.* **68**, 309 (1992).

[82] P. Sprangle, B. Hafizi, G. Joyce, P. Serafim, Methods for conditioning electron beams in free-electron lasers, *Phys. Rev. Lett.* **70**, 2896 (1993).

[83] C. B. Schroeder, E. Esarey, W. P. Leemans, Electron-beam conditioning by thomson scattering, *Phys. Rev. Lett.* **93** 194801 (2004).

[84] A. A. Zholents, Laser assisted electron beam conditioning for free electron lasers, *Phys. Rev. ST Accel. Beams* **8**, 050701 (2005).

[85] G. Penn, A. M. Sessler, J. S. Wurtele, A plasma channel beam conditioner for a free electron laser, *Proceedings of PAC07* **A06**, 1176 (2007).

[86] S. J. McNaught, J. P. Knauer, D. D. Meyerhofer, Measurement of the initial condition of electrons ionized by a linearly polarized, high-intensity laser, *Phys. Rev. Lett.* **78**, 626 (1997).

[87] G. Malka *et al*., Relativistic electron generation in interactions of a 30 TW laser pulse with a thin foil target, *Phys. Rev. E* **66**, 066402 (2002).

[88] K. Nakamura *et al*., GeV electron beams from a centimeter-scale channel guided laser wakefield accelerator, *Phys. Plasmas* **14**, 056708 (2007).

[89] L.-L. Yu *et al*., Two-color laser-ionization injection, *Phys. Rev. Lett.* **112**, 125001 (2014).

[90] K. Schmid, L. Veisz, Supersonic gas jets for laser-plasma experiments, *Rev. Sci. Instrum.* **83**, 053304 (2012).

[91] S. W. Jolly, Z. He, C. McGuffey, W. Schumaker, K. Krushelnick, A. G. R. Thomas, Stereolithography based method of creating custom gas density profile targets for high intensity laser-plasma experiments, *Rev. Sci. Instrum.* **83**, 073503 (2012).

[92] M. Vargas *et al*., Improvements to laser wakefield accelerated electron beam stability, divergence, and energy spread using three-dimensional printed two-stage gas cell targets, *Appl. Phys. Lett.* **104**, 231108 (2014).

[93] S. Gordienko, A. Pukhov, Scalings for ultrarelativistic laser plasmas and quasimonoenergetic electrons, *Phys. Plasmas* **12**, 043109 (2005).

[94] F. S. Tsung, R. Narang, W. B. Mori, C. Joshi, R. A. Fonseca, L. O. Silva, Near-GeV-energy laser-wakefield acceleration of self-injected electrons in a centimeter-scale plasma channel, *Phys. Rev. Lett.* **93**, 185002 (2004).

[95] M. Tzoufras *et al.,* Beam loading in the nonlinear regime of plasma-based acceleration, *Phys. Rev. Lett.* **101**, 145002 (2008).

[96] M. Chen, E. Esarey, C. B. Schroeder, C. G. R. Geddes, W. P. Leemans, Theory of ionization-induced trapping in laser-plasma accelerators, *Phys. Plasmas* **19**, 033101 (2012).

[97] T. Tajima, Y. Kishimoto, M. C. Downer, Optical properties of cluster plasma, *Phys. Plasmas* **6**, 3759 (1999).

[98] P. Serafim, P. Sprangle, B. Hafizi, Optical guiding of a radially polarized laser beam for inverse Cherenkov acceleration in a plasma channel, *IEEE Trans. Plasma Sci.* **28**, 1155 (2000).

[99] A. G. York , H. M. Milchberg , J. P. Palastro, T. M. Antonsen, Direct acceleration of electrons in a corrugated plasma waveguide, *Phys. Rev. Lett.* **100**, 195001 (2008).

[100] K. Nemeth, B. Shen, Y. Li, H. Shang, R. Crowell, K. C. Harkay, J. R. Cary, Laser-driven coherent betatron oscillation in a laser-wakefield cavity, *Phys. Rev. Lett.* **100**, 095002 (2007).

[101] S. Corde *et al.,* Controlled betatron x-ray radiation from tunable optically injected electrons, *Phys. Rev. Lett.* **107**, 255003 (2011).

[102] H. Guo *et al.,* Measurements of gain for slow cyclotron waves on an annular electron beam, *Phys. Rev. Lett.* **49**, 730 (1982).

[103] M. Einat, E. Jerby, Normal and anomalous Doppler effects in a dielectric-loaded stripline cyclotron-resonance maser oscillator, *Phys. Rev. E* **56**, 5996 (1997).

[104] J. L. Shaw, N. Lemos, L. D. Amorim, N. Vafaei-Najafabadi, K. A. Marsh, F. S. Tsung, W. B. Mori, C. Joshi, Role of Direct Laser Acceleration of Electrons in a Laser Wakefield Accelerator with Ionization Injection, *Phys. Rev. Lett.* **118**, 064801 (2017).

Vita

Xi Zhang was born in Jinhua, Zhejiang Province, China. He is the only child of Youling Zhang and Lizhen Lin. He stayed in Jinhua until graduation from Jinhua No.1 middle school. He chose physics as his undergraduate major and plasma physics as his master thesis topic in Zhejiang University. During his time of Zhejiang University, he met his wife Wenmin Zhang. Xi Zhang started graduate school at The University of Texas at Austin in August 2011.

Contact: jhzhangxi@gmail.com

This dissertation was typed by the author.